

SIGNATURES OF GEOCHEMICAL CHANGES AT METHANE-
SEEPS AS RECORDED BY SEEP CARBONATES

Dissertation

zur Erlangung des Doktorgrades der Naturwissenschaften

Dr. rer. nat.

am Fachbereich Geowissenschaften
der Universität Bremen
vorgelegt von

Dipl.-Geol. Tobias Himmler

Bremen, März 2011

Gutachter:

Prof. Dr. Jörn Peckmann

Prof. Dr. Gerhard Bohrmann

Tag des öffentlichen Promotionskolloquiums:

16. Juni 2011

„Phantasie ist wichtiger als Wissen, denn Wissen ist begrenzt.“

Albert Einstein

Table of contents

Preface.....	1
Abstract.....	2
Zusammenfassung.....	3
Chapter 1 Introduction.....	5
1.1 Cold methane-seeps – distribution, occurrence, and processes.....	5
1.2 Authigenic seep carbonates.....	9
1.3 Motivation and objectives.....	12
Chapter 2 Manuscripts.....	17
2.1 Manuscript 1.....	19
<i>Rare earth elements in authigenic methane-seep carbonates as tracers for fluid composition during early diagenesis</i>	
2.2 Manuscript 2.....	47
<i>Corrosion patterns of seep-carbonates from the eastern Mediterranean Sea</i>	
2.3 Manuscript 3.....	61
<i>Rare earth element signatures of early diagenesis in cold-seep pore waters on Hydrate Ridge, off Oregon</i>	
Chapter 3 Conclusions and outlook.....	79
Acknowledgements.....	82
References.....	84

Preface

The present thesis contains three studies, two of which are dedicated to the investigation of seep carbonates, and one to methane-seep pore waters. The results are presented in the form of three manuscripts arranged according to the date of submission. A brief introduction on general aspects of seep carbonates is given at the beginning, and a summary of the main results together with future research perspectives closes the thesis. The investigated materials comprise Recent seep carbonates from the Makran accretionary prism (offshore Pakistan; northern Arabian Sea) and the Anaximander seamounts (offshore SW Turkey, eastern Mediterranean Sea), retrieved during two research expeditions with R/V Meteor (M74/3 in 2007, and M70/3 in 2006, respectively). The pore water samples derive from Hydrate Ridge sediments on the Cascadia convergent margin (offshore Oregon, USA; north-eastern Pacific) and have been acquired during R/V Atlantis cruise AT3-35B in 1999. All studies were carried out within the framework of the MARUM–Center for Marine and Environmental Sciences research area “*Geo-Biosphere Interactions*”. The submitted manuscripts are contributions to the project “*GB6 Mineral authigenesis and organomineralization*”.

Abstract

In the first manuscript (chapter 2.1) petrographic and geochemical data of aragonitic seep carbonates from the Makran accretionary prism are presented. High-resolution rare earth element (REE) analysis yield distinct total REE_{aragonite} concentrations and shale-normalised REE_{aragonite} patterns. The REE variations are ascribed to different pore fluid compositions and accompanied redox changes during aragonite precipitation. The second manuscript (chapter 2.2) deals with early diagenetic alterations of aragonitic seep-carbonate crusts exposed at the Amsterdam and Athina mud volcanoes (eastern Mediterranean Sea). Detailed thin section analysis reveals that widespread carbonate corrosion created significant amounts of secondary porosity. In order to explain carbonate dissolution a simple model is proposed, involving the aerobic oxidation of methane and hydrogen sulphide. The third manuscript (chapter 2.3) describes the distribution of REE in anoxic pore waters on Hydrate Ridge (Cascadia subduction zone, north-eastern Pacific). The pore waters are markedly enriched in REEs compared to bottom water and display variable shale-normalised patterns, remarkably with positive as well as negative Ce anomalies. Authigenic seep carbonates are suggested as efficient REE sinks at methane-seeps.

Zusammenfassung

Im ersten Manuskript (Kapitel 2.1) werden petrographische und geochemische Daten einer Methan-Karbonate Probe vom Makran-Akkretionskeil (nördliches Arabisches Meer) diskutiert. Hochauflösende Messungen von Seltenerdelementen (SEE) an zeitlich aufeinander folgenden Aragonit-Zementen zeigen deutlich variierend SEE-Gesamtkonzentrationen und SEE-Muster. Als Ursachen für diese Variationen werden chemisch unterschiedlich zusammengesetzte Porenfluide und ein sukzessiver Wechsel des Redox-Milieus von reduzierend nach oxidierend angenommen. Das zweite Manuskript (Kapitel 2.2) beschreibt früh-diagenetische Veränderungen hochporöser Methan-Karbonate an zwei Schlamm-Vulkanen (Amsterdam und Athina) im östlichen Mittelmeer. Petrographischen Detailstudien zeigen, dass durch Karbonat-Lösung ein enormer Anteil an Sekundär-Porosität in den Karbonaten entstanden ist. Mit einer aus der Literatur übernommenen Hypothese wird ein einfaches Modell erläutert, wie durch aerobe Oxidation von Methan und Schwefelwasserstoff Karbonat-Lösung induziert wird. Das dritte Manuskript (Kapitel 2.3) beschreibt die Verteilung von SEE in reduzierten Porenwässern auf dem Hydrat-Rücken (Cascadia-Subduktionszone, nordöstlicher Pazifik). Die Konzentrationen an SEE in den Porenwässern sind stark erhöht im Vergleich zum Bodenwasser und zeigen unterschiedliche SEE-Muster. Authigene Karbonate werden als potentielle Senke für SEE an Methan-Austrittstellen vorgeschlagen. Die SEE-Muster der reduzierten Porenwässer sind sowohl durch positive als auch negative Cer-Anomalien gekennzeichnet.

1 Introduction

1.1 Cold methane-seeps – distribution, occurrence, and processes

Submarine fluid expulsions are known as hot vents and cold seeps, depending on the emission rate, temperature, and chemical composition of the fluids (Herzig and Hannington, 2006). In general, the term cold seep refers to fluid expulsion systems at ambient seawater temperature and relatively slower emission rates, as opposed to hot vents (Parnell, 2002). In contrast to hot vents which are mainly located at oceanic spreading centres, cold seeps are ubiquitous on continental margins (Schlüter, 2002; Fig. 1).

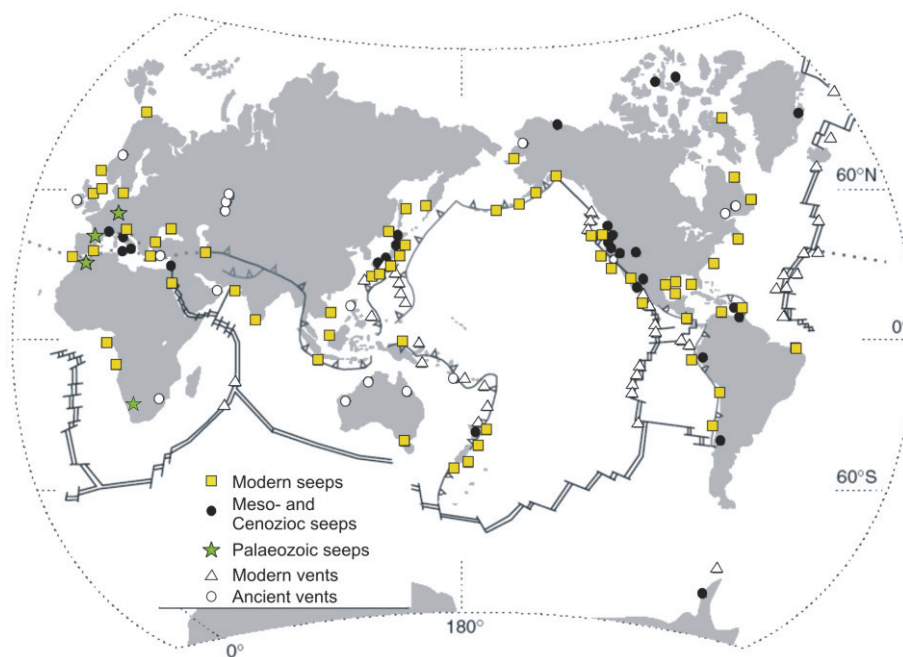


Figure 1: Global distribution of modern and ancient seep and vents deposits. Modified from Campbell (2006)

A wealth of geological features is associated with cold seeps and deposits thereof are frequently recognised in the ancient rock record (Fig. 1; Campbell, 2006). Different types of cold seeps occur on continental margins, including

groundwater seeps, brine seeps, and hydrocarbon seeps (Schlüter, 2002). The occurrence of hydrocarbon seeps on continental margins principally reflects the high input of organic matter. In ocean margin settings the accumulation of sedimentary organic matter is promoted (i) by enhanced primary production and fast sedimentation rates, and (ii) in restricted basins with anoxic water bodies (e.g., Rulkötter, 2006). Subsequent to deposition of organic rich sediments hydrocarbons are generated in the course of diagenesis and later burial by degradation of organic matter (Tissot and Welte, 1992). Sediment compaction, either tectonically induced at convergent margins or through increasing lithostatic pressure due to high sedimentation rates at passive margins, leads to overpressured pore fluids and sediment dewatering transports hydrocarbon-rich fluids to the seafloor (Fig. 2).

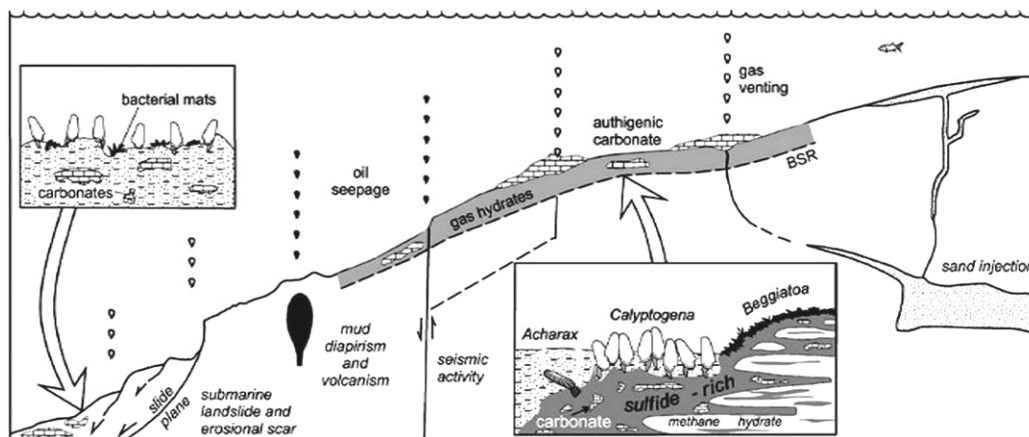


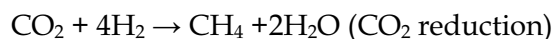
Figure 2: Schematic cross section through continental margin sediments illustrating hydrocarbon-seeps and associated features. Hydrocarbon-rich fluids migrate through the sediments along faults and sand injections due to sediment compaction and dewatering; ascending methane forms gas hydrates (BSR = bottom simulating reflector, indicating the lower boundary of the gas hydrate stability zone); oil-seeps are related to deep-sourced mud volcanoes and reservoirs; cold-seep carbonates precipitate within anoxic sediments and form chemohermers at the seafloor; chemosynthesis-based communities of clams (e.g., *Acharax*, *Calyptogena*) and bacterial mats (e.g., sulphide-oxidizing *Beggiatoa*) inhabit the sediments at methane-seeps. Figure adopted from Campbell (2006).

Methane-seeps are the most abundant cold hydrocarbon-seeps (e.g., Judd and Hovland, 2007), occurring on convergent as well as passive continental margins, and in shallow as well as deep water environments (e.g., Kulm et al.,

1986; Sweeney, 1988, Aharon et al., 1992; Suess et al., 1998; Bohrmann et al., 2002; Naudts et al., 2006; Klaucke et al., 2010).

At methane-seeps, fluids enriched in methane and hydrogen sulphide emanate from the sediment into the water column. The reduced compounds sustain unique cold seep ecosystems of chemosynthesis-based communities (Sibuet and Olu-Le Roy, 2002; Levin, 2005; Fig. 2). Benthic faunal assemblages at methane-seeps are dominated by sulphide-oxidizing bacteria (e.g., *Beggiatoa*, *Thioploca*), large chemosynthetic bivalves (vesicomid clams, mytilid mussels), and vestimentiferan tube worms. The chemosynthetic bivalves and tube worms harbour chemoautotrophic microbial endosymbionts in their tissues that rely on the oxidation of methane and hydrogen sulphide from the seepage fluids for obtaining energy and organic carbon production (Fischer, 1990). Therefore, the recognition of cold seep ecosystems on the seafloor provides reliable evidence for methane-seeps on continental margins (e.g., Sahling et al., 2002; Sibuet and Olu-Le Roy, 2002).

Methane is generated during early diagenesis and later burial of sedimentary organic matter (e.g., Claypool and Kvenvolden, 1983). Early diagenetic methane (= microbial methane) is produced in anoxic sediments below the sulphate-reduction zone by methanogenic archaea using acetate and carbon dioxide as carbon source to produce methane with molecular hydrogen (Fig. 3; Reeburgh, 2007).



Sedimentary organic matter that survives microbial degradation will be exposed to higher temperature during burial and undergo successive thermocatalytic breakdown to low molecular weight hydrocarbons, ultimately to thermogenic methane (Tissot and Welte, 1992). The two methane sources (microbial vs. thermogenic) can be discriminated based on the carbon and hydrogen isotopic signature and the molecular ratio of methane (C_1) over heavier

hydrocarbons ($C_2 + C_3$ compounds) (Claypool and Kvenvolden, 1983; Whiticar, 1999). Microbial methane (-110 to -50‰) is depleted in ^{13}C relative to thermogenic methane (-50 to -20‰) and yields significantly higher ($C_1/C_2 + C_3$) values.

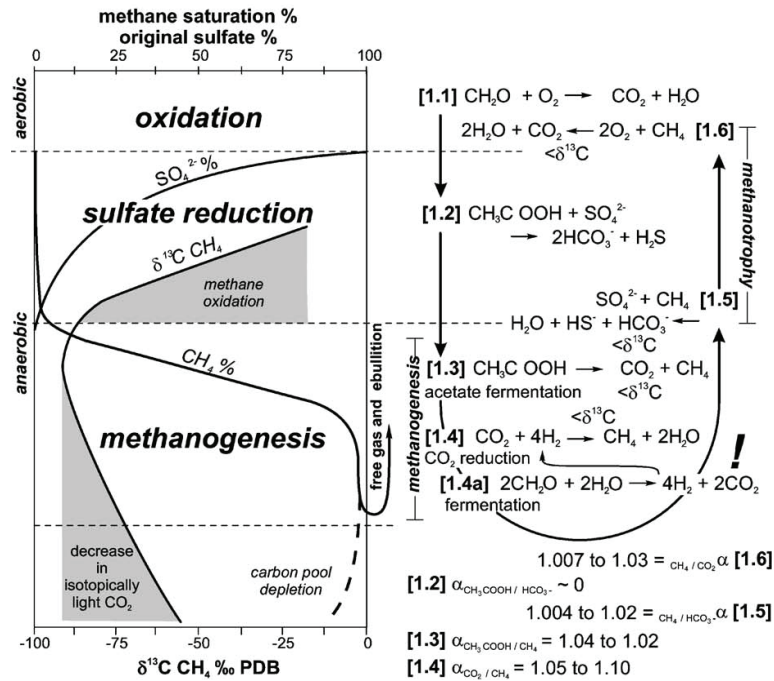


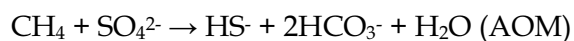
Figure 3: Left panel: Schematic profile through the oxic, sulphate reduction, and methanogenic zones of methane-seep sediments (increasing sediment depth from the top; arbitrary scale) and related methane carbon isotope signature (cf. Whiticar, 1999). Right panel: Major pathways and reactions of early diagenetic organic carbon mineralization and associated carbon isotope fractionations; equations [1.3] and [1.4] illustrate the generation of extremely ^{13}C -depleted microbial methane ($<\delta^{13}\text{C}$) through acetate fermentation or CO_2 -reduction, which is converted to ^{13}C -depleted bicarbonate (HCO_3^- ; $<\delta^{13}\text{C}$) and hydrogen sulphide (HS^-) at the base of the sulphate-reduction zone *via* the anaerobic oxidation of methane [1.5]. Figure adopted from Campbell (2006).

In sediments where sufficient methane is available to exceed methane-solubility in pore fluids and under appropriate pressure and temperature conditions such as encountered today below ~ 450 m water depth, gas hydrates form (Bohrmann and Torres, 2006). Gas hydrates are ice-like solid compounds formed of gas molecules encaged by ice crystals. Methane constitutes the main hydrocarbon compound in gas hydrates, although other guest molecules like carbon dioxide, hydrogen sulphide, ethane, propane, and butane can be

incorporated into gas hydrate as well (Bohrmann and Torres, 2006). The presence of gas hydrates in marine sediments can be deduced from various lines of evidences, including: (i) seismic evidence in the form of a bottom simulating reflector (BSR) which marks the lower boundary of the gas hydrate stability zone in sediments; (ii) chemical evidence from pore water analysis (i.e. chlorine and $\delta^{18}\text{O}$ anomalies in pore waters); (iii) direct evidence of solid gas hydrates retrieved from seafloor sediments with geological sampling tools. Gas hydrates are sensitive to changes of pressure and temperatures, affecting their stability field (cf. Bohrmann and Torres, 2006) and methane-seeps are often associated with gas hydrates decomposition (e.g., Suess et al., 1999). Overall, gas hydrates constitute a huge dynamic carbon reservoir in marine sediments and play an essential role in the global carbon cycle (e.g., Dickens, 2003).

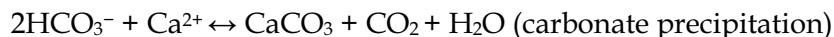
1.2 Authigenic seep carbonates

Large amounts of the methane generated in continental margin sediments is anaerobically oxidised within the sediments through microbially mediated sulphate-dependent anaerobic oxidation of methane (AOM; Fig. 3):



AOM is the key process at methane-seeps and constitutes a major sink for methane in marine sediment (Hinrichs and Boetius, 2002; Reeburgh, 2007). The process of AOM is mediated by a microbial consortium consisting of anaerobic methane-oxidizing archaea and sulphate-reducing bacteria (Boetius et al., 2000). This consortium synthesises highly ^{13}C -depleted organic molecules which can be used as diagnostic molecular biomarkers for sulphate-dependent AOM in methane-seep sediments (Hinrichs and Boetius, 2002, and references therein).

The production of bicarbonate through AOM leads to increased pore water alkalinity, resulting in the precipitation of seep carbonates (e.g., Ritger et al, 1987; Luff and Wallmann, 2003).



Aragonite, high-magnesium calcite, and dolomite are the main carbonate lithologies of seep carbonates (e.g., Roberts and Aharon, 1994; Bohrmann et al., 1998; Greinert et al., 2001; Luff and Wallmann, 2003). The close link between AOM and carbonate precipitation at methane-seeps is manifested in AOM-specific ^{13}C -depleted lipid biomarkers which are incorporated into seep carbonates (e.g., Peckmann et al., 1999; Thiel et al., 2001; Aloisi et al., 2002; Michaelis et al., 2002; Birgel, et al., 2008; Leefmann et al., 2008; Haas et al., 2010). These findings demonstrate the crucial role of AOM for the precipitation of seep carbonates.

Seep carbonates are characterised by negative $\delta^{13}\text{C}$ values, generally below -30‰ V-PDB (cf. Peckmann and Thiel, 2004) because the highly ^{13}C -depleted methane carbon is converted during AOM to ^{13}C -depleted bicarbonate which is used for carbonate precipitation (Fig. 3). However, the $\delta^{13}\text{C}$ values of seep carbonates are isotopically heavier than their parent methane due to admixture of relatively ^{13}C -enriched carbon species during carbonate precipitation (cf. Peckmann and Thiel, 2004). Thus, the $\delta^{13}\text{C}$ values of seep carbonates can be used to decipher the main carbon source because seep carbonates inherit the $\delta^{13}\text{C}$ signature of the dominant carbon species during precipitation (Fig. 4; e.g., Formolo et al., 2004).

Oxygen stable isotope signatures of seep carbonates can be used in combination with mineralogical data to decipher pore fluid compositions during precipitation (e.g., Bohrmann et al., 1998; Han et al., 2004). For instance, high-magnesium calcite associated with gas hydrates shows anomalously positive $\delta^{18}\text{O}$ values because dissociation of gas hydrate liberates ^{18}O -enriched pore water from which the carbonates precipitate (Fig. 4; e.g., Bohrmann et al., 1998; Pierre and Fouquet, 2007).

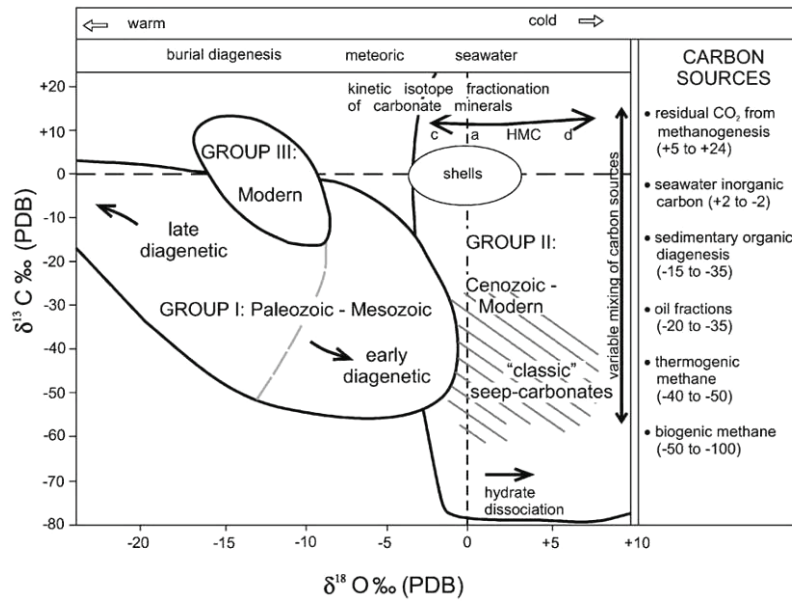


Figure 4: Stable carbon and oxygen isotope signatures of Phanerozoic seep carbonates and specific $\delta^{13}\text{C}$ signatures of different carbon sources; c = calcite; a = aragonite; HMC = high-Mg calcite; d = dolomite. $\delta^{13}\text{C}$ and $\delta^{18}\text{O}$ values of modern seep carbonates are shown in group II; note the variations in $\delta^{13}\text{C}$ due to variable mixing of different carbon sources; anomalously positive $\delta^{18}\text{O}$ values indicate that the seep carbonates precipitated from ^{18}O -enriched fluids originating from gas hydrate dissociation. Figure adopted from Campbell (2006).

Moreover, seep carbonates comprise geological archives to study changing environmental parameters and duration of past seepage. Uranium-thorium dating of seep carbonates from various methane-seeps revealed sub-recent intervals of intensive seepage accompanied by enhanced precipitation of seep carbonates, probably related to Quaternary sea-level fluctuations and gas hydrate destabilisation due to increasing bottom water temperatures (Feng et al., 2010b, and references therein).

1.3 Motivation and objectives

The driving hypothesis for this study is that variable fluid flux rates modify the redox conditions at methane-seeps and authigenic seep carbonates may provide geological archives to study those changes.

Precipitation of seep carbonates is microbially induced by AOM under anoxic conditions. However, the redox conditions can change significantly because methane-seeps are highly dynamic systems with variable fluid flux rates and directions of fluid flow (e.g., Tryon et al., 1999; Tryon and Brown, 2001; Torres et al., 2002; Solomon et al., 2008). On the one hand, high flux rates of methane charged fluids can push the lower boundary of the sulphate reduction zone where AOM occurs close to the sediment water interface (e.g., at 2 cm below the seafloor; cf. Boetius et al., 2000), and thus trigger seep-carbonate formation under anoxic conditions near the seafloor. During periods of low flux, on the other hand, oxygenated bottom water infiltrating the sediment causes a shift of the zone of AOM, respectively the zone of seep-carbonate formation, further downward into the anoxic sediment. In this case, however, under sufficient methane supply AOM maintains bicarbonate production and the produced bicarbonate may be transported with diffusing pore fluids into the shallow sediment and eventually precipitate under oxic conditions (cf. Feng et al., 2009a). Variation in flux rates and associated redox changes can occur at various time scales. For example, the flux rates at methane-seep in gas hydrate rich sediments on Hydrate Ridge varies in response to the variations of the hydrostatic pressure on gas hydrates due to tidal cycles (higher flux rates = low hydrostatic pressure = low tide, and *vice versa*; cf. Torres et al., 2002).

Indeed, there is growing evidence that seep carbonates record variable redox conditions at methane-seeps. Biomarkers of aerobic methanotrophs are present in modern methane-seep sediments (Elvert and Niemann, 2008) and are frequently found in ancient seep carbonates (Birgel and Peckmann, 2008), indicating that oxic conditions are common at methane-seeps. Remarkably, when oxic conditions prevail over relatively long periods at methane-seeps, aerobic oxidation of methane may become the dominant process and support dissolution

of seep carbonates. The carbon dioxide produced during aerobic oxidation of methane results in increasing $p\text{CO}_2$ and consequently dissolution of seep carbonates (e.g., Matsumoto, 1990; Paull et al., 1992). Nevertheless, biomarker evidence for oxic conditions was recently supported by rare earth element (REE) studies of modern and ancient seep carbonates, which indicate that variable redox conditions occurred during seep-carbonate precipitation (e.g. Feng et al., 2008; 2009a, 2009b). Remarkably, Birgel et al. (2011) found a striking co-occurrence of biomarkers for aerobic methanotrophs and REE signatures indicative of oxic conditions in Recent seep carbonates from the Gulf of Mexico. REE geochemistry is widely used for palaeoredox reconstructions because of the redox-sensitive behaviour of the element Cerium (Ce). The application of Ce as redox-tracer is based on the fact that the naturally trivalent Ce^{3+} is oxidised to Ce^{4+} under oxic conditions, and thus departs in its geochemical behaviour from the other trivalent REE (cf. Brookins, 1989). This results in a “negative Ce anomaly” in shale-normalised REE patterns. For example, in oxygenated seawater dissolved Ce^{3+} is microbially oxidised to insoluble Ce^{4+} (Moffett, 1990). Consequently, oxic seawater is characterised by a distinctive negative Ce anomaly (e.g., de Baar et al., 1985; Sholkovitz et al., 1994). Anoxic seawater, on the other hand, lacks distinct negative Ce anomalies or even possesses slightly positive Ce anomalies (Fig. 5; de Baar et al., 1988). The Ce anomaly has been defined as the measured shale-normalised Ce value (Ce_{SN}) divided by the “expected” Ce value (Ce^*), estimated by linear extrapolation over its direct REE neighbours Lanthanum (La) and Praseodymium (Pr):

$$\text{Ce}/\text{Ce}^* = 2\text{Ce}_{\text{SN}}/[\text{La}_{\text{SN}} + \text{Pr}_{\text{SN}}]$$

However, due to anomalous behaviour of La itself, this modification should be avoided and Ce anomalies should be calculated with the more appropriate near REE neighbours Pr and Neodymium (Nd) as follows (e.g., Bolhar et al., 2004):

$$\text{Ce}/\text{Ce}^* = \text{Ce}_{\text{SN}}/[2\text{Pr}_{\text{SN}}-\text{Nd}_{\text{SN}}]$$

However, both modifications are widely used in literature.

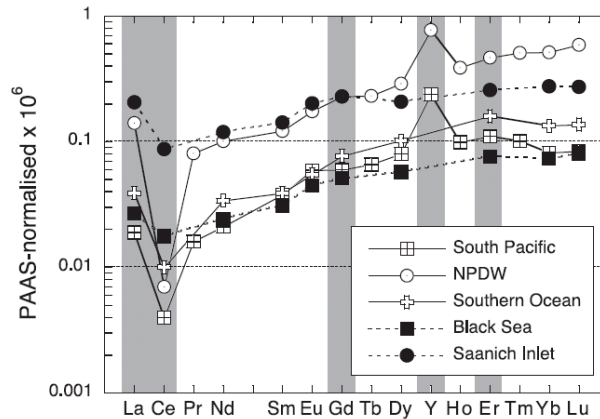


Figure 5: Shale-normalised (PAAS = Post-Archaean Australian Average Shale) REE+Y patterns of modern seawater. Note the distinct negative Ce anomalies (downward “V”) for oxic seawater (white symbols) whereas anoxic seawater (black symbols) shows no Ce anomalies. Figure adopted from Bolhar et al. (2004).

REEs are incorporated as in marine carbonates as substitutes for Ca^{2+} without significant fractionation over the REE series (e.g., Terakado and Masuda, 1988; Webb and Kamber, 2000; Webb et al., 2009). The incorporation of Na^+ at Ca^{2+} sites is thought to balance the excess charge created by REE^{3+} coprecipitation with calcite and aragonite (Zhong and Mucci, 1995; Qu et al., 2009).



The characteristic seawater REE+Y pattern (Fig. 5) is preserved over geological times in marine microbial carbonates, which are valuable proxies for ancient seawater redox-geochemistry (e.g., Bolhar et al., 2004; Kamber and Webb, 2001). Microbial carbonates of Archaean age yield remarkably similar shale-normalised REE patterns to that of modern seawater, however, without distinct negative Ce anomalies (Fig. 6). The lack of distinct Ce anomalies in microbialites from the Campbellrand Formation (South Africa) is ascribed to intermixing anoxic deep waters on a shallow carbonate platform where the microbialites

formed (Kamber and Webb, 2001). Likewise, seep carbonates may preserve REE characteristics of redox changes resulting from different fluid flux rates (e.g., Feng et al., 2009a, Birgel et al., 2011): Seep carbonates characterised by negative Ce anomalies indicate oxic conditions during carbonate precipitations, whereas the absence of negative Ce anomalies point to anoxic conditions.

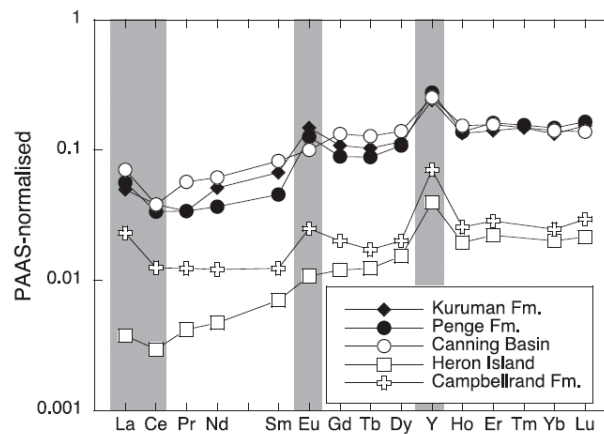


Figure 6: Shale-normalised REE+Y patterns from Archaean (BIF samples from Kuruman and Penge Formations; microbial carbonate samples from the Campbellrand Formation), Devonian microbialites (reef carbonates from Canning Basin), and modern microbialites (Heron Island samples); note the absence of negative Ce anomaly in the Archaean samples. Figure adopted from Bolhar et al. (2004).

With respect to geochemical implications on seep-carbonate derived REE patterns, the distribution of REE in methane-seep pore waters may provide additional information. In general, all REEs are indirectly redox sensitive during early diagenesis as demonstrated from REE distribution in oxic and anoxic pore waters (Haley et al., 2004): Anoxic pore waters are characterised by distinct convex-up shaped REE patterns because REE are mainly sourced from reductive dissolution of iron oxides in the iron reduction zone. Oxic pore waters, on the other hand, show seawater-like patterns. Thus, seep carbonates that formed under anoxic conditions may display convex-up shaped REE patterns from anoxic pore waters (cf. Feng et al., 2009b).

It was the goal of this study to characterise geochemical variations at methane-seeps by integration of detailed petrographic observations, high-resolution trace and major element data of modern seep carbonates, and major and trace element signatures of methane-seep associated pore waters.

The specific objectives were to:

- 1) Measure rare earth elements (REE) in pore waters and seep carbonates and integrate the REE data with other geochemical data (stable carbon and oxygen isotopes, mineralogy, major pore water parameters).
- 2) Describe early diagenetic alterations of seep carbonates by detailed macro- and petrographic observations.

2 Manuscripts

2.1 Manuscript 1

Rare earth elements in authigenic methane-seep carbonates as tracers for fluid composition during early diagenesis

T. Himmler, W. Bach, G. Bohrmann, J. Peckmann

*MARUM–Center for Marine Environmental Sciences and Faculty of Geosciences,
University of Bremen, PO Box 330 440, 28334 Bremen, Germany*

Published 2010

in *Chemical Geology* 227, 126–136. doi: 0.1016/j.chemgeo.2010.07.015

(Reproduced with permission of Elsevier)

Abstract

Authigenic carbonates forming at an active methane-seep on the Makran accretionary prism mainly consist of aragonite in form of microcrystalline, cryptocrystalline, and botryoidal phases. The $\delta^{13}\text{C}_{\text{carbonate}}$ values are very negative (-49.0 to -44.0% V-PDB), agreeing with microbial methane as dominant carbon source. The $\delta^{18}\text{O}_{\text{carbonate}}$ values are exclusively positive ($+3.0$ to $+4.5\%$ V-PDB) and indicate precipitation in equilibrium with seawater at bottom water temperatures. The content of rare earth elements and yttrium (REE+Y) determined by laser ablation-inductively coupled plasma-mass spectrometry (LA-ICP-MS) and solution ICP-MS varies for each aragonite variety, with early microcrystalline aragonite yielding the highest, cryptocrystalline aragonite intermediate, and later botryoidal aragonite the lowest REE+Y concentrations. Shale-normalised REE+Y patterns of different types of authigenic carbonate reflect distinct pore fluid compositions during precipitation: Microcrystalline aragonite shows high contents of middle rare earth elements (MREE), reflecting REE patterns ascribed to anoxic pore water. Cryptocrystalline aragonite exhibits a seawater-like REE+Y pattern at elevated total REE+Y concentrations, indicating higher concentrations of REEs in pore waters, which were influenced by seawater. Botryoidal aragonite is characterised by seawater-like REE+Y patterns at initial growth stages followed by an increase of light rare earth elements (LREE) with advancing crystal growth, reflecting changing pore fluid composition during precipitation of this cement. Conventional sample preparation involving micro-drilling of carbonate phases and subsequent solution ICP-MS does not allow to recognise such subtle changes in the REE+Y composition of individual carbonate phases. To be able to reconstruct the evolution of pore water composition during early diagenesis, an analytical approach is required that allows to track the changing elemental composition in a paragenetic sequence as well as in individual phases. High-resolution analysis of seep carbonates from the Makran accretionary prism by LA-ICP-MS reveals that pore fluid composition not only evolved in the course of the formation of different phases, but also changed during the precipitation of individual phases.

1. Introduction

Fluid expulsions on the seafloor where methane rich fluids emanate from the sediment into the water column are known as methane-seeps. They are ubiquitous along modern continental margins and their deposits are frequently recognised in the ancient rock record (Campbell, 2006; Naehr et al., 2007). Modern methane-seeps are characterised by highly variable seepage intensity (e.g., Tryon et al., 1999; Klaucke et al., 2010). As a consequence of this variability, early diagenetic conditions within methane-seep sediments may change significantly (cf. Tryon and Brown, 2001). Carbonates form within anoxic sediments at methane-seeps as a result of increased pore water alkalinity caused by sulphate-dependent anaerobic oxidation of methane (AOM) mediated by prokaryotes (e.g., Ritger et al., 1987; Paull et al., 1992; Boetius et al., 2000). These authigenic carbonates represent excellent geochemical archives for studying the evolution of pore fluids and biogeochemical processes at seeps. For instance, stable carbon and oxygen isotopes of seep carbonates have been frequently used to decipher the carbon source and the chemical composition of pore fluids (e.g., Bohrmann et al., 1998; Aloisi et al., 2000; Formolo et al., 2004; Peckmann and Thiel, 2004; Teichert et al., 2005).

Haley et al. (2004) presented a model for the evolution of rare earth element (REE) patterns in pore waters during early diagenesis in marine sediments. These authors demonstrated that REEs can be used to elucidate geochemical processes in early diagenetic settings. The REE plus yttrium (Y) patterns of pore fluids are recorded in diagenetic carbonates; modern marine shallow-water carbonates for instance are robust proxies for seawater chemistry (e.g., Webb et al., 2009 and references therein). Likewise, REE+Y geochemistry of seep carbonates may reflect early diagenetic processes. Recently, the REE geochemistry of methane-seep carbonates has been studied in order to assess redox-conditions during carbonate precipitation (Feng et al., 2008; 2009a;b; 2010). Based on differences in Ce anomalies between varieties of carbonate cement of ancient and modern seep limestones, Feng et al. (2009a;b) suggested that redox-conditions varied widely during carbonate precipitation. Carbonate samples in these studies were micro-

drilled from limestones, dissolved and analysed by ICP-MS, so it was not possible to resolve heterogeneities within individual carbonate phases.

Here we present a high spatial resolution microanalytical REE+Y analysis of seep carbonates from the Makran accretionary prism, offshore Pakistan. The carbonates were analysed using a combination of high-resolution LA-ICP-MS and solution ICP-MS. This study aims to show that the combination of these methods reveals veritable variations in REE+Y concentrations and distinct shale-normalised REE+Y patterns for each carbonate phase, thus implying highly variable environmental conditions during carbonate precipitation. In this study, we use the term 'phase' to refer to varieties of authigenic aragonite representing different stages of the paragenetic sequence.

2. Regional Setting

The large Makran accretionary complex developed between the Arabian and European plates in the northern Arabian Sea, covering the Makran region in southern Iran and Pakistan (Fig. 1). It constitutes a long-lived convergent plate boundary where oceanic crust is actively subducted beneath continental crust (Farhoudi and Karig, 1977), representing an example of the structural evolution at active continental margins and related sediment dewatering processes (e.g., White, 1984; Platt et al., 1985; Minshull and White, 1989; Fruehn et al., 1997; von Rad et al., 2000; Grando and McClay, 2007). Following the accretion of the Makran micro-plate to Eurasia in the Late Cretaceous, northward subduction of the Arabian Plate has continued at fairly constant rates during the Cenozoic (Golonka, 2004). Erosion of the contemporaneously forming Himalayan orogenic belt provided continuous sediment supply that was deposited in the present-day northern Arabian Sea (Garzanti et al., 1996). Since the middle Miocene, steady convergence and sediment input resulted in frontal accretion, thrust faulting, large-scale underthrusting and underplating of sediment beneath the Eurasian plate followed by progressive uplift of the coastal Makran (Platt et al., 1985). Only 150 km of the frontal accretionary complex are submerged today whereas 400 km of the accretionary complex are exposed onshore southern Iran and Pakistan

(White, 1984; Platt et al., 1985). A prominent bottom simulating reflector was traced across the Makran shelf indicating the occurrence of gas hydrates at 500 to 800 m sediment depth underlain by free gas (White, 1984; Minshull and White, 1989; Sain et al., 2000; von Rad et al., 2000). Numerous gas and fluid expulsions are reported from the Makran accretionary complex including offshore mud diapirs (Wiedicke et al., 2001), onshore mud volcanoes (e.g., Farhoudi and Karig, 1977; White, 1984), and methane-seeps (von Rad et al., 1996; 2000). Methane-seeps were often found in water depth of less than 800 m, which is believed to represent the upper limit of the gas hydrate stability field (Delisle, 2004). Authigenic carbonates at methane-seeps on the Makran shelf have been reported previously in a water depth of approximately 850 m (von Rad et al., 1996). During R/V METEOR cruise M74/3 active gas seeps have been found over the entire margin at water depths between 575 and 2870 m (Bohrmann et al., 2008). This study deals with seep carbonates from an active methane-seep named 'Flare 7' (Bohrmann et al., 2008; Fig. 1) in 1656 m water depth located mid-slope of the Makran accretionary prism (24°38.556'N, 62°44.246'E). The fauna observed at this site includes living tube worms, sponges (Fig. 1), and bathymodiolin mussels.

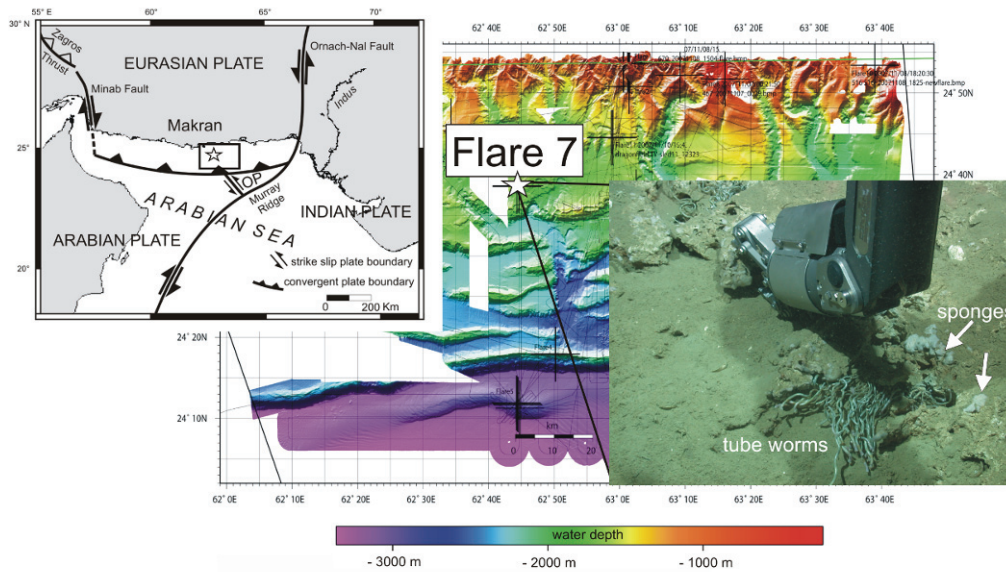


Fig. 1: Regional tectonics sketch map (upper left; OP = Ormara Plate; redrawn after Kukowski et al., 2001) and bathymetric map (centre) of the Makran accretionary complex created during M74/3; asterisks indicate sample locality at site 'Flare 7'. The photograph in the lower right shows the ROV-assisted sample recovery and seep-dwelling tube worms and sponges.

3. Analytical procedures

The sample (GeoB 12338-2) was retrieved during R/V METEOR cruise 74/3 in 2007 using the manipulator arm of the ROV MARUM-QUEST4000 (Fig. 1).

Thin sections (48 x 28 mm) were prepared for standard petrographic investigations and fluorescence microscopy on a Zeiss Axioskop 40A.

Rare earth element and yttrium (REE+Y) concentrations were determined by LA-ICP-MS and solution ICP-MS, both conducted on a ThermoFinnigan Element2 mass spectrometer at the University of Bremen. The use of LA-ICP-MS allowed phase-specific high-resolution probing of REE+Y concentrations in homogenous carbonate phases on thin sections. The laser (NewWave UP193) was operated with a 5 Hz pulse rate at approximately 1.3 GW/cm² irradiance and a beam diameter of 100 μm. A pre-ablation step with 120 μm beam diameter (approximately 0.3 GW/cm², 5 Hz) was done for each spot to avoid surface contamination. Data were calibrated against NIST612 glass standard with concentrations reported by Pearce et al. (1997). We used ⁴³Ca as internal standard assuming a Ca content of 40.00% for the analysed carbonate samples. Both the

calibration standard (NIST612) and the reference rock BCR-2 were measured as unknowns repeatedly throughout data collection. Average concentrations and standard deviations of the means are provided in Table 1 along with the recommended reference values for comparison.

When the beam diameter was too large to avoid ablation of detrital particles, we measured the REE+Y concentrations of both carbonate and detrital background sediment by solution ICP-MS following selective dissolution. In that procedure two samples of carbonate-cemented sediment were drilled with a handheld micro-drill from a polished slab, approximately 150 mg rock powder each, and dissolved in 20 ml double-distilled 2% HNO₃ (10 μ l [HNO₃]:100 ml [Milli-Q[®]], pH = 3) for 30 minutes at room temperature. No bubbling was observed after 30 min. To separate the dissolved carbonate fraction from insoluble non-carbonates, the obtained solutions were centrifuged immediately after carbonate dissolution and supernatants were carefully decanted. Then, the dissolved carbonate fraction was evaporated for 96 hours at 40°C to approximately 4 ml. Insoluble residues (approximately 25 mg) were washed three times with Milli-Q[®], dried, and dissolved in a mixture of double-distilled concentrated HNO₃, HCl, and HF. Following microwave digestion and complete evaporation of the solutions the residues were dissolved in 20 ml of 2% HNO₃. For ICP-MS measurements, 1 ml of the solution of the carbonate fraction was added to 9 ml double-distilled 2% HNO₃, and 1 ml of the residue solution was added to 4 ml double-distilled 2% HNO₃. In a final step all solutions were spiked with 10 ppb indium as internal standard.

In order to ground truth the results of the carbonate solution measurements, approximately 170 mg of homogeneous carbonate cement were dissolved and subjected to solution ICP-MS. The same carbonate cement was analysed repeatedly by LA-ICP-MS. The two data sets correspond well, although concentrations measured by LA-ICP-MS are slightly higher (see below). Precision and accuracy were checked by replicate analysis of standard samples with standard deviation smaller than 5% for LA-ICP-MS and smaller than 10% for solution ICP-MS. The REE+Y concentrations were normalised against Post

Archaean Average Shale (PAAS; Taylor and McLennan, 1985). Subscript 'SN' denotes shale-normalised values. The cerium (Ce) anomaly was calculated as $Ce/Ce^* = 3Ce_{SN}/(2La_{SN} + Nd_{SN})$, according to Wright et al. (1987). Other elemental anomalies including lanthanum (La) and europium (Eu) were calculated as follows (cf. Bau and Dulski, 1996; Bolhar et al., 2004): $La/La^* = La_{SN}/(3Pr_{SN} - 2Nd_{SN})$; $Eu/Eu^* = Eu_{SN}/(0.67Sm_{SN} + 0.33Tb_{SN})$. REE_{SN}/REE_{SN}^* ratios higher than 1 indicate a positive anomaly and ratios smaller than 1 indicate a negative anomaly. Given the analytical uncertainties, we only consider REE_{SN}/REE_{SN}^* anomalies below 0.8 and above 1.2 to be significant. It should be noted that by calculating the Ce anomaly with La, the determined anomaly may be overestimated due to anomalous abundances of La itself. We still used the equation of Wright et al. (1987) in order to compare our results with previously reported data.

For bulk rock X-ray diffraction (XRD) analysis, a representative selection of crushed samples (fragments smaller than 1 cm) was pulverised in an agate mortar. XRD analysis of carbonate-cemented background sediment was performed on a pulverised sample obtained with a handheld micro-drill from a polished slab. XRD measurements were carried out at the Crystallography Department (University of Bremen), using a Philips X'Pert Pro MD X-ray diffractometer with a Cu-K α tube ($\lambda=1.541$; 45 kV, 40 mA). The carbonate content of the carbonate-cemented sediment was determined after Müller and Gastner (1971).

Samples for carbon and oxygen stable isotope analysis were taken from a polished slab with a handheld micro-drill. Sample powders were reacted with 100% phosphoric acid at 75°C, and the evolved CO₂ gas was analysed with a Finigan MAT 251 mass spectrometer at the University of Bremen. The $\delta^{13}C$ and $\delta^{18}O$ values are corrected according to the NBS19 standard and reported in per mill (‰) relative to the V-PDB (Vienna-PeeDee Belemnite) standard (standard deviation smaller than 0.04‰).

Table 1: Average REE+Y concentrations ($\mu\text{g/g}$) measured for NIST612 and BCR-2 standards by LA-ICP-MS with respective reference data (Pearce et al., 1997; GeoReM database: <http://georem.mpch-mainz.gwdg.de>, Jochum et al., 2005).

Elem ent	NIST612				BCR-2			
	This study		Pearce et al. (1997)		This study		GeoReM	
	Average (n=11)	SD (%)	Preferred average	SD (%)	Average (n=9)	SD ($\mu\text{g/g}$)	Preferred values	SD ($\mu\text{g/g}$)
La	36	2.75	35.77	2.15	24	0.3	24.9	0.2
Ce	38	2.58	38.35	1.64	51	0.6	52.9	0.2
Pr	37	2.31	37.16	0.93	6	0.1	6.7	0.1
Nd	35	1.97	35.24	2.44	27	0.5	28.7	0.1
Sm	37	1.40	36.72	2.63	6	0.2	6.58	0.02
Eu	34	1.34	34.44	1.59	1.8	0.05	1.96	0.01
Gd	37	2.60	36.95	1.06	6	0.2	6.75	0.03
Tb	36	3.05	35.92	2.68	1.0	0.03	1.07	0.03
Dy	36	2.14	35.97	0.82	6	0.1	6.41	0.05
Y	38	2.76	38.25	2.14	33	0.6	37	2
Ho	38	1.39	37.87	1.09	1.2	0.03	1.28	0.03
Er	37	1.17	37.43	1.5	4	0.1	3.66	0.01
Yb	40	1.01	39.95	2.86	3	0.1	3.38	0.02
Lu	38	1.08	37.71	1.95	0.5	0.02	0.503	0.009

4. Results

4.1. Carbonate mineralogy, petrography, and stable isotopes

4.1.1. Carbonate mineralogy

Bulk-rock powder X-ray diffractometry reveals aragonite as the dominant carbonate phase, with minor contributions of calcite and dolomite. Accessory non-carbonate minerals are muscovite, quartz, albite, and chlorite. Analysis of the micro-drilled powder shows that the carbonate-matrix cementing the hemipelagic background sediment is aragonite with minor contribution of calcite. The non-carbonate phases mainly comprise quartz, chlorite, albite, kaolinite, and muscovite. The carbonate content of one sample of the aragonite-cemented background sediment was 81%.

4.1.2. Carbonate petrography

The studied sample is mainly composed of authigenic aragonite occurring in three different varieties: (i) microcrystalline aragonite (Fig. 2A), (ii) brownish cryptocrystalline aragonite (Fig. 2B), and (iii) botryoidal aragonite (Figs. 2B, C). Microcrystalline aragonite and botryoidal aragonite represent the volumetrically dominant carbonate phases. Microcrystalline aragonite constitutes the cement for argillaceous hemipelagic background sediment (Fig. 2A).

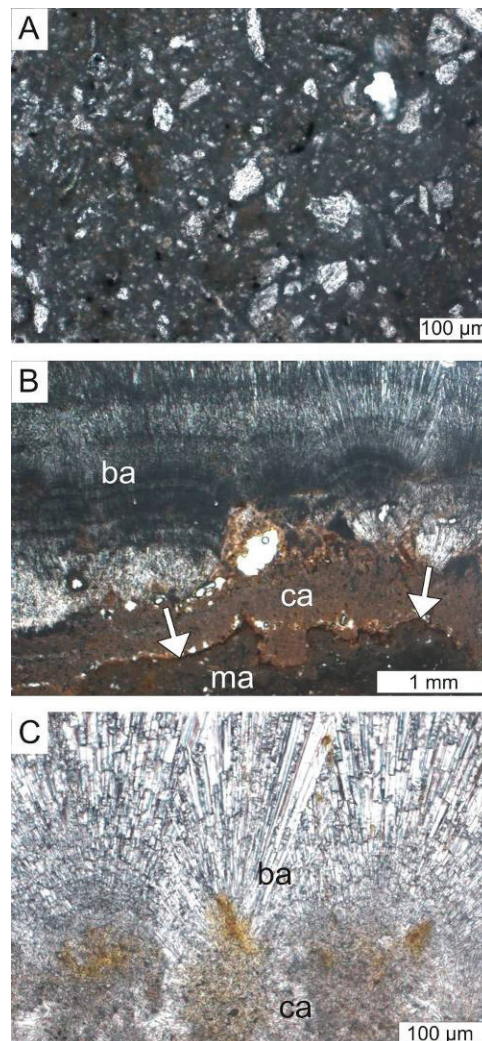


Fig. 2: Carbonate petrography. (A) Hemipelagic background sediment with silt-sized detritus in a matrix of microcrystalline aragonite. (B) Botryoidal aragonite (ba) growing on cryptocrystalline aragonite (ca); surface (arrows) coated by sulphide-minerals. (C) Aragonite botryoids (ba) originating on clots of cryptocrystalline aragonite (ca).

Microcrystalline aragonite cemented background sediment contains abundant silt-sized quartz detritus (Fig. 2A) and rare bioclasts (diatom frustules and foraminiferan tests). A sharp contact marked by sulphide mineral coatings separates this phase from cryptocrystalline aragonite (Fig. 2B). Cryptocrystalline aragonite (Figs. 2B, 3) consists of clotted aragonite crystal aggregates (diameters smaller than 30 μm; Figs. 2B, C, and 3A), forming a thin layer (less than 0.8 mm). At the contact between cryptocrystalline and botryoidal aragonite small pores occur (Fig. 2B). Under UV-radiation cryptocrystalline aragonite exhibits an

intense autofluorescence (Fig. 3B). Fibrous crystals of botryoidal aragonite form isopachous cement crusts with a diameter of more than 1 mm (Fig. 2B). Single aragonite botryoids originate from clots of cryptocrystalline aragonite (Fig. 2C). Abundant fluid inclusions are observed within the basal portion of botryoids, producing a faint lamination (Figs. 2B, 3A).

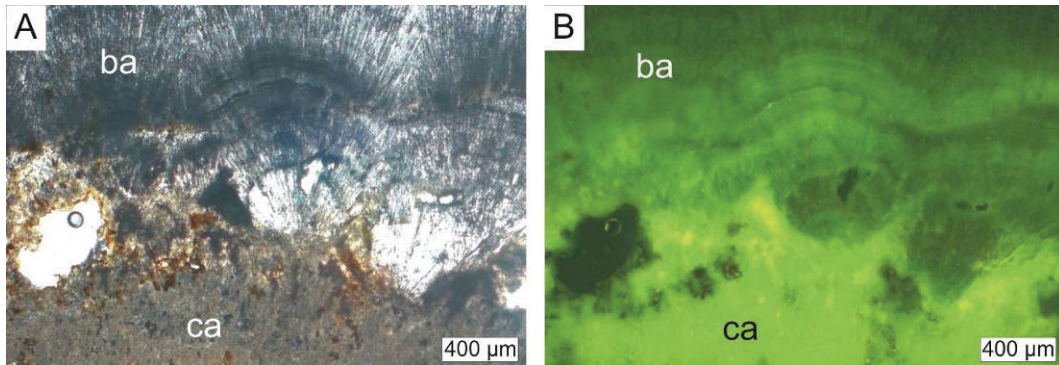


Fig. 3: Plane-polarised (A) and UV-fluorescence micrograph (B) of cryptocrystalline aragonite (ca) and botryoidal aragonite (ba). Inclusion rich areas within botryoidal aragonite show higher autofluorescence than clear areas with fewer inclusions; note intense autofluorescence of cryptocrystalline aragonite.

4.1.3. Carbon and oxygen stable isotopes

All samples yield exclusively negative $\delta^{13}\text{C}$ and positive $\delta^{18}\text{O}$ values, revealing only small isotopic variation (Fig. 4). Botryoidal aragonite is slightly more ^{13}C -depleted and more ^{18}O -enriched than microcrystalline aragonite. Botryoidal aragonite ($n = 7$) yields $\delta^{13}\text{C}$ values ranging from -49.0 to -44.0‰ (mean value: $-47.0 \pm 1.8\text{‰}$) and $\delta^{18}\text{O}$ values from 4.1 to 4.5‰ ($4.3 \pm 0.1\text{‰}$). Microcrystalline aragonite ($n = 6$) shows $\delta^{13}\text{C}$ values from -46.5 to -45.4‰ ($-46.0 \pm 0.4\text{‰}$) and $\delta^{18}\text{O}$ values from 3.6 to 4.0‰ ($3.8 \pm 0.1\text{‰}$). It was not possible to micro-drill the thin seam of cryptocrystalline aragonite for isotope analysis.

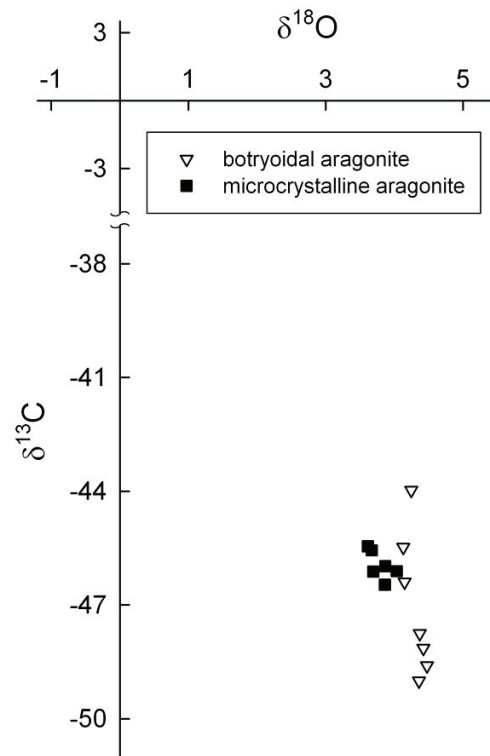


Fig. 4: Carbon and oxygen stable isotope plot of aragonite varieties.

4.2. Phase-specific REE+Y geochemistry

4.2.1. Solution ICP-MS

REE+Y concentrations obtained with solution ICP-MS are presented in Table 2. The shapes of shale-normalised REE+Y patterns clearly diverge (Fig. 5). The highest concentrations of $\Sigma\text{REE+Y}$ were measured in insoluble residue (182 and 173 $\mu\text{g/g}$), compared to microcrystalline aragonite (52 and 39 $\mu\text{g/g}$), and botryoidal aragonite (0.8 $\mu\text{g/g}$). Despite of the close spatial relationship of microcrystalline aragonite and non-carbonate minerals of the hemipelagic sediment, the shale-normalised patterns differ significantly between the dissolved aragonite phase and the insoluble residue (Fig. 5), revealing that only minor leaching or desorption processes of REEs from non-carbonate minerals occurred during aragonite dissolution. Furthermore, the measured carbonate content for aragonite-cemented sediment of this sample (81%) is in good

agreement with mass-balance calculation of dissolved carbonate (Table 2), pointing to complete aragonite dissolution. Shale-normalised REE+Y patterns of botryoidal aragonite obtained with solution ICP-MS and LA-ICP-MS are almost identical, confirming the consistency of the two methods applied (Fig. 5).

Table 2: REE+Y concentrations ($\mu\text{g/g}$) of microcrystalline aragonite cemented background sediment (non-carbonates and microcrystalline aragonite) and botryoidal aragonite obtained with solution ICP-MS.

Sample	A non-carbonates	B non-carbonates	A microcrystalline ara.	B microcrystalline ara.	Botryoidal aragonite
Dissolved material [mg]	27 (weighed)	25 (weighed)	126 (calculated)	128 (calculated)	171 (weighed)
La	31.6	33.2	6.6	4.9	0.2
Ce	59.5	62.3	13.9	10.3	0.09
Pr	7.0	7.4	2.0	1.5	0.03
Nd	26.2	27.4	8.7	6.6	0.1
Sm	5.3	5.7	2.7	2.0	0.03
Eu	1.1	1.2	0.6	0.4	0.006
Gd	4.6	4.8	2.6	2.0	0.02
Tb	0.7	0.7	0.3	0.3	0.003
Dy	4.1	4.3	1.8	1.4	0.01
Y	26.6	28.2	11.5	8.6	0.3
Ho	0.8	0.9	0.3	0.2	0.003
Er	2.4	2.6	0.8	0.6	0.009
Yb	2.5	2.5	0.7	0.5	0.01
Lu	0.4	0.4	0.1	0.1	0.001
$\Sigma\text{REE+Y}$	173	182	52	39	0.8
Y/Ho	32	32	37	35	93
Ce/Ce*	0.9	0.9	0.9	0.9	0.3
La/La*	1.0	1.0	1.0	1.1	2.2
Eu/Eu*	1.1	1.2	1.2	1.1	1.0

Microcrystalline aragonite is characterised by elevated middle REE (MREE) concentrations (i.e., Sm, Eu, Gd, Tb, Dy; $\text{Nd}_{\text{SN}}/\text{Dy}_{\text{SN}} = 0.7$), creating a ‘MREE bulge’ (Fig. 5). No distinct anomalies were observed for Ce, La, and Eu (Table 2). The Y/Ho ratio of microcrystalline aragonite is approximately 36 (Table 2).

Insoluble residues of aragonite-cemented sediment reveal flat shale-normalised REE+Y patterns ($\text{Pr}_{\text{SN}}/\text{Yb}_{\text{SN}} = 0.9$) without distinct Ce and La anomalies. Values for the Eu anomaly are similar to those of microcrystalline

aragonite, whereas the Y/Ho ratio is 32, which is close to the chondritic value of 28 (Bau, 1996).

The shale-normalised pattern of botryoidal aragonite displays a mild light REE (LREE) depletion ($Pr_{SN}/Yb_{SN} = 0.8$). Moreover, the pattern is characterised by (i) a strong negative Ce anomaly, (ii) a distinct positive La anomaly, and (iii) no Eu anomaly (Table 2). The Y/Ho ratio is 93, distinctly higher than that of the microcrystalline aragonite and similar to Y/Ho in seawater (between 44 and 77; Bau, 1996).

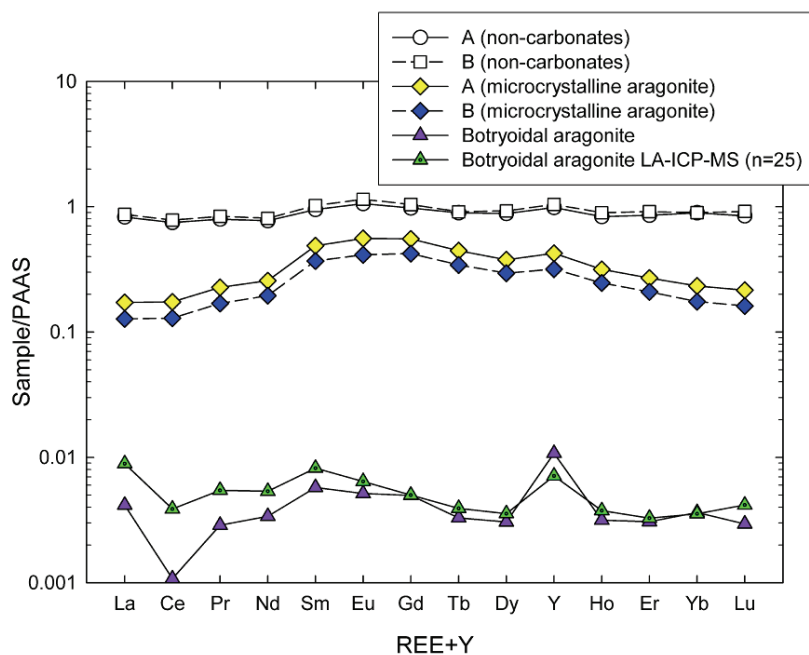


Fig. 5: Phase-specific shale-normalised REE+Y patterns obtained with solution ICP-MS.

4.2.2. Laser-ablation ICP-MS

Laser-ablation sampling allowed us to determine the REE+Y content of cryptocrystalline aragonite, which could not be sampled for solution ICP-MS measurements by micro-drilling. Moreover, LA-ICP-MS analyses of the botryoidal aragonite were used to investigate sub-millimetre scale compositional heterogeneity. Microcrystalline aragonite cementing sediment was also analysed by this technique, but as the obtained data represent mixed REE+Y signals of the microcrystalline aragonite and the non-carbonate minerals, they are not considered here.

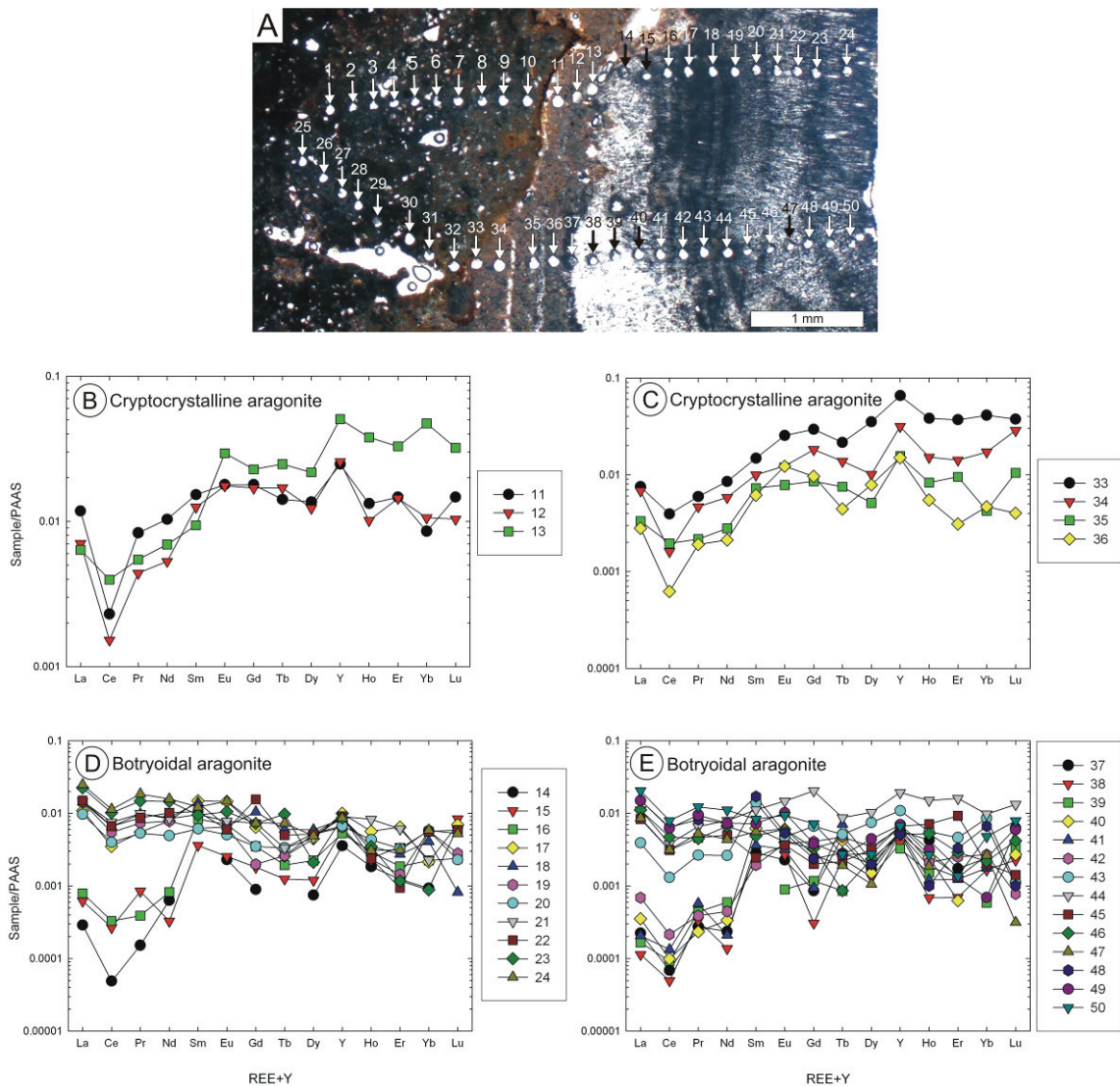


Fig. 6: Shale-normalised REE+Y patterns of single-spot analysis. (A) Thin section showing laser craters produced during laser ablation. (B) and (C) show shale-normalised patterns of cryptocrystalline aragonite (craters 11 to 13 and 33 to 36, respectively), (D) and (E) show the patterns of botryoidal aragonite (14 to 24 and 37 to 50).

Cryptocrystalline aragonite ($n = 7$) shows low to intermediate total REE+Y concentrations with values in the range of 0.8 to 3.4 ppm (average = 1.9 ± 0.9). The REE+Y patterns are characterised by distinct LREE depletion (average $Pr_{SN}/Yb_{SN} = 0.4 \pm 0.3$) with pronounced negative Ce and strongly positive La anomalies (Table 3; Figs. 6B, C). Europium anomalies are exclusively positive and the Y/Ho ratios vary between 36 and 75 with an average of 55 ± 12 .

Botryoidal aragonite ($n = 25$) yields much lower total REE+Y concentrations with values between 0.1 to 3.0 ppm (1.2 ± 0.8) than cryptocrystalline aragonite. High-resolution probing revealed an increase of total REE+Y concentration along with the direction of aragonite crystal growth (Figs. 6D, E). The shale-normalised REE+Y patterns display progressive LREE enrichment during aragonite crystal growth with Pr_{SN}/Yb_{SN} ratios increasing from 0.1 up to 4.4 (1.4 ± 1.2). Samples 23 and 49 yielded relatively low Yb concentrations, leading to abnormally high Pr_{SN}/Yb_{SN} ratios (Table 3). Y/Ho ratios are strongly variable, ranging from 26 to 141, but have an average value (67 ± 33) similar to that of the cryptocrystalline aragonite. Exclusively negative Ce anomalies are developed, while La anomalies range between positive (up to 2.7) and negative (as low as 0.2) values. Europium anomalies vary between 0.4 to 1.8.

Table 3: Phase-specific REE+Y concentration in ($\mu\text{g}/\text{kg}$) measured with LA-ICP-MS; 'bd': below detection limit, 'nc': not calculated; numbers in italics were not used for calculation of mean values and standard deviation (SD).

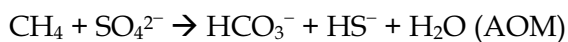
Spot	Lithology	La	Ce	Pr	Nd	Sm	Eu	Gd	Tb	Dy	Y	Ho	Er	Yb	Lu	Σ REE + Y ($\mu\text{g}/\text{g}$)	Y/Ho	Ce/Ce*	La/La*	Eu/Eu*	Pr ₉₀₀ /M ₉₀₀ S
11	Cryptocrystalline aragonite	449	183	73.6	350	84.8	19.3	83.4	10.9	63.7	667	13.1	41.8	24.1	6.34	2.1	51	0.2	2.7	1.2	1.0
12	Cryptocrystalline aragonite	269	121	38.8	180	69.5	19.0	78.9	13.2	57.7	696	10.0	41.1	29.8	4.48	1.6	69	0.2	2.7	1.3	0.4
13	Cryptocrystalline aragonite	243	315	48.2	235	52.1	31.8	106	19.2	102	1367	37.6	93.8	133	13.9	2.8	36	0.6	2.5	2.0	0.1
33	Cryptocrystalline aragonite	286	313	52.5	287	82.4	27.4	137	16.6	164	1770	37.8	105	116	16.3	3.4	47	0.5	8.2	1.5	0.1
34	Cryptocrystalline aragonite	260	128	41.3	198	55.2	13.2	84.9	10.7	47.1	850	15.0	40.4	48.4	12.4	1.8	57	0.2	2.9	1.1	0.3
35	Cryptocrystalline aragonite	127	156	19.1	94.7	40.4	8.45	39.8	5.81	23.9	421	8.22	27.1	12.0	4.52	1.0	51	0.6	3.7	1.1	0.5
36	Cryptocrystalline aragonite	107	49.4	16.8	71.6	34.1	13.2	44.9	3.43	36.7	404	5.42	8.82	13.1	1.74	0.8	75	0.2	1.9	2.2	0.4
											Mean value					1.9	55	0.4	3.5	1.5	0.4
											SD					0.9	12	0.2	2.0	0.4	0.3
14	Botryoidal aragonite	11.0	bd	1.34	21.5	bd	2.48	4.17	bd	3.48	96.1	1.82	3.52	2.62	2.82	0.2	1.82	0.3	nc	0.2	0.2
15	Botryoidal aragonite	23.6	21.3	7.48	11.1	20.1	2.74	8.42	1.0	5.62	159	2.37	9.94	bd	3.64	0.3	67	0.5	0.3	0.9	nc
16	Botryoidal aragonite	30.2	26.2	3.44	28.0	46.2	7.57	16.3	15.0	10.5	144	2.92	5.30	6.30	1.03	0.3	49	0.4	-1.6	1.1	0.2
17	Botryoidal aragonite	415	278	48.4	265	82.4	15.7	30.1	1.99	20.8	271	5.58	18.4	6.02	3.03	1.5	48	0.4	13.5	1.3	2.6
18	Botryoidal aragonite	546	526	86.8	296	77.8	7.19	48.8	4.65	27.8	223	3.50	7.76	11.5	0.35	1.9	64	0.5	1.2	0.6	2.4
19	Botryoidal aragonite	542	435	64.8	265	34.5	6.97	9.21	2.02	24.1	172	2.29	4.12	16.0	1.22	1.6	75	0.5	2.2	1.3	1.3
20	Botryoidal aragonite	371	317	46.7	167	33.9	5.47	16.2	2.60	24.6	181	4.28	9.34	16.2	1.00	1.2	42	0.5	1.6	1.0	0.9
21	Botryoidal aragonite	562	598	87.3	285	53.3	8.43	34.3	2.56	21.3	243	8.17	17.3	6.41	bd	1.9	30	0.6	1.1	1.0	4.4
22	Botryoidal aragonite	573	529	76.2	345	58.8	6.45	72.6	3.87	24.0	245	2.35	2.66	15.8	2.55	2.0	104	0.5	2.7	0.7	1.5
23	Botryoidal aragonite	858	809	130	496	52.6	11.4	33.7	7.56	9.92	233	3.45	3.35	2.48	bd	2.7	67	0.5	1.5	1.1	16.8
24	Botryoidal aragonite	949	906	163	534	67.7	15.9	34.3	5.66	22.9	232	3.06	8.90	16.5	2.27	3.0	76	0.5	1.0	1.4	3.2
37	Botryoidal aragonite	8.54	5.44	2.42	8.0	15.9	2.45	3.98	3.68	8.17	155	4.22	4.94	6.8	2.71	0.2	37	0.3	0.6	0.6	0.1
38	Botryoidal aragonite	4.33	3.93	2.96	4.64	bd	2.92	1.43	1.82	6.22	104	0.678	1.98	4.67	0.98	0.1	154	0.4	0.2	nc	0.2
39	Botryoidal aragonite	6.34	7.32	3.87	20.1	bd	0.966	5.50	0.659	bd	88.3	1.51	bd	1.65	1.46	0.1	58	0.3	1.3	nc	0.7
40	Botryoidal aragonite	13.4	7.89	2.06	11.4	34.5	4.34	15.5	3.27	7.07	146	2.43	1.78	bd	1.17	0.3	60	0.3	11.7	0.7	nc
41	Botryoidal aragonite	7.86	10.6	5.04	7.09	20.1	3.44	4.35	5.46	10.3	151	1.20	3.51	4.97	bd	0.2	126	0.6	0.2	0.7	0.3
42	Botryoidal aragonite	26.4	17.1	3.42	15.1	10.7	4.17	19.0	3.65	16.2	167	2.09	7.14	7.61	0.335	0.3	80	0.4	2.5	1.4	0.1
43	Botryoidal aragonite	149	104	23.4	88.9	77.7	5.08	30.8	3.96	34.8	293	5.54	13.1	24.1	0.480	0.9	53	0.4	1.4	0.4	0.3
44	Botryoidal aragonite	426	302	57.9	269	62.0	16.0	95.3	6.72	48.2	522	14.9	45.7	27.5	5.75	1.9	35	0.4	2.9	1.4	0.7
45	Botryoidal aragonite	318	248	40.6	171	13.6	3.95	9.32	1.68	14.9	180	7.05	26.3	5.60	0.617	1.0	26	0.4	2.2	1.6	2.3
46	Botryoidal aragonite	424	374	39.8	226	27.1	6.52	15.3	0.667	10.9	138	5.16	8.24	6.14	1.80	1.3	27	0.5	56.6	1.7	2.1
47	Botryoidal aragonite	328	251	46.4	148	31.1	6.59	12.4	1.48	4.94	142	1.84	3.73	7.42	0.136	1.0	77	0.4	1.2	1.4	2.0
48	Botryoidal aragonite	573	511	72.4	247	94.6	5.81	11.1	2.19	9.32	140	0.989	9.39	18.7	0.437	1.7	141	0.5	1.5	0.4	1.2
49	Botryoidal aragonite	573	496	83.4	247	40.1	10.9	17.8	2.05	20.7	188	3.13	3.72	1.95	2.58	1.7	60	0.5	1.1	1.8	13.7
50	Botryoidal aragonite	782	630	108	375	46.1	10.1	33.8	2.11	12.8	180	2.65	3.89	13.5	3.41	2.2	68	0.5	1.4	1.4	2.6
											Mean value					1.2	67	0.4	1.4	1.1	1.4
											SD					0.8	33	0.1	0.8	0.4	1.2

5. Discussion

Aragonite is the major carbonate phase of the investigated seep limestone from the Makran accretionary prism. It occurs as (i) microcrystalline aragonite, (ii) cryptocrystalline aragonite, and (iii) botryoidal aragonite, which all show distinct shale-normalised REE+Y patterns (Figs. 5 and 6). The observed REE+Y concentrations are all in the range of previously reported REE concentrations in authigenic methane-seep carbonates (Feng et al., 2008; 2009a;b; 2010).

5.1. Environment of carbonate formation

Carbonate formation at methane-seeps is induced by increased carbonate alkalinity resulting from the anaerobic oxidation of methane (AOM) following the reactions:



Methane is extremely depleted in ^{13}C ($\delta^{13}\text{C}$ values: -110 to -50‰ for microbial methane; -50 to -20‰ for thermogenic methane; Whiticar, 1999). Due to kinetic isotope fractionation during AOM, i.e. faster oxidation of methane with the ^{12}C isotope ($1.002 < \alpha < 1.014$, Whiticar and Faber, 1986), the resulting bicarbonate is even more ^{13}C depleted than the parent methane. Negative $\delta^{13}\text{C}_{\text{carbonate}}$ values lower than -30‰ are characteristic for methane-seep carbonates (e.g., Peckmann and Thiel, 2004), and have been frequently reported from seep deposits along many continental margins (e.g., Bohrmann et al., 1998; Teichert et al., 2005; Naehr et al., 2007; Pierre and Fouquet, 2007). The extremely negative $\delta^{13}\text{C}$ values (as low as -49‰) of the seep carbonates investigated in this study are similar to previously reported values from the Makran accretionary prism (von Rad et al., 1996). These low $\delta^{13}\text{C}$ values indicate that a significant fraction of the bicarbonate in the pore waters derived from AOM (cf. Peckmann and Thiel, 2004). The $\delta^{13}\text{C}$ signal of authigenic carbonates is intermediate between that of seep methane on the one hand and sedimentary organic matter and seawater dissolved inorganic carbon (DIC) on the other hand and reflects mixing of bicarbonate from different sources. AOM is the source of the ^{12}C -depleted bicarbonate, while bicarbonate

relatively enriched in ^{13}C may be due to inorganic carbon dissolved in seawater or bicarbonate produced during degradation of organic matter (cf. Formolo et al., 2004; Naehr et al., 2007). The mixing proportions cannot be constrained, but the observed $\delta^{13}\text{C}$ values as low as -49‰ indicate that oxidation of microbial methane must be a significant contributor to the inorganic carbon pool of the pore waters.

More information about environmental conditions during carbonate formation can be deduced from the oxygen stable isotope composition of seep carbonates (e.g., Han et al., 2004, Teichert et al., 2005). However, the interpretation of $\delta^{18}\text{O}_{\text{carbonate}}$ values is not straightforward as the oxygen isotope composition of carbonates is a function of several environmental factors including temperature, carbonate mineralogy, pore water $\delta^{18}\text{O}$ values, and pore water pH (Epstein et al., 1953; Grossman and Ku, 1986). A factor that may be particularly relevant at methane-seeps is the dissociation of gas hydrate, leading to the liberation of ^{18}O enriched waters (Davidson et al., 1983) and thus to higher $\delta^{18}\text{O}_{\text{carbonate}}$ values (Bohrmann et al., 1998; Aloisi et al., 2000; Pierre and Fouquet, 2007). Another potential factor is the dehydration of clay-minerals in deeper parts of marine sediments which also releases ^{18}O -enriched water (Dählmann and de Lange, 2003). By contrast, formation of authigenic ^{18}O -enriched clay minerals during alteration of basaltic rocks or volcanic ash within the sub-seafloor sediment leads to decrease in $\delta^{18}\text{O}$ values of pore water (Matsumoto, 1992).

The $\delta^{18}\text{O}$ values of the studied carbonates are exclusively positive with microcrystalline aragonite showing slightly lower values ($3.8 \pm 0.1\text{‰}$) than botryoidal aragonite ($4.3 \pm 0.1\text{‰}$). In order to test if aragonite precipitated from ^{18}O -enriched, ^{18}O -depleted pore waters, or in equilibrium with seawater, we calculated the isotopic composition of the aragonite-precipitating fluid using the following equation (Han et al., 2004):

$$\delta^{18}\text{O}_{\text{fluid}} (\text{SMOW}) = \delta^{18}\text{O}_{\text{aragonite}} (\text{PDB}) - (19.7 - t)/4.34$$

We used the current bottom water temperature (t) at the sampling site of approximately 4.6°C (Bohrmann et al., 2008). The calculated $\delta^{18}\text{O}_{\text{fluid}}$ values vary

between 0.1 and 1‰ (microcrystalline aragonite: $\delta^{18}\text{O} = 0.3 \pm 0.2\text{‰}$ SMOW; botryoidal aragonite: $\delta^{18}\text{O} = 0.8 \pm 0.1\text{‰}$ SMOW), and cover the range of seawater $\delta^{18}\text{O}$ values between glacial ocean water (approximately 1.0‰ SMOW, Fairbanks, 1989) and modern seawater (approximately 0‰ SMOW). Therefore, the carbonates apparently precipitated within sediments in close proximity to the seafloor in equilibrium with seawater. Similar $\delta^{13}\text{C}$ and $\delta^{18}\text{O}$ values have been suggested to indicate rapid ascent of methane causing entrainment of seawater in shallow subsurface sediments (Han et al., 2004). The large amount of early diagenetic cement in the studied seep carbonate supports such a scenario, indicating high seepage intensity (cf. Peckmann et al., 2009).

5.2. Composition of early diagenetic fluids deduced from REE+Y_{carbonate} geochemistry

5.2.1. *Microcrystalline aragonite*

Precipitation of methane-derived microcrystalline aragonite resulted in the lithification of the hemipelagic background sediment. Because microcrystalline aragonite and background sediment were too finely interspersed to allow analyses by LA-CP-MS, aragonite dissolution followed by solution ICP-MS analysis was applied to investigate the REE+Y content of microcrystalline aragonite.

Microcrystalline aragonite reveals significantly high total REE+Y concentrations and a distinct shale-normalised pattern, which differs from those of later cryptocrystalline and botryoidal aragonite cements. Concentrations of MREEs (Sm, Eu, Gd, Tb, Dy) are exceptionally high and form a 'MREE bulge' in shale-normalised REE+Y patterns. These patterns contrast those of the non-carbonate minerals, which exhibit the flat REE+Y pattern expected for clastic sediments derived from continental crust (cf. Taylor and McLennan, 1985). Haley et al. (2004) investigated REEs in marine pore waters and showed that anoxic pore waters are characterised by higher REE concentrations than seawater and a significant MREE enrichment (their Figs. 2 and 5). They suggested that the MREE

enrichment is caused by the reduction of Fe-oxides during early diagenesis in anoxic sediments. This MREE enrichment can be inherited by diagenetic precipitates that in turn act as sinks for REEs (Haley et al., 2004). Feng et al. (2008; 2009b) reported similar MREE-enriched patterns for methane-derived microcrystalline aragonite in the same concentration range, but no explanation for their development was given.

The negative $\delta^{13}\text{C}$ values ($-46.0 \pm 0.4\text{‰}$) reveal that most of the carbonate ions involved in the precipitation of microcrystalline aragonite derived from AOM. With regard to the narrow range of $\delta^{13}\text{C}$ values a relatively low but constant admixture of isotopically heavier DIC is indicated. On the one hand, the calculated $\delta^{18}\text{O}_{\text{fluid}}$ values point to precipitation of microcrystalline aragonite in equilibrium with seawater while the REE+Y data, on the other hand, imply that anoxic pore waters of the iron reduction zone constitute the main fluid source. We suggest that the relatively high total REE+Y concentration and the MREE enrichment of microcrystalline aragonite are best explained by precipitation from MREE-enriched anoxic pore fluids close to or within the zone of iron reduction. In redox-stratified marine sediments the zone of iron reduction usually directly overlies the zone of sulphate reduction (e.g., Froelich et al., 1979) where sulphate-dependent AOM occurs. Remarkably, Beal et al. (2009) showed that AOM can also be coupled to iron reduction and not only to sulphate reduction. Therefore it seems likely that either iron reduction was preceding sulphate-dependent AOM or that part of AOM was directly coupled to iron reduction.

5.2.2. *Cryptocrystalline aragonite*

Shale-normalised REE+Y patterns of cryptocrystalline aragonite differ from those of microcrystalline aragonite in that they show strong enrichment of HREEs over LREEs ($\text{Pr}_{\text{SN}}/\text{Yb}_{\text{SN}} = 0.4 \pm 0.3$), super-chondritic Y/Ho ratios ($\text{Y}/\text{Ho} = 55 \pm 12$), and pronounced REE anomalies, particularly for lanthanum (positive La anomaly = 3.5 ± 2), cerium (negative Ce anomaly = 0.4 ± 0.2), and europium (positive Eu anomaly = 1.5 ± 0.4). Except for positive Eu anomalies, these patterns reflect the behaviour of REEs in modern oxygenated seawater (Byrne and Kim,

1990; de Baar et al., 1985; Sholkovitz et al., 1994; Bau, 1996; Alibo and Nozaki, 1999), including seawater of the northwestern Indian Ocean (German and Elderfield, 1990). This indicates a seawater-like composition of the parental fluids of cryptocrystalline aragonite. However, HREE enrichment is also observed in marine pore waters (Haley et al., 2004) due to enhanced REE release resulting from degradation of organic matter and subsequent HREE complexation with carbonate ions in solution (cf. Byrne and Kim, 1990; Sholkovitz et al., 1994).

Although an evaluation of the relative influence of pore waters versus seawater during the precipitation of cryptocrystalline aragonite is problematic, there are some observations that indicate strong influence of pore waters. Pore waters show significantly higher REE concentrations than seawater (Haley et al., 2004). The concentration of HREEs in cryptocrystalline aragonite is relatively high compared to seawater values, being only slightly lower than REE signals of microcrystalline aragonite. The intense autofluorescence of cryptocrystalline aragonite (Fig. 3B) points to a high content of organic matter, which is also more typical of pore waters than of seawater. Additional evidence for precipitation of cryptocrystalline aragonite from anoxic pore waters stems from the analysis of lipid biomarkers. Leefmann et al. (2008) reported high concentrations of AOM-specific biomarkers in a cryptocrystalline variety of aragonite that is similar to the seams of cryptocrystalline aragonite discussed here. Because high contents of lipid biomarkers and intense autofluorescence are more typical for the microcrystalline matrix of seep limestones rather than for later botryoidal aragonites, an environment of formation of cryptocrystalline aragonite more similar to that of the pore water-imprinted microcrystalline aragonite seems likely. Although the majority of observations argue for stronger influence of pore waters than seawater, the high Y/Ho ratios (55 ± 12) of cryptocrystalline aragonite, on the other hand, confirm that at least some influence of seawater cannot be excluded.

Considering that AOM – a process requiring strictly anoxic conditions – promoted the precipitation of cryptocrystalline aragonite, the origin of pronounced negative Ce anomalies is ambiguous (cf. Brookins, 1989). Negative

Ce anomalies are typical of well-oxygenated seawater, where dissolved Ce^{3+} is microbially oxidised to more stable Ce^{4+} , which is readily scavenged (Moffett, 1990; Sholkovitz et al., 1994). Negative Ce anomalies in methane-seep carbonates have been ascribed to episodic oxic conditions and seawater influence during carbonate formation at times of low seepage fluxes (Feng et al., 2008; 2009a,b; 2010). It is, however, difficult to exclude other factors that could influence Ce speciation. Pourret et al. (2008) demonstrated that negative Ce anomalies and HREE enrichment are features of alkaline solutions. These patterns are believed to result from increased HREE solubility due to carbonate complexation and the scavenging of Ce^{4+} by humic acids. Considering that seep carbonates result from an increase of alkalinity due to AOM (e.g., Ritger et al., 1987; Peckmann and Thiel, 2004), it seems feasible that the negative Ce anomalies and the HREE enrichment in cryptocrystalline aragonite reflect high pore water alkalinity in combination with the presence of organic matter rather than oxygenation.

5.2.3. Botryoidal aragonite

Shale-normalised REE+Y patterns of early growth stages of botryoidal aragonite (Figs. 6D, E) are similar to those of cryptocrystalline aragonite, showing pronounced LREE depletion. Other than cryptocrystalline aragonite, the composite REE+Y pattern of botryoidal aragonite (= average values of normalised REE+Y, data not shown; Fig. 5) reveals HREE depletion similar to patterns of aragonite cement in other seep limestones (Feng et al., 2008; their Fig. 8). Botryoidal aragonite shows considerably lower LREE and total REE+Y concentrations than cryptocrystalline aragonite, implying a significant change in the REE+Y source of the fluid. Based on the pronounced LREE depletion and relatively lower total REE+Y concentrations, a seawater source of REE+Y seems likely and is in good agreement with the calculated super-chondritic Y/Ho ratios and the distinct negative Ce anomalies. Moreover, the relatively wide range of $\delta^{13}\text{C}$ values of botryoidal aragonite indicates variable admixture of ^{13}C -enriched carbonate species (e.g., among others seawater DIC), agreeing with an increased influence of seawater. During later growth stages of botryoidal aragonite, the

fluid composition changed as revealed by the progressive LREE enrichment and increase of total REE concentration. The LREE enrichment observed for the late growth stages of botryoidal aragonite may have been caused by continuing degradation of organic matter releasing LREEs > HREEs into pore waters (Haley et al., 2004). In such a scenario, precipitation of botryoidal aragonite was initially dominated by seawater and subsequently during the formation of later growth stages by endemic seep-influenced pore waters. As botryoidal aragonite fills cracks, brittle failure of the limestone matrix and seawater ingress was preceding its precipitation. During later stages of crystal growth the cracks were successively sealed leading to gradually more restricted pore water-dominated conditions.

6. Conclusions

Distinct variation in $\sum\text{REE+Y}$ concentrations and shale-normalised patterns of methane-derived authigenic carbonates can be used to decipher changes in the composition of pore fluids from which carbonate minerals precipitate at seeps. Seep carbonates from an active seep on the Makran accretionary prism in 1656 m water depth proved to be well suited for studying the geochemical evolution during diagenesis, because their paragenetic sequence consists only of one carbonate mineralogy. On the one hand, the minor offset between $\delta^{13}\text{C}$ and $\delta^{18}\text{O}$ values between the first and the latest precipitates (i.e., microcrystalline and botryoidal aragonite) reveals that the composition of the respective pore fluids was close to seawater and that the relative contributions of different carbon sources were similar. On the other hand, the phase specific $\sum\text{REE+Y}$ contents of the three aragonite phases were found to vary strongly, revealing distinctly different shale-normalised patterns. The latter findings point to significant changes of pore fluid composition in the course of early diagenetic carbonate formation. Our results confirm that $\text{REE+Y}_{\text{carbonate}}$ data provide information that are critical for the understanding of early diagenetic carbonate formation at methane-seeps, in particular when combined with carbon and oxygen stable isotope data. Because $\text{REE+Y}_{\text{carbonate}}$ signals are exceptionally stable during later

stages of diagenesis and even carbonate recrystallisation (cf. Webb et al., 2009), such data are particularly useful for reconstructing early diagenetic pathways in ancient sedimentary environments. Based on the results of this study, the following conclusions can be drawn:

1. Early diagenetic authigenic carbonates from the Makran accretionary prism formed at methane-seeps near to the sea floor as a result of anaerobic oxidation of microbial methane.
2. Aragonite is the dominant carbonate species, occurring as (i) microcrystalline aragonite (cementing background sediment), (ii) cryptocrystalline aragonite, and (iii) botryoidal aragonite.
3. The combination of solution ICP-MS and LA-ICP-MS revealed distinct shale-normalised REE+Y_{aragonite} patterns that indicate variable pore fluid composition during carbonate authigenesis: Early microcrystalline aragonite yielded the highest REE+Y concentrations and a distinct 'MREE bulge', reflecting anoxic pore waters. The MREE enrichment indicates that iron reduction occurred before or during the lithification of the background sediment by microcrystalline aragonite. (i) HREE enrichment, (ii) a pronounced negative Ce anomaly putatively resulting from high alkalinity induced by anaerobic oxidation of methane favouring scavenging of Ce⁴⁺ by humic acids, and (iii) high REE concentrations indicate pore water as dominant REE+Y source of cryptocrystalline aragonite with minor seawater influence. A distinct change from pore water to seawater dominated REE+Y patterns followed the precipitation of cryptocrystalline aragonite as revealed by high-resolution probing of botryoidal aragonite, which shows significantly lower total REE+Y concentrations and seawater-like patterns, indicating seawater as dominant REE+Y source during initial growth of botryoids. Progressive LREE enrichment during later stages of botryoidal aragonite growth suggests that the REE+Y source diverged again from seawater to LREE enriched seep-influenced pore waters.

Acknowledgements

This study is part of the first author's doctoral thesis at the University of Bremen. We greatly appreciate the invaluable support of the master and crew on R/V METEOR cruise M74/3, and the skilful work of the ROV MARUM-QUEST4000 team during sample recovery. TH owes gratitude to Heike Anders and Andreas Klügel (both University of Bremen) for offering their patient support during analytical preparations and ICP-MS measurements. We are thankful for the important contributions of Monika Segl (stable isotope measurements), Sebastian Flotow (preparation of thin sections), and Christoph Vogt (XRD-analysis; all University of Bremen). We thank the editor Jeremy Fein, as well as Brian Haley and one anonymous reviewer for constructive comments. Financial support was provided by the Deutsche Forschungsgemeinschaft (DFG) through the DFG-Research Center / Excellence Cluster "The Ocean in the Earth Systems"

2.2 Manuscript 2

Corrosion patterns of seep-carbonates from the eastern Mediterranean Sea

Tobias Himmler¹, Florian Brinkmann¹, Gerhard Bohrmann¹ and Jörn Peckmann²

¹*MARUM–Center for Marine Environmental Sciences and Faculty of Geosciences, University of Bremen, PO Box 330 440, 28334 Bremen, Germany*

²*Department of Geodynamics and Sedimentology, Center for Earth Sciences, University of Vienna, 1090 Vienna, Austria*

Submitted December 2010 to *Terra Nova*; revised version submitted March 2011.

Abstract

Porous seep-carbonates are exposed at mud volcanoes (MV) in the eastern Mediterranean Sea. The ^{13}C -depleted aragonitic carbonates formed as a consequence of the anaerobic oxidation of methane in a shallow sub-surface environment. Besides the macroscopically visible cavernous fabric, extensive carbonate corrosion was revealed by detailed analysis. After erosion of the background sediments, the carbonates became exposed to oxygenated bottom waters that are periodically influenced by the release of methane and upward diffusion of hydrogen-sulphide. We suggest that carbonate corrosion resulted from acidity locally produced by aerobic oxidation of methane and hydrogen-sulphide in the otherwise with respect to aragonite oversaturated bottom waters. Although it remains to be tested, if the mechanisms of carbonate dissolution suggested here are valid, this study reveals that a better estimate on the significance of corrosion is required in order to assess the amount of methane-derived carbon that is permanently fixed in seep-carbonates.

1. Introduction

Submarine mud volcanoes (MV) release huge amounts of methane into the water column, constituting pathways for ascending and degassing of overpressured buried sediments along convergent continental margins (Milkov, 2000; Dimitrov, 2002; Kopf, 2002; Reeburgh, 2007). The compressional tectonic regime in the eastern Mediterranean Sea gives rise to numerous MV in the tectonically active region of the Anaximander seamounts southwest off Turkey, including the Amsterdam and Athina MV (Fig. 1; Woodside et al., 1998; Lykousis et al., 2009). Seepage of methane in the Anaximander seamount region has been reported based on high concentrations of dissolved methane in bottom waters (Charlou et al., 2003) and large acoustic plumes caused by methane bubbles in the water column (Bohrmann et al., 2008). Manifestations of seepage comprise endemic benthic communities of chemosymbiotic bivalves and tube worms (Olu-Le Roy et al., 2004; Carlier et al., 2010).

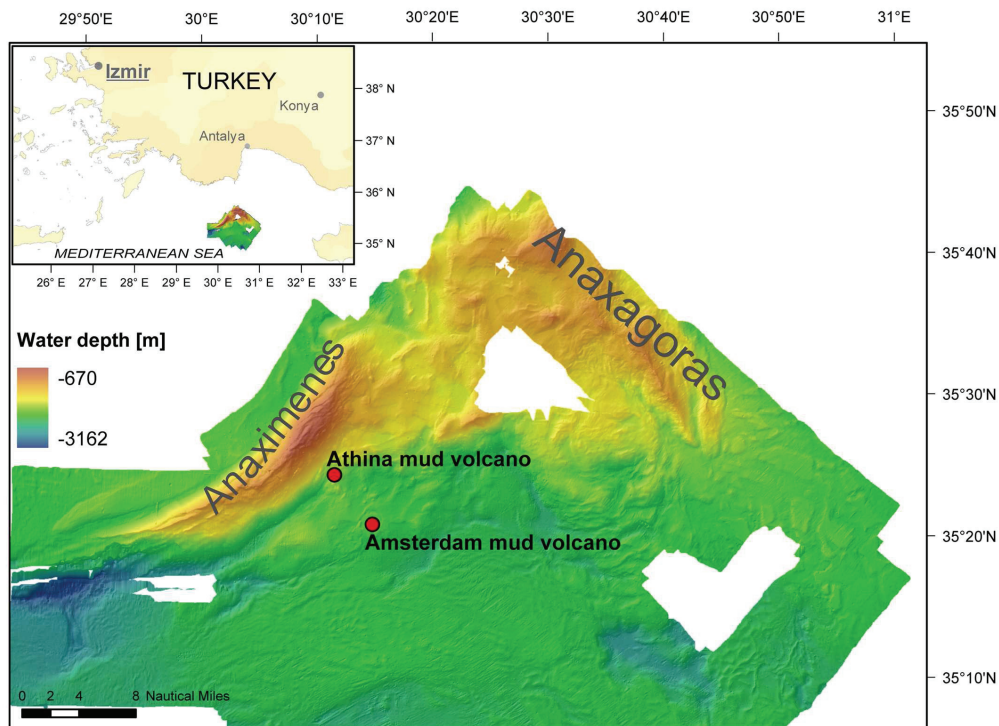


Fig. 1: Location of the Anaximander seamounts in the eastern Mediterranean Sea (box upper left) and detailed bathymetry map showing positions of Amsterdam and Athina mud volcanoes; Anaximenes and Anaxagoras represent individual ranges of the Anaximander seamounts.

At various locations worldwide past seepage is documented by authigenic seep-carbonates (e.g., Campbell, 2006). Seep-carbonates form when methane-charged pore waters meet the subsurface sulphate-reduction zone. Thereby, microbially mediated sulphate-dependent anaerobic oxidation of methane (AOM) increases carbonate alkalinity, resulting in the precipitation of carbonates within anoxic sediments (e.g., Ritger et al., 1987; Paull et al., 1992; Boetius et al., 2000). Large, yet on a global scale poorly quantified amounts of methane-derived carbon are incorporated into authigenic seep-carbonates (e.g., Formolo et al., 2004). Carbonate crusts of varying thickness between a few centimetres and several decimetres cover wide areas on the seafloor at the Amsterdam and Athina MV (Fig. 2). Aloisi et al. (2000; 2002) reconstructed the early diagenetic processes that led to the formation of carbonate crust at the eastern Mediterranean MV. Based on mineralogical and geochemical data, it was concluded that the carbonates formed as a result of AOM within anoxic mud-flow deposits near to the sediment-water interface.

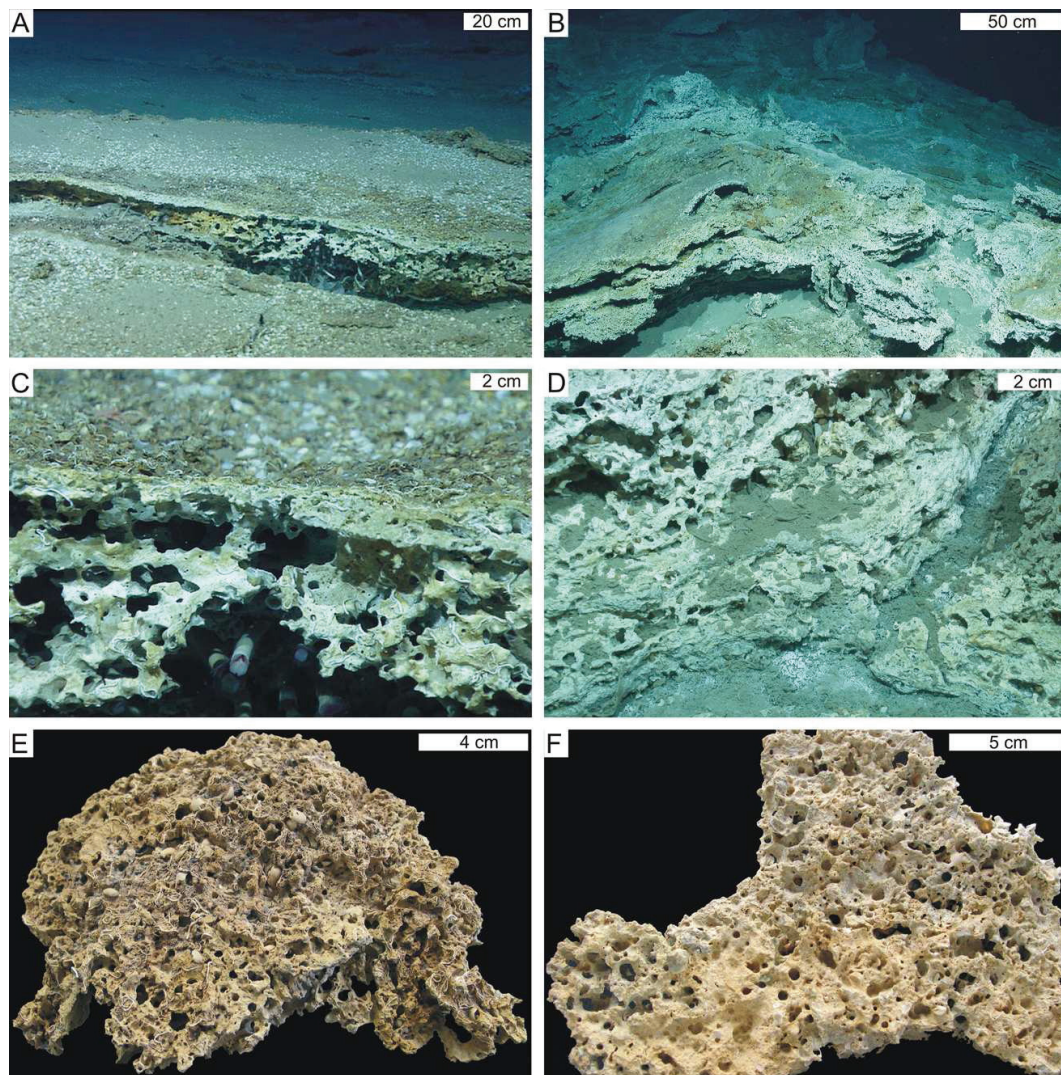


Fig. 2: (A) Carbonate pavement exposed at Amsterdam mud volcano. (B) Gently curved carbonate layer at Athina mud volcano. (C) Close-up of (A), showing large pores and living tube-worms; note that the surface is covered with abundant mollusc shells and serpulid tubes. (D) Close-up of (B), showing porous carbonates partly covered with sediment. (E) and (F) Porous carbonate samples recovered from Amsterdam (E, internal sample-code GeoB 11308-1) and Athina (F, GeoB 11319-2) sites.

A significant, yet unaddressed, textural feature of the seep-carbonates at the Amsterdam and Athina MV is their significant secondary porosity. Modern porous aragonitic seep-carbonates have been recognized at some seeps worldwide, e.g., off Baffin Island, northeast Canada (Matsumoto, 1990), at the Costa Rica margin (Han et al., 2004), on Hydrate Ridge, offshore Oregon, USA (Teichert et al., 2005), and associated with asphalt volcanoes in the Gulf of Mexico (Naehr et al., 2009). Despite the fact that early diagenetic corrosion

features are common in ancient seep-carbonates (e.g., Beauchamp and Savard, 1992; Campbell, et al., 2002; Peckmann et al., 2003), modern examples of corrosion are surprisingly scarce (e.g., Matsumoto, 1990; Han et al., 2004; Naehr et al., 2009) and the processes driving corrosion were rarely addressed (Matsumoto, 1990). Porosity in the large, well-exposed seep-carbonates on Hydrate Ridge equals or even exceeds the amount of porosity in the seep-carbonates at the Amsterdam and Athina MV (pers. obs. Gerhard Bohrmann), but this attribute of the Hydrate Ridge carbonates received very little attention. Abundant pores were mentioned by Teichert et al. (2005), but their origin, being either primary or secondary, was not discussed. Here, new mineralogical, petrographic, and geochemical data on seep-carbonates from the Amsterdam and Athina MV are presented. Evidence of widespread carbonate corrosion is documented and possible mechanisms of carbonate destruction are suggested.

2. Samples and analytical methods

Samples were retrieved with the manipulator arm of the ROV MARUM-QUEST4000 during R/V METEOR cruise M70/3 in 2006 (Table 1). The samples were cut into slabs and polished for scanning and thin section preparation. Thin sections (100 x 75 and 150 x 100 mm) were stained with a mixture of potassium ferricyanide and alizarin red dissolved in 0.1% HCl (Dickson, 1966) and Feigl's solution (Feigl and Anger, 1958). Powder X-ray diffraction (XRD) measurements on micro-drilled samples were performed on a Philips X'Pert Pro MD X-ray diffractometer (Cu-K α tube; $\lambda=1.541$; 45 kV, 40 mA) by the Crystallography research group, University of Bremen. Samples for carbon and oxygen stable isotope analysis were taken from polished slabs with a micro-drill. Sample powders were reacted with 100% phosphoric acid at 75 °C and the produced CO₂ was analysed with a Finigan MAT 251 mass spectrometer at the MARUM, University of Bremen. The $\delta^{13}\text{C}$ and $\delta^{18}\text{O}$ values were calibrated against NBS19 and are reported in per mill (‰) relative to the Vienna-PeeDee Belemnite standard (standard deviation <0.07‰).

Table 1: Analysed seep-carbonate samples and sampling sites (GeoB = Geoscience Department, Bremen).

GeoB Sample	Location	Latitude [N]	Longitude [E]	Water depth [m]
11301-5	Amsterdam mud volcano	35°19.618'	30°15.358'	2026
11301-6	Amsterdam mud volcano	35°19.516'	30°15.172'	2016
11308-1	Amsterdam mud volcano	35°20.181'	30°14.848'	2034
11319-2	Athina mud volcano	35°23.262'	30°12.611'	1765

3. Results and discussion

3.1 Sub-seafloor genesis of carbonates

The carbonate crusts exposed at the Amsterdam and Athina MV comprise two main lithofacies: i) sediment cemented by microcrystalline carbonate, and ii) pore-filling clotted and botryoidal cement (Fig. 3). Powder X-ray-diffractometry and petrographic analysis revealed that the authigenic carbonate phases consist of aragonite. Apart from aragonite, the carbonate cemented sediment contains minor amounts of calcite, magnesian calcite, quartz, and clay minerals. Angular mud-breccia clasts and bioclasts (bivalves, foraminifers, gastropods, and pteropods) are typical features of the carbonates. The degree of lithification varies from unconsolidated to well indurated sediment, indicating variable spatial distribution of the cementation front. Samples that predominantly consist of clotted and botryoidal cement contain only traces of calcite and magnesian calcite, suggesting that bioclasts are the only source of calcite.

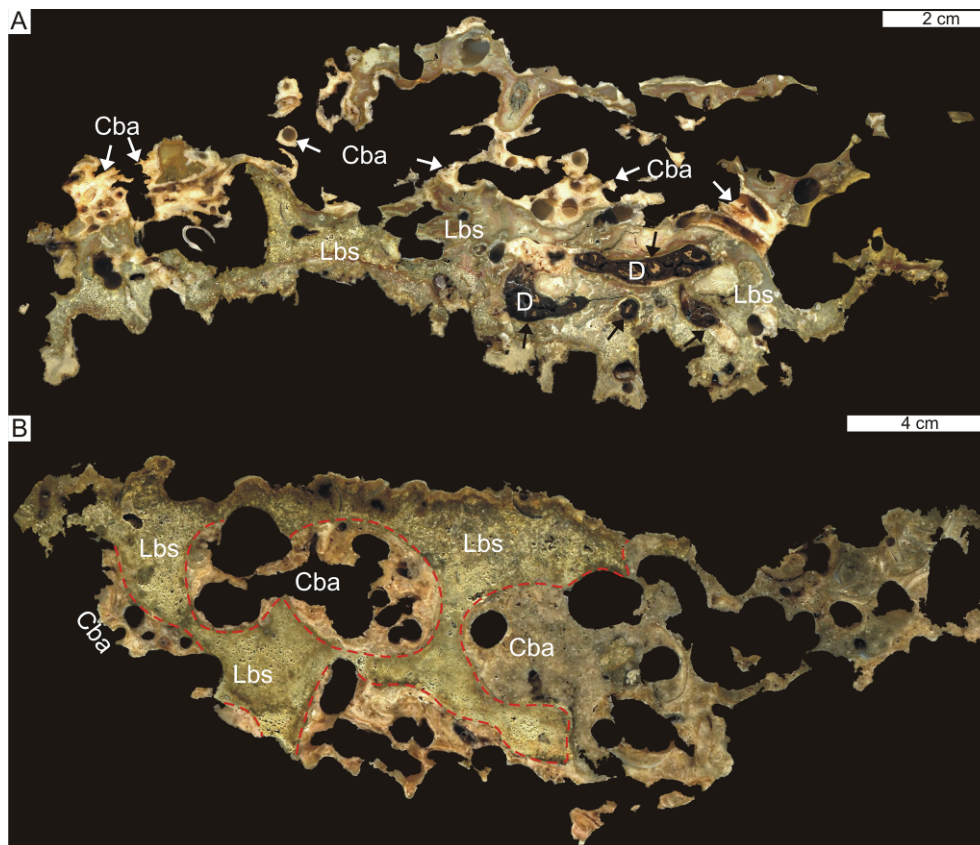


Fig. 3: Scanned cross-section through seep-carbonates with secondary porosity (A = GeoB 11308-1; B = GeoB 11319-2); Cba = clotted and botryoidal aragonite; Lbs = lithified background sediment. D = detrital sediment. (A) Burrows within lithified background sediment (black arrows); open pores are filled with detrital sediment and clotted and botryoidal aragonite; white arrows indicate channels cross cutting clotted and botryoidal aragonite.

Geochemical conditions favouring aragonite precipitation (i.e., high Mg/Ca ratios, high sulphate, and low phosphate concentrations; cf. Burton, 1993) are likely to occur within anoxic mud-flows where methane-rich pore waters intermix with sulphate-rich bottom waters. AOM leads to high pore-water carbonate alkalinity and eventually to carbonate precipitation at the base of the sulphate-reduction zone. Based on lipid biomarkers diagnostic for the prokaryotes performing AOM and steep pore-water sulphate gradients, Aloisi et al. (2002) argued that high sulphate concentration exerts the main control on carbonate precipitation, resulting in the predominance of aragonite. Our stable carbon and oxygen isotope data agree with AOM-induced carbonate precipitation within the shallow sub-seafloor (Fig. 4). Microcrystalline aragonite yielded $\delta^{13}\text{C}$ values between -24.9 and -12.0‰ ($-20.6 \pm 3.0\text{‰}$; $n = 9$) and $\delta^{18}\text{O}$

values between 2.5 and 3.9‰ (3.0 ± 0.4 ‰). The $\delta^{13}\text{C}$ values of clotted and botryoidal aragonite are slightly lower, ranging from -32.8 to -19.1 ‰ (average: -26.1 ± 4.3 ‰; $n = 9$), but this phase yielded similar $\delta^{18}\text{O}$ values between 2.6 and 3.4‰ (2.9 ± 0.3 ‰). The measured $\delta^{18}\text{O}$ values cluster around the expected $\delta^{18}\text{O}_{\text{aragonite}}$ value of 3.3‰ calculated after Grossman and Ku (1986) for aragonite precipitation in equilibrium with ambient conditions (bottom water temperature $T = 13^\circ\text{C}$; $\delta^{18}\text{O}_{\text{seawater}} = 1.5$ ‰ SMOW; cf. Aloisi et al., 2000), agreeing with carbonate precipitation close to the seafloor. This interpretation is in accord with pore-water sulphate profiles that confine the actual zone of AOM at the Amsterdam MV within 70 to 30 cm below the seafloor (Pape et al., 2010).

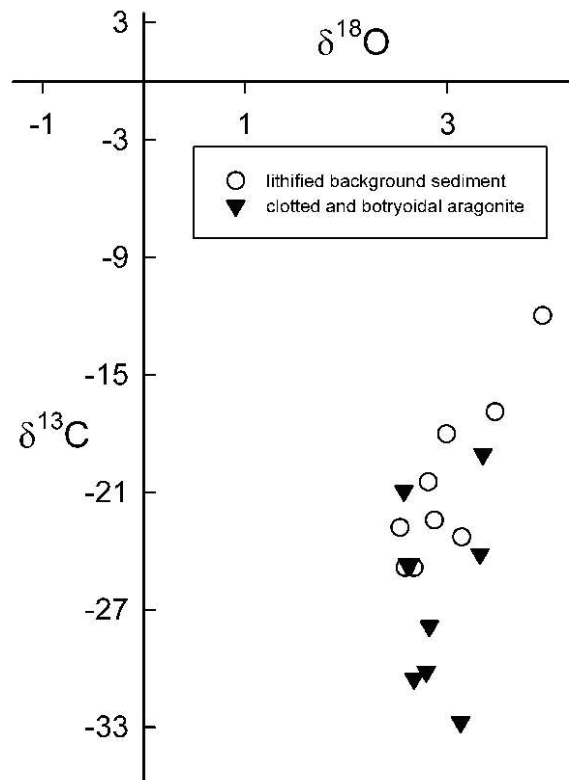


Fig. 4: Carbon and oxygen stable isotope plot of the two main lithofacies of carbonate crusts at Amsterdam and Athina mud volcanoes.

Seep-carbonates usually reveal $\delta^{13}\text{C}$ values that reflect the dominant carbon species of the early diagenetic carbon pool (e.g., Formolo et al., 2004; Naehr et al., 2007). Dissolved inorganic carbon (DIC) at seeps derives from the oxidation of

^{13}C -depleted methane (microbial methane: -110 to -50‰ ; thermogenic methane: -50 to -20‰ ; Whiticar, 1999), crude oil (-35 to -25‰ ; Roberts and Aharon, 1994), and possibly minor organic matter (approximately -25‰ or higher) with variable contributions of seawater DIC (approximately 0‰) and residual CO_2 from methanogenesis ($+15\text{‰}$ or higher; cf. Irwin et al., 1977). The negative $\delta^{13}\text{C}$ values of the early lithified sediment ($-20.6 \pm 3.8\text{‰}$) are best explained by the prevalence of bicarbonate derived from AOM and an admixture of seawater DIC. The lowest $\delta^{13}\text{C}$ values (as low as -32.8‰) for clotted and botryoidal aragonite agree with methane as dominant carbon source.

3.2 Implications on carbonate corrosion

The irregular surfaces of the carbonate crust exposed at the Amsterdam and Athina MV reflect to some degree the spatial distribution of cementation within the sediment. However, the most striking textural features of seep-carbonates are superabundant cavities and corrosion surfaces (Figs. 5, 6). The heavily corroded internal and external surfaces (Fig. 6) demonstrate that widespread dissolution of carbonate shaped the crusts. Corrosive dissolution affected all carbonate phases and components including aragonite cemented sediment, clotted and botryoidal aragonite cements, and bioclasts (Fig. 6). Based on the analysis of 19 large thin sections at least 10 vol. % of the seep-carbonate was dissolved (cf. Flügel, 2004). This approach is probably even underestimating the total amount of dissolved carbonate. Although it is straightforward to assess the internal porosity in this way, it is more difficult to constrain the degree of dissolution on external surfaces.

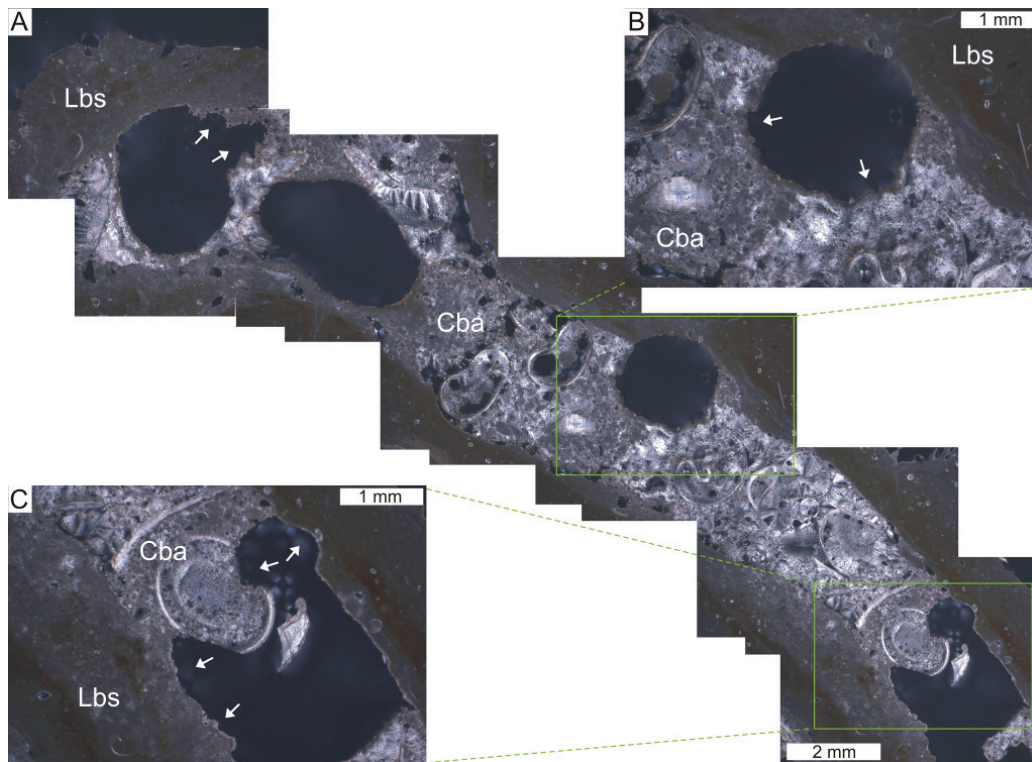


Fig. 5: Different types of secondary pore space; white arrows point to corrosion surfaces; Cba = clotted and botryoidal aragonite; Lbs = lithified background sediment. (A) Photo-mosaic showing a firmground burrow within early lithified sediment filled with clotted and botryoidal aragonite (crossed nicols; open pores appear dark) and mollusc shells. (B) A later boring crosscutting early lithified background sediment and clotted and botryoidal aragonite. (C) Highly irregular corrosion surfaces.

The carbonate minerals aragonite and calcite dissolve in solutions undersaturated with respect to carbonate ions at given pressure and temperature, with aragonite being more prone to dissolution due to its higher solubility constant (Morse et al., 1980). Recent deep water in the eastern Mediterranean Sea is supersaturated with respect to aragonite (cf. Millero et al., 1979). Thus, an additional mechanism is required that locally induces carbonate dissolution at the Amsterdam and Athina MV to explain the observed corrosion patterns. A possible scenario involves the oxidation of methane and hydrogen-sulphide. Today, AOM occurs between 30 to 70 cm below the sediment-water interface in the central part of the Amsterdam MV (e.g., Pancost et al., 2000; Pape et al., 2010), while large amounts of methane pass through the zone of AOM and escape

periodically into the water column (cf. Charlou et al., 2003). Similarly, diffusion of hydrogen-sulphide into the bottom waters at the Amsterdam MV has been documented by pore water profiles (Pape et al., 2010).

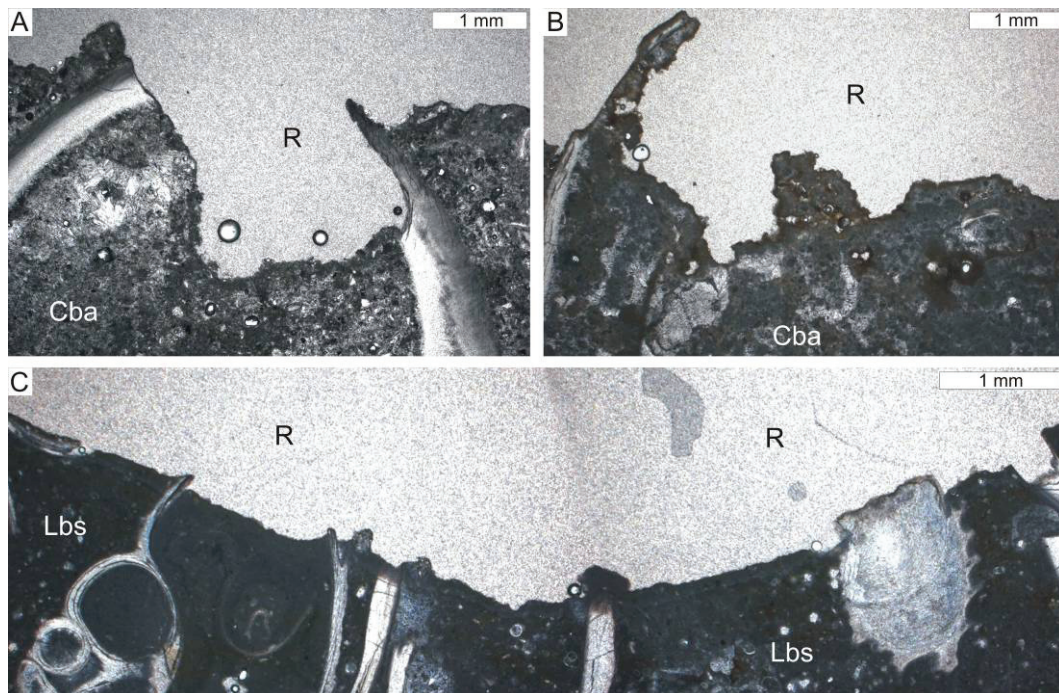
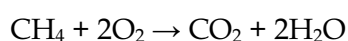


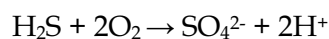
Fig. 6: Patterns of carbonate corrosion; plane-polarized light; Cba = clotted and botryoidal aragonite; Lbs = lithified background sediment; R = resin. (A) Corroded shell fragment and clotted and botryoidal aragonite. (B) Highly irregular corrosion surface on clotted and botryoidal aragonite cement. (C) Relatively smooth corrosion surface on early lithified sediment with abundant mollusc shell fragments.

Like at other seeps, the Amsterdam and Athina MV seep-carbonates formed under anoxic conditions (Aloisi et al., 2002). In order to explain the extensive corrosion patterns observed, we utilise the scenario put forward by Matsumoto (1990): Erosion of the background sediment through bottom water currents eventually exposed the seep-carbonates to oxic bottom waters. When the seepage fluids charged with methane and hydrogen-sulphide passed by the now exposed crusts, the reduced compounds were oxidized. As a consequence of this oxidation, the pH value locally dropped. When methane is oxidized in an aerobic process, a weak acid is produced that should favour carbonate dissolution rather than precipitation (Matsumoto, 1990; Paull et al., 1992).



It needs to be mentioned that the supposed effect of aerobic oxidation of methane on carbonate minerals is yet to be verified, because it is difficult to exclude that other processes at seeps may counteract this effect. If an associated process would increase the pH value, the transformation of the produced carbon dioxide to carbonate ions may occur, favouring precipitation instead of dissolution. For the time being, it remains difficult to explain the signatures of oxic conditions and aerobic methanotrophy found in some seep-carbonates (i.e. negative Ce-anomalies and molecular fossils of aerobic methanotrophs; e.g., Birgel and Peckmann, 2008; Feng et al., 2009; Himmler et al., 2010). The effect of aerobic oxidation of methane on the pH value of pore fluids can be possibly counteracted by other processes, but such counteracting processes seem not feasible in the oxic water column or on the surface of exposed carbonates. It can, thus, be asserted that the observed carbonate corrosion was possibly caused by bacterial methane oxidation under oxic conditions.

Sulphide-oxidation is another process shaping methane-seep environments that has the potential to increase acidity and to dissolve carbonate minerals. Many seeps including those of the Amsterdam and Athina MV are typified by sulphide-oxidizing bacteria like *Beggiatoa* or *Thioploca* that oxidize hydrogen-sulphide with oxygen or nitrate (Schulz and Jørgensen, 2001; Joye et al., 2004).



This process locally lowers the pH values of pore fluids or bottom waters, favouring dissolution of seep-carbonates. Based on high resolution pore-water measurements (pH, pCO₂, DIC, alkalinity) in hydrocarbon-seep sediments, Cai et al. (2006) detected a narrow zone of carbonate undersaturation immediately below the sediment-water interface where calcareous clam shells are corroded. These authors suggested that aerobic oxidation of methane combined with sulphide-oxidation is responsible for an increase in pCO₂ and a decrease of pH, leading to local carbonate dissolution. Evidence for the occurrence of aerobic methanotrophy stems from biomarkers of aerobic methanotrophs detected in

modern (Elvert and Niemann, 2008) and ancient seep-deposits (Birgel and Peckmann, 2008), confirming that aerobic oxidation of methane episodically prevails in these environments.

Notably, the studied seep-carbonates are devoid of authigenic pyrite (cf. Aloisi et al., 2000). This observation indicates that hydrogen-sulphide produced by AOM was not fixed by ferrous iron in the pore water, which would have led to subsequent pyrite formation (Schoonen, 2004). Together with the presence of hydrogen-sulphide in the seep fluids today, this observation reveals that sulphide-oxidation may well have contributed to the generation of acidity. The lack of pyrite and iron oxyhydroxides also renders unlikely the possibility that corrosion resulted from pyrite oxidation (cf. Pirlet et al., 2010).

4. Conclusions

Seep-carbonates consisting of ^{13}C -depleted aragonite exposed at the Amsterdam and Athina mud volcanoes in the eastern Mediterranean Sea formed in the shallow anoxic subsurface, induced by AOM. Erosion of the surrounding background sediment exposed the carbonates to oxic bottom waters. A striking feature of the carbonates is their secondary porosity, most of which resulted from corrosion. Based on today's release of methane and hydrogen-sulphide into the bottom water at the study sites, we suggest that aerobic oxidation of methane and hydrogen-sulphide locally generated acidity, which caused corrosion of aragonitic seep-carbonates in the otherwise oversaturated bottom waters. A crude estimate deduced from thin sections indicates that at least 10 vol.% of the studied seep-carbonate was dissolved. In order to properly assess the significance of dissolution for mass-balance considerations on carbon flux, similar assessments should be made on other modern seep-carbonates worldwide. A comparison of modern seep-carbonates exposed to oxic seawater based on a literature survey and own seafloor observations indicates that a great amount of carbon is liberated by carbonate-corrosion, resulting in a substantial, deferred flux of methane-derived carbon to the ocean. Corrosion of seep-

carbonates on and above the seafloor was apparently often overlooked or ignored in the past.

Acknowledgements

We appreciate the skilful work of the captain, the crew, and the MARUM-QUEST4000 team during R/V METEOR cruise M70/3. Monika Segl and Christoph Vogt are acknowledged for analytical support. We thank Gerald Dickens and an anonymous referee for constructive comments, which considerably improved the manuscript. Funding was provided through the DFG-Research Center/Excellence Cluster “The Ocean in the Earth Systems”.

2.3 Manuscript 3

Rare earth element signatures of early diagenesis in cold-seep pore waters on Hydrate Ridge, off Oregon

Tobias Himmeler¹, Brian Haley², Marta Torres², Gary Klinkhammer², Gerhard Bohrmann¹, Jörn Peckmann³

¹ *MARUM–Center for Marine and Environmental Sciences and Department of Geosciences, University of Bremen, 28334 Bremen, Germany*

² *College of Oceanic and Atmospheric Sciences, Oregon State University, Corvallis OR 97331, USA*

³ *Department of Geodynamics and Sedimentology, Center for Earth Sciences, University of Vienna, 1090 Vienna, Austria*

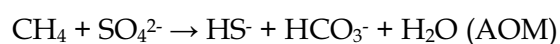
Submitted March 2011 to *Geochemistry, Geophysics, Geosystems*.

Abstract

We have studied the distribution of rare earth elements (REE) and major geochemical parameters (i.e., sulfate, sulfide, total alkalinity, calcium, magnesium and phosphate) in cold-seep pore waters from two push cores taken on Hydrate Ridge (northeast Pacific Ocean, off Oregon coast). Downcore decreasing sulfate and coevally increasing sulfide concentrations indicate bacterial sulfate reduction as dominant early diagenetic process. Pore water total REE (Σ REE) concentrations increase markedly immediately below the sediment-water interface and are much higher compared to Σ REE in overlying water. Distinct convex-shaped shale-normalized REE patterns with relative cerium (Ce) enrichment are observed at ~2-cm-depth below the sediment water interface, probably related to intensive microbial activity and reduction of particulate Ce-oxides within shallow sediments. Below ~2-cm-depth, shale-normalized REE patterns display linear heavy REE-enrichment and negative cerium Ce anomalies. These features are ascribed to REE-carbonate complexation due to increased carbonate alkalinity. Decreasing Σ REE concentrations correlate with decreasing calcium concentrations, which is interpreted to represent REE-scavenging during precipitation of cold-seep carbonates.

1. Introduction

Pore fluids enriched in microbial and thermogenic methane are expelled from sediments on the convergent Cascadia margin, off Oregon, USA (e.g., Kulm et al., 1986; Torres et al., 2009). On Hydrate Ridge, a prominent gas hydrate bearing accretionary ridge, large amounts of dissolved methane are consumed within sediments by microbially mediated anaerobic oxidation of methane coupled to sulfate-reduction (AOM) (Boetius et al., 2000; Knittel, et al., 2003; Treude et al., 2003; Valentine et al., 2005):



AOM-produced hydrogen sulfide is transported via advecting pore fluids of various flux intensities to the seafloor where it sustains extensive bacterial mats of sulfide-oxidizing bacteria at higher flux rates and clusters of vesicomylid clams at lower flux rates (Sahling et al., 2002; Torres et al., 2002). Very high rates of sulfate-reduction (up to $140 \text{ mmol m}^{-2} \text{ d}^{-1}$) (cf. Boetius et al., 2000) coupled to AOM lead to increased carbonate alkalinity, resulting in the precipitation of seep-carbonates within the sediments (e.g., Ritger et al., 1987; Luff and Wallmann, 2003; Leefmann et al., 2008). Recently, rare earth element (REE) studies of modern and ancient authigenic cold-seep carbonates were used to reconstruct variable redox-conditions at cold-seeps (e.g., Feng et al., 2008; 2009), and REE were suggested as tracers for different fluid sources preserved during cold-seep carbonate precipitation (Himmeler et al., 2010). These studies were restricted by the current lack of knowledge on the distribution of REE in cold-seep pore waters, as no data have been reported on the distribution of REE in cold-seep associated pore waters.

To obtain cold-seep pore waters is not an easy task: Cold-seeps are spatially confined areas on the seafloor where the geochemical environment changes from “cold-seep” to “normal marine” within meters and cementation of the sediment by seep-carbonates may prevent penetration of sampling tools. On Hydrate Ridge, cold-seeps are characterized by chemosynthesis-based faunal assemblages on the seafloor (Sahling et al., 2002). Therefore visually-controlled sampling devices are needed to target veritable sampling-sites (video guided multiple corers, push cores deployed with remotely operated vehicles or manned submersibles). Moreover, measuring REE in pore waters is fraught with complications, because: (i) the sample volume is not greater than a few milliliters and the concentration of REE is extremely low (pico-molar level); (ii) in order to avoid signal suppression and isobaric interferences of certain REE-isotopes with oxides during analysis, REE must be separated from dissolved salts. To overcome these analytical limitations a tailored instrumental setup is required that allows to separate and measure REE in pore waters (Haley and Klinkhammer, 2003).

In this study we report for the first time REE data from cold-seep pore waters. We examine the behavior of REE in a combined study together with major chemical pore water parameters (i.e., sulfate, sulfide, total alkalinity, calcium, magnesium and phosphate), and discuss early diagenetic geochemical processes based on REE-profiles and shale-normalized REE patterns.

2. Sampling and analytical procedures

Samples were retrieved with ALVIN submersible from two locations on Hydrate Ridge during R/V Atlantis cruise AT3-35B in 1999 (HRN = northern area; HRS = southern part; Table 1; Fig. 1). Push cores were taken from cold-seep sediments as indicated by the chemosynthetic communities on the seafloor (cf. Torres et al., 2002).

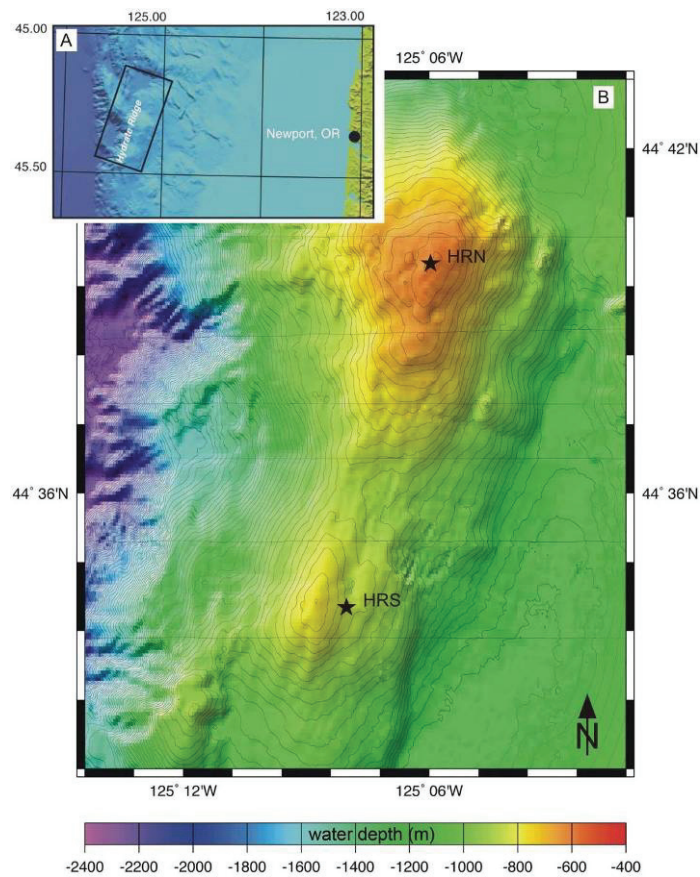


Fig. 1: (A) Location of Hydrate Ridge, off Oregon. (B) Sampling sites at Hydrate Ridge North (HRN) and Hydrate Ridge South (HRS).

Table 1: Locations and seafloor features of sampling sites on Hydrate Ridge; HRN = Hydrate Ridge North; HRS = Hydrate Ridge South.

Station	Latitude	Longitude	Water depth (m)	Remarks
HRN	44°40.03'N	125°06.01'W	600	Extensive authigenic seep-carbonates
HRS	44°34.20'N	125°08.82'W	768	Soft sediment covered with extensive mats of filamentous sulfur-oxidizing bacteria

Pore waters were extracted on board from sediment slices by centrifugation and processed under nitrogen atmosphere and in situ temperatures. Push-core sampling allows analyses of seawater that directly overlies the sediment surface, here referred to as overlying water. Extracted pore waters were filtered (0.45 μm) into HCl-cleaned bottles and subsequently acidified with triple-distilled 6N HCl. Aliquots were stored at 4°C for trace element analysis. Total alkalinity and phosphate were determined using standard analytical procedures (e.g., Grasshoff et al., 1999). Calcium and magnesium concentrations were analyzed using atomic emission spectroscopy; sulfate was analyzed by ion chromatography. Pore water aliquots for sulfide (H_2S) determination were initially fixed on-board by adding Zn-Acetate solution and sulfide content was determined photometrical.

REE analysis was performed in June 2010 using a custom modified Dionex DX-500 ion chromatograph (IC) connected to a PQ ExCell quadropole inductively coupled plasma mass spectrometer (ICP-MS). Custom modifications and detailed analytical procedures are described by Haley and Klinkhammer (2003). In brief, we have used left-over pore water aliquots that were previously used for major element-analysis and on-board measurements. The sample volumes varied between 1 to 6 ml. The remaining aliquots were weighed, filled-up with triple-distilled HNO_3 to a final volume ($\text{volume}_{\text{final}}$) of 7 ml and subsequently injected into the IC with acid-cleaned 10 ml plastic syringes. Dilution is necessary to confidently fill the 5-ml-sample-loop of the IC-module. We calculated the dilution factor (DF) as weight ratio ($\text{volume}_{\text{final}}$ /remaining aliquot). Pore water REEs are separated from the matrix and concentrated via

several chromatography columns before being released individually to the connected ICP-MS for real-time analyses. Contamination from the IC was monitored through replicate analyses of a seawater sample (NBP95 R10) (see Haley and Klinkhammer, 2003). Indeed, due to dysprosium contamination in one of the IC-reagents concentrations of this element are excluded from this study. REE concentrations were normalized against PAAS-values (Nance and Taylor, 1976). Subscript 'SN' denotes shale-normalized values. We calculated the cerium (Ce) anomaly as $Ce/Ce^* = (2Ce_{SN}/La_{SN}+Pr_{SN})$ (de Baar et al., 1983), and as $Ce/Ce^* = (Ce_{SN}/2Pr_{SN}-Nd_{SN})$ (Bolhar et al., 2004). Other elemental anomalies including lanthanum (La) and europium (Eu) were calculated as follows (cf. Bolhar et al., 2004; Bau and Dulski, 1996): $La/La^* = La_{SN}/(3Pr_{SN}-2Nd_{SN})$; $Eu/Eu^* = Eu_{SN}/(0.67Sm_{SN}+0.33Tb_{SN})$. REE_{SN}/REE_{SN}^* ratios higher than 1 indicate a positive anomaly and ratios smaller than 1 indicate a negative anomaly. We only consider REE_{SN}/REE_{SN}^* anomalies below 0.8 and above 1.2 as significant due to the analytical uncertainties (1 σ standard deviation of the method is ~ 17%) (Haley and Klinkhammer, 2003).

3. Results

Downcore total REE (Σ REE) concentrations together with non-REE parameters are shown in Figure 2. REE profiles are presented in Figure 3 for light REE (LREE; i.e. average of La, Pr, and Nd), the elements Ce and Eu, as well as the heavy REE (HREE; i.e. average of Er, Tm, Yb, and Ly). Cerium and Eu are shown separately because these elements may react different from their REE neighbors due to the unique redox-chemistry of Ce and Eu (de Baar, et al., 1988; Brookins, 1989; Bau et al., 2010). The shale-normalized patterns are shown in Figure 4.

Table 2: Non-REE parameters at station HRN; OW = overlying water; TA = total alkalinity.

Station HRN						
Depth (cm)	TA (mM)	SO ₄ ²⁻ (mM)	H ₂ S (mM)	Ca ²⁺ (mM)	Mg ²⁺ (mM)	PO ₄ ³⁻ (μM)
OW	2.35	26.3	0.04	12.9	53.0	2.32
-0.75	2.87	26.2	0.04	13.2	53.6	7.61
-2.26	6.33	25.0	0.99	12.3	53.5	11.6
-3.77	10.9	19.9	2.69	11.2	52.6	7.65
-5.27	13.5	18.1	3.52	10.6	52.8	5.7
-6.78	17.1	15.1	4.59	8.61	52.2	5.84
-8.28	23.5	7.46	3.79	7.48	51.9	8.5

Table 3: Non-REE parameters at station HRS; OW = overlying water; TA = total alkalinity.

Station HRS						
Depth (cm)	TA (mM)	SO ₄ ²⁻ (mM)	H ₂ S (mM)	Ca ²⁺ (mM)	Mg ²⁺ (mM)	PO ₄ ³⁻ (μM)
OW	2.14	23.6	0.06	11.5	47.3	0.17
-0.71	4.68	21.9	0.52	13.1	52.1	18.9
-2.12	6.81	18.4	1.80	12.4	51.6	16
-3.53	11.6	14.9	4.07	11.4	52.2	13
-4.94	16.5	8.51	7.28	9.9	53.3	11.3
-6.35	2.34	3.69	10.7	7.90	52.3	12.3
-7.76	30.2	2.73	12.8	3.92	51.8	15.5
-9.17	30.2	1.77	13.3	2.80	51.8	15.1
-10.59	33.1	1.75	16.4	2.58	51.5	18.4

3.1 Comparison of REE- and non-REE profiles

Overlying water yield the lowest Σ REE concentrations (55 and 73 pmol kg⁻¹; for HRS and HRN, respectively) whereas pore water is 2 to 36 times REE-enriched over overlying water (Tables 4 and 5). HRN pore waters yield slightly lower Σ REE values than HRS samples (HRN = 230 to 1327 pmol kg⁻¹; HRS = 135 to 2018 pmol kg⁻¹). The peak- Σ REE concentrations for both sites are found at ~2-cm-depth. Below this depth, Σ REE decrease gradually but never reach concentrations lower than overlying waters. In the interval between ~2 and ~5-cm-depth Σ REE concentrations from HRS are slightly higher compared to HRN samples. Despite these minor variations the shapes of the downcore Σ REE profiles are similar for both stations (Fig. 2).

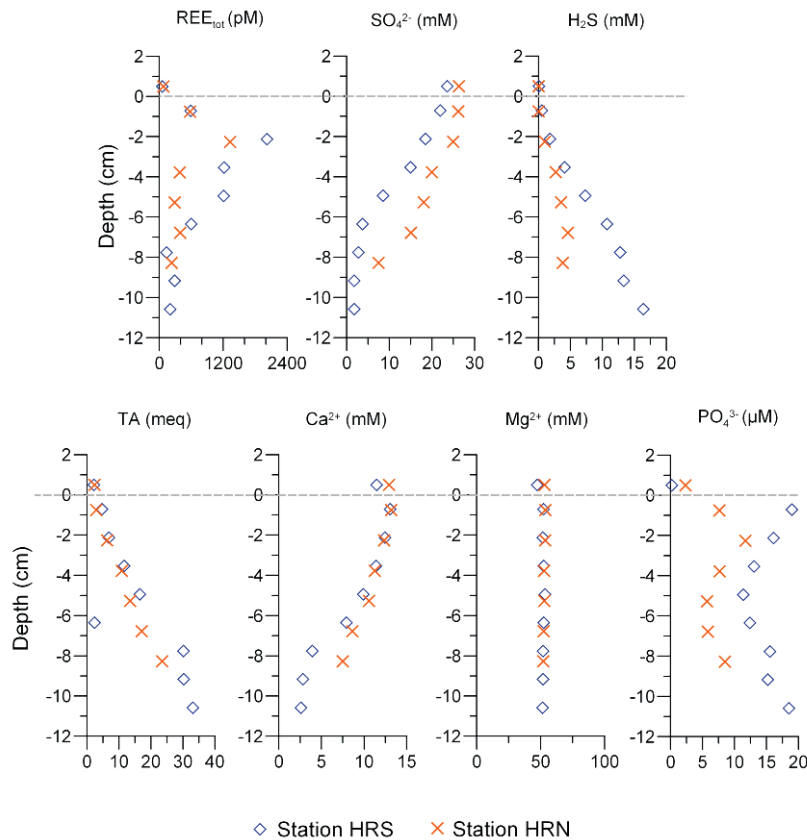


Fig. 2: Pore water parameters of the investigated Hydrate Ridge stations at the northern summit (HRN) and southern mound (HRS). Vertical grey line indicates the sediment–water interface; TA = total alkalinity.

At both sites the sulfate concentrations in overlying waters are sea water-like (~28 mM). Overall, the two stations are characterized by downcore-decreasing sulfate concentrations and coeval increasing sulfide and total alkalinity. The HRS Σ REE profile follows this trend in that the highest Σ REE concentrations occur in the reactive layer of sulfate-reduction (i.e. steep gradient between sulfate maximum and minimum). The relatively lower Σ REE concentrations in HRN samples go together with slightly higher sulfate and lower sulfide concentrations – a first hint that REE distribution in cold-seeps is related to sulfate reduction. At the HRS site dissolved Ca^{2+} decreases gradually downcore, with a steep gradient at ~7-cm-depth. This trend is also evident for Σ REE below ~2-cm-depth, suggesting that consumption of dissolved Ca^{2+} and REE is coupled to the same process. In the HRN samples this particular observation is less clear; however the same general trend (i.e. decreases of both,

Ca²⁺ and Σ REE) is evident. In contrast to Ca²⁺, downcore Mg²⁺ is constant and shows no correlation with Σ REE. Phosphate correlates with the REE-trend only in the uppermost sample at ~1-cm-depth. The downcore PO₄³⁻-profile is apparently decoupled from Σ REE (i.e. downward-increasing PO₄³⁻ and decreasing Σ REE).

Table 4: Pore water REE concentrations at station HRN; DF = dilution factor (see text for explanation); bd = below detection; nc = not calculated; HREE/LREE = average of PAAS-normalized values of Er, Tm, Yb and Lu over La, Ce, Pr and Nd.

Station HRN							
Depth (cm)	OW	-0.75	-2.26	-3.77	-5.27	-6.78	-8.28
DF		1.45	1.8	2.28	2.68	3.74	3.27
REE(pmol/kg)							
La	43.2	116.6	171.4	98.6	99.1	161.2	114.9
Ce	bd	235.6	615.6	159.5	90.7	96.4	57.3
Pr	bd	37.2	69.7	18.2	9.1	22.2	6.1
Nd	11.5	93.3	251.2	44.7	46.2	26.6	25.3
Sm	5.1	24.8	59.7	21.4	8.6	15.8	8.3
Eu	2.3	6.6	14.1	3.8	3.3	8.5	2.8
Gd	3.4	20.8	47.7	12.9	14.5	14.8	5.8
Tb	0.9	4	8.2	2.8	4.6	8.4	2.7
Ho	2	5.9	11.2	4.8	bd	5.2	bd
Er	1.2	13	29.9	7	2.6	7.2	2
Tm	0.5	2.1	5.2	1.6	bd	4.8	bd
Yb	2.7	14.3	36.6	7	4	12.1	2.5
Lu	0.7	2.6	6.6	1.7	1.7	7.2	2.5
Σ REE	73.4	576.8	1327	384	284.4	390.5	230.3
La/La* (Bolhar et al., 2004)	nc	0.5	0.6	0.8	21.1	0.7	7.1
Ce/Ce* (Bolhar et al., 2004)	nc	0.5	1	0.7	2	0.3	1.3
Eu/Eu* (Bolhar et al., 2004)	2	1.2	1.1	0.9	0.9	1.3	1.1
Ce/Ce* (de Baar et al., 1983)	nc	0.8	1.2	0.9	0.6	0.4	0.4
HREE/LREE	1.7	1.9	2.3	1.9	1.7	5	2.3

Table 5: Pore water REE concentrations at station HRS; DF = dilution factor (see text for explanation), bd = below detection; nc = not calculated; HREE/LREE = average of PAAS-normalized values of Er, Tm, Yb and Lu over La, Ce, Pr and Nd.

Station HRS									
Depth (cm)	OW	-0.71	-2.12	-3.53	-4.94	-6.35	-7.76	-9.17	-10.59
DF		2.73	1.08	4.13	3.12	1.25	2.8	2.56	2.65
REE (pmol/kg)									
La	35.7	120.1	207.3	245.3	268.8	83.2	65.8	95.5	82.2
Ce	bd	192.9	928	396.8	501.9	231.9	bd	85.6	50.7
Pr	1.6	30.9	101.1	52.9	68.3	35.4	4	14.7	8.5
Nd	6.4	87.4	386.4	268.5	203.2	146.9	19.5	43	22
Sm	2.7	35.7	109.5	49.4	42.6	38.2	15.3	10.5	11.8
Eu	bd	5.8	26.7	12.3	8.9	7.1	1.3	1.1	2
Gd	1.1	36.1	104.6	57	39	29.3	13.4	12.1	11.1
Tb	0.6	5.4	16.2	9.5	5.9	3.9	1.2	1.7	2.1
Ho	0.8	9.7	19.7	15.4	10.3	3.3	0.7	1.7	2
Er	3.3	30.5	48.5	52.3	28	9.2	7.3	11	3.5
Tm	0.1	4.5	8.3	6.4	3.6	1.2	0.5	0.4	1.3
Yb	2.4	24	53.3	42.2	25.5	8.6	4.7	5.7	5.7
Lu	0.5	6	8.5	8.2	2.6	1.5	1.5	1.8	1.7
Σ REE	55.2	589.1	2018.1	1216	1208.6	599.7	135.1	284.7	204.5
La/La* (Bolhar et al., 2004)	6.5	0.6	0.6	10	0.7	0.9	17.6	1.1	1.5
Ce/Ce* (Bolhar et al., 2004)	nc	0.6	1.1	1.5	0.7	0.9	nc	0.6	0.5
Eu/Eu* (Bolhar et al., 2004)	nc	0.8	1.1	1.1	1	1	0.5	0.5	0.7
Ce/Ce* (de Baar et al., 1983)	nc	0.7	1.4	0.8	0.8	0.9	nc	0.5	0.4
HREE/LREE	2.4	4.6	2.3	3.2	1.5	1.1	2.9	2.1	2.9

Downcore profiles of $LREE_{av}$, $HREE_{av}$, Ce, and Eu for both stations are very similar (Fig. 3). This indicates that only minor fractionation occurs across the entire REE series: LREE and HREE are released in similar proportions within the interval between the sediment-water interface and ~2-cm-depth. Below ~2 cm the REE diffuse downward into an unknown sink, again with relatively proportionate LREE:HREE. Cerium and Eu follow these trends without significant deviation from the other REEs.

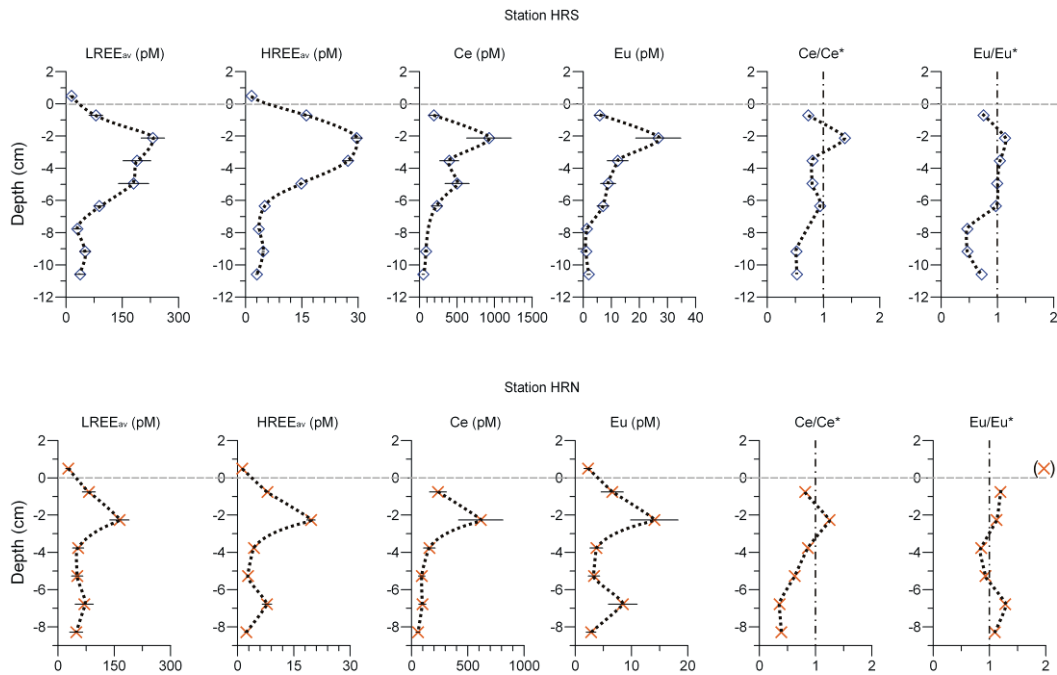


Fig. 3: Pore water REE profiles and plots of downcore Ce and Eu anomalies. Values for Ce anomaly were calculated as $Ce/Ce^* = (2Ce_{SN}/La_{SN} + Pr_{SN})$; the vertical dash-dot lines mark unity values ($1 = \text{no anomaly}$); $LREE_{av}$ = average of La, Pr, and Nd; $HREE_{av}$ = average of Er, Tm, Yb, and Lu; the horizontal error bars indicate individual standard deviation, values are adopted from Haley and Klinkhammer (2003); the grey horizontal line indicates the sediment–water interface; the vertical dotted lines represent our data interpretation and are not calculated best-fit-lines.

3.2 Shale-normalized patterns and REE anomalies

The majority of samples show linear HREE-enrichment ($HREE/LREE > 1$) and slightly negative Ce anomalies when calculated with La (Tables 4 and 5; Figs. 3 and 4). By using this manipulation the determined Ce anomaly is overestimated due to anomalous abundances of La itself (i.e. positive La anomaly). This is only the case for samples at ~5 (~4) and ~8 (~8) cm-depth from HRN (HRS) as revealed by positive La anomalies. Distinct convex-shaped patterns with a small middle REE-bulge (MREE; i.e. Sm, Eu, Gd, Tb) are observed in ~2-cm-depth at both sites, remarkably with positive Ce anomalies (Fig. 3). A positive Eu anomaly is calculated for overlying water at the clam field site (Fig.3), but this is most likely a sampling or analytical artifact. One sample from HRN yields a minor positive Eu anomaly at ~7-cm-depth.

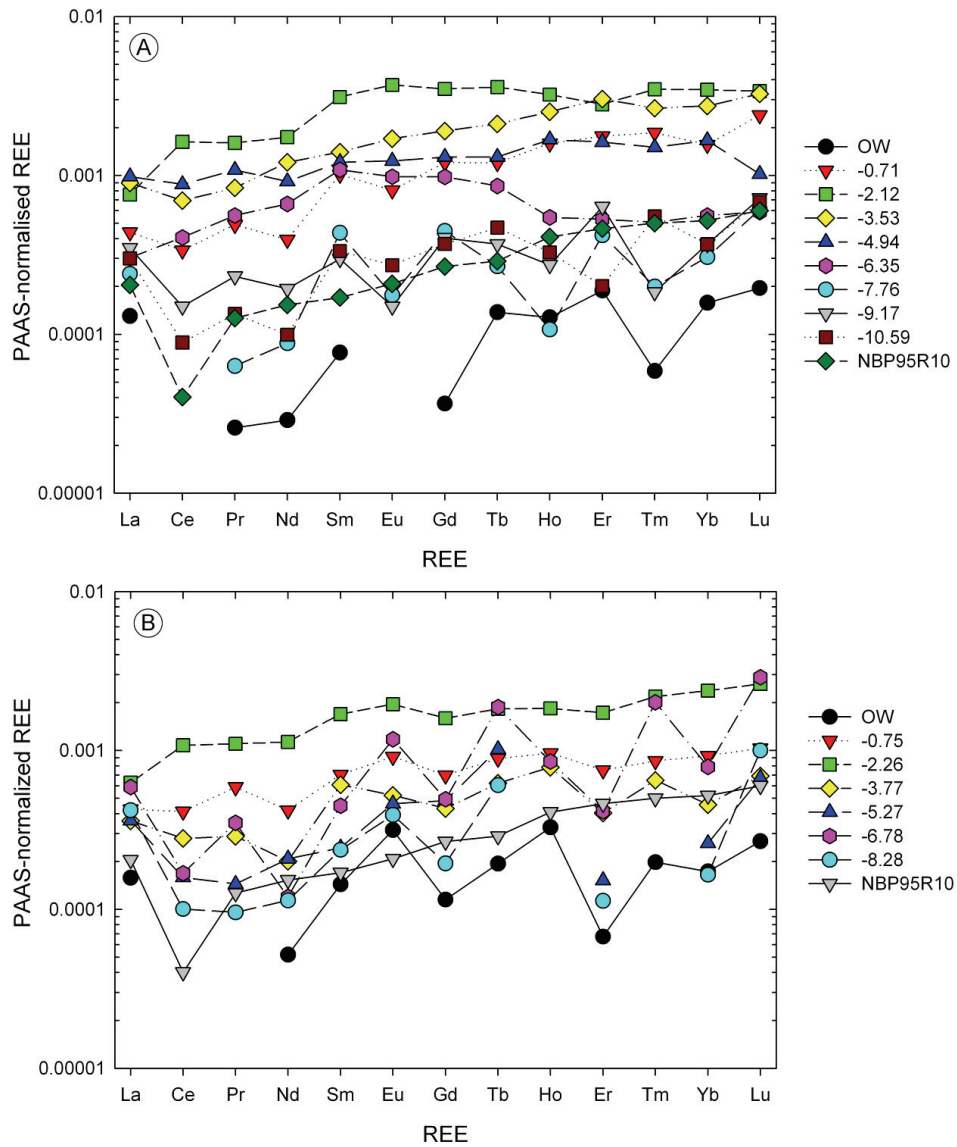


Fig. 4: Shale-normalized REE-patterns of pore waters and seawater standard NBP95 R10 (cf. Haley and Klinkhammer, 2003); (A) HRS samples; note the general HREE-enrichment; the pattern at 2.12-cm-depth shows a slight MREE-bulge and Ce is relatively enriched over its REE-neighbors. (B) HRN samples; similar to (A) a HREE-enriched pattern with a slight enrichment of Ce occurs at 2.26-cm-depth. Please note that the “noisy” saw-tooth patterns are mainly due to low intensities (i.e., low counts-per-second) during ICP-MS analysis, resulting from the necessarily sample dilution.

4 Discussion

The pore waters of the two stations are characterized by nearly identical geochemical signatures: (1) shallow REE-enrichment followed by downward diffusion; (2) downward decreasing sulfate and coeval increase of total alkalinity and sulfide; (3) downward decrease in Ca and constant Mg values. The minor variations in sulfide and sulfate concentrations are related to different fluid fluxes out of the sediment (Sahling et al., 2002; Torres et al., 2002), with slightly higher sulfide fluxes at HRS.

4.1 Early diagenetic REE-dynamics pore waters on Hydrate Ridge

The investigated pore waters are strongly anoxic due to high sulfide-flux out of Hydrate Ridge sediments (Sahling et al., 2002; Torres et al., 2002). The marked increase of Σ REE concentrations immediately below the sediment-water interface clearly indicates release of REE into pore waters from a yet unidentified source. This seems to be a common feature of pore water REE-dynamics in reducing sediments (Elderfield and Sholkovitz, 1987; Sholkovitz and Elderfield, 1988; Haley et al., 2004). In terms of REE patterns, the pore waters are characterized by HREE-enrichment in a linear fashion and, remarkably, yield negative Ce anomalies (except for samples at ~2-cm-depth; see discussion below). Such HREE-enriched patterns are typical of REE released through degradation of organic matter and subsequent re-association of the released REE with dissolved bicarbonate (Haley et al., 2004). Pourret et al. (2008) investigated the competition between dissolved organic compounds (i.e., humic acids) and carbonate ions for REE-complexation in alkaline solution and showed that HREE-enriched patterns with negative Ce anomalies typify carbonate-complexed REE. With regard to the HREE-enriched patterns and negative Ce anomalies observed here, we suggest that REE in Hydrate Ridge pore waters are mainly carbonate-complexed. The observed HREE-enrichment is consistent with bicarbonate production and coeval rise of alkalinity during sulfate-dependent AOM. Moreover, HREE-enrichment agrees with the increasing complexation and

stability constants of carbonato-complexed REE across the REE series (Cantrell and Byrne, 1987; Lee and Byrne, 1993).

There are, however, two distinctly different patterns observed at ~2 and ~6-cm-depth. At ~2-cm-depth the pattern is not strictly linear, yielding a slight MREE-bulge. This pattern corresponds with the highest Σ REE. Haley et al. (2004) suggested that enhanced release of MREE from the reduction of sedimentary Fe-oxides results in significantly high REE concentrations and distinct MREE-enriched patterns in anoxic pore waters, but the lack of dissolved Fe(II)-data for the samples under investigation hampers this conclusion. Alternatively, the slightly MREE-enriched pattern at ~2 cm is similar to REE distributions patterns found between solutions and bacterial biofilms (Takahashi et al., 2007). Boetius et al. (2000) showed that Hydrate Ridge sediments below bacterial mats of sulfide-oxidizing *Beggiatoa* contain high amounts of cell aggregates of the microbial AOM-consortium (i.e., methane-oxidizing archaea and sulfate-reducing bacteria), remarkably, with the peak-cell-abundance at ~2-cm-depth. The high abundance of microbial biomass at this depth corresponds with the highest Σ REE and the MREE-enriched pore waters observed here. We must note here that the observations of Boetius et al. (2000) derive from another push core taken from *Beggiatoa*-covered sediments on southern Hydrate Ridge. Similarly to the proposed “microbial” distribution pattern by Takahashi et al. (2007) the shale-normalized REE patterns observed at ~2-cm-depth might reflect enhanced microbial activity. However, the REE-distribution patterns reported in Takahashi et al. (2007) were derived from waters containing bacteria precipitating Fe-(oxy) hydroxides, a process that differs significantly from AOM. Nevertheless, considering the relatively low Σ REE and very high amount of microbial biomass within the *Beggiatoa*-covered sediments on Hydrate Ridge, we suggest that the slightly MREE-enriched shale-normalized REE pattern at ~2-cm-depth reflects intensive microbial activity (see discussion below). We can not fully exclude reduction of Fe-oxides though, since AOM can also be coupled to Fe-reduction (Beal et al., 2009).

At ~6-cm-depth a HREE-depleted pattern is observed. With regard to the strong affinity of HREE to form carbonato-complexes in solutions, this observation implies either limited availability of dissolved bicarbonate to form REE-complexes, or the preferential removal of carbonato-complexed HREE into authigenic seep-carbonates. Remarkably, the HREE-depletion in deeper pore waters coincides with a sharp decrease of Ca²⁺ between ~6 and 7-cm-depth. Considering that dissolved Ca²⁺ is readily removed from pore waters through precipitation of seep-carbonates, we suggest that the carbonate-complexed HREE are scavenged in the same fashion. This is in good agreement with the extensive formation of aragonite on Hydrate Ridge (e.g., Ritger et al., 1987; Luff and Wallmann, 2003; Teichert et al., 2005). We note that Terakado and Masuda (1988) have pointed out that it is unlikely for the dissolved carbonato-complexed REE to coprecipitate because only the free REE ions should be incorporated into the aragonite crystal lattice. In contrast, Qu et al. (2009) showed in experimental studies that fast rates of aragonite precipitation results in enhanced incorporation of REE into aragonite crystals. Considering that aragonite precipitation is stimulated during AOM (Luff and Wallmann, 2003), we suggest that the correlation between the deep profiles of Ca²⁺ and ΣREE indicates that both are consumed by the precipitation of cold-seep carbonates.

4.2 Implications on the redox-chemistry of Ce and Eu at cold-seeps on Hydrate Ridge

What is striking about the REE patterns at ~2-cm-depth is that the redox-sensitive element Ce is relatively enriched over its REE-neighbors. This agrees well with the anoxic pore water geochemistry and the microbiological observations (e.g., Boetius et al., 2000; Valentine et al., 2005). With regard to the relatively enriched Ce concentrations, reduction of distinct Ce-oxides may release Ce³⁺ into pore water, following the chemical reaction (cf. Elderfield and Sholkovitz, 1987):



The standard free energy yield during reduction of Ce-oxides is close to the value of denitrification (-453 kJ mol^{-1}) (see Jørgensen, 2006 and references cited therein). Considering the similar energy yields of Ce-reduction to other early diagenetic microbial catalyzed chemical reactions, it is feasible that Ce-oxides are reduced coincidentally, which would explain the relatively enriched Ce^{3+} concentrations observed here (i.e., like all the other LREEs). This interpretation would support a “microbial” REE-pattern at $\sim 2\text{-cm}$ -depth. Remarkably, similar MREE-enriched patterns with positive Ce-anomalies were found in early diagenetic cements of seep-carbonates (Feng et al., 2010), indicating that they formed under similar (i.e., anoxic) conditions.

Negative Ce anomalies are developed further downcore – surprisingly in a strictly anoxic environment as revealed by increasing sulfide concentrations downcore. The development of an “apparent” negative Ce anomaly due to anomalous enrichment of La accounts only for two samples (see above); all other samples carry “true” negative Ce anomalies. Pourret et al. (2008) showed that negative Ce anomalies develop in organic-rich alkaline solutions due to carbonate REE-complexation and subsequent scavenging of Ce^{4+} by humic acids. Similar processes produce the observed negative Ce anomalies, since relatively high concentrations of dissolved organic carbon (DOC) are found in cold-seep pore waters on Hydrate Ridge (cf. Valentine et al., 2005). Considering the increased carbonate alkalinity due to AOM and a relatively high concentration of DOC, the negative Ce anomalies in anoxic pore waters observed here can be explained with the concept put forward by Pourret et al. (2008).

No significant Eu anomalies are observed, which is not surprising, because Eu^{3+} enrichment is more common in high- and low-temperature deep-sea hydrothermal fluids (Klinkhammer et al., 1994; Bau et al., 2010), and has not been detected in anoxic seawater (de Baar et al., 1988). The slight positive Eu anomaly observed at $\sim 7\text{-cm}$ -depth from HRN might be real but this seems to be an exception.

5 Conclusions

Anoxic cold-seep pore waters from two stations on Hydrate Ridge reveal similar geochemical signatures and REE profiles. Robust evidence for early diagenetic REE-mobility derives from: (1) distinct shallow Σ REE maxima, (2) dynamic ranges of shale-normalized REE patterns, and (3) the behavior of the redox-sensitive element Ce. We propose a simple model to explain these features: First, sulfate-dependent AOM increases carbonate alkalinity and dissolved REE immediately form carbonato-complexes, as revealed by HREE-enriched shale-normalized patterns with negative Ce anomalies. The anoxic conditions favor Ce^{3+} stability only at ~ 2 cm-depth as evident from real positive Ce anomalies. This is ascribed to enhanced microbial activity (i.e., sulfate-dependent AOM) and may also include microbial (?) reduction of Ce-oxides. Below the 2-cm- Σ REE-maximum, downward decreasing Σ REE correlates with decreasing Ca concentrations, suggesting that formation of cold-seep carbonates (i.e., aragonite) constitutes a significant REE-sink within anoxic cold-seep sediments on Hydrate Ridge.

Finally, we have to stress that the dilution-step during sample preparation decreases the naturally low REE concentrations even more, resulting in lower counts-per-second during ICP-MS analysis and inevitably higher uncertainties. We are aware of these analytical limitations and note that our interpretations are based on the major REE features. The interpretations of specific REE-features (i.e., REE-anomalies) shall be regarded as a first approach for further discussion on cold-seep pore water REE geochemistry. Further work is needed to resolve details on REE-dynamics in cold-seep pore waters, especially with regard to behavior of the redox-sensitive element Ce, which would substantially increase the potential of REE as geochemical proxies in modern and ancient cold-seep deposits (e.g., Feng et al., 2009, 2010; Himmler et al., 2010).

Acknowledgements

We appreciate the support of the captain, the crew, and the skillful and experienced work of the ALVIN-team during R/V Atlantis cruise AT3-35BS.

Andy Ungerer (Oregon State University) is acknowledged for analytical support. Funding was provided through the DFG-Research Center/Excellence Cluster “The Ocean in the Earth Systems”.

3 Conclusions and outlook

The three manuscripts presented above provide petrographic and geochemical data on seep carbonates and methane-seep pore waters. The results confirm that authigenic seep carbonates record geochemical changes at methane-seeps. It was main goal of this thesis to characterise geochemical variations at methane-seeps by studying the texture and rare earth element (REE) geochemistry of Recent seep carbonates and methane-seep associated pore waters. This was accomplished by:

- High-resolution REE analysis of aragonitic seep carbonates from the Makran accretionary prism in combination with carbon and oxygen stable isotope and mineralogical data (manuscript 1).
- Detailed petrographic and geochemical studies on seep carbonates from the Amsterdam and Athina mud volcanoes, eastern Mediterranean Sea (manuscript 2).
- Measurements of REEs and major geochemical pore water parameters from two stations on Hydrate Ridge, Cascadia convergent margin off Oregon, north-eastern Pacific (manuscript 3).

The first manuscript reports on high-resolution REE analyses combined with carbon and oxygen stable isotope measurements performed on a single seep-carbonate specimen from an active methane-seep on the Makran accretionary prism. The results show that the pore fluid composition during precipitation of seep carbonates has changed from anoxic pore water to oxic seawater in the course of aragonite precipitation. Negative Ce anomalies are discussed in the light of variable redox conditions during carbonate formation, concluding that negative Ce anomalies in seep carbonates do not necessarily point to oxic condition during carbonate precipitation. However, in order to better understand REE patterns in seep carbonates a combined study of solid phases (e.g., seep carbonates, sediment, organic matter, authigenic pyrite) and

pore waters from other seep locations is desirable. Not only the carbonates, but also the non-carbonate minerals must be included to get a comprehensive data set that allows resolving REE-cycling at methane-seeps in more detail. It seems promising to explore the REE geochemistry in ancient seep carbonates because REE are exceptionally stable during diagenetic processes, and thus could help to decipher (bio) geochemical processes at ancient methane-seeps.

The second manuscript describes the formation of significant volumes of secondary porosity in seep carbonate crusts in the eastern Mediterranean Sea. A scenario is presented to explain vastly observed corrosion patterns: Erosion of overlying sediments exposed the seep carbonates to oxic bottom water where ascending methane and hydrogen sulphide is immediately oxidised. Aerobic oxidation of methane and hydrogen sulphide leads to increasing $p\text{CO}_2$ and decreasing pH, eventually forcing dissolution of the exposed seep carbonates. It is concluded that carbonate dissolution might be more common at Recent methane-seeps than previously recognized. With regard to the amount of methane derived carbon incorporated in seep carbonates, this study sheds light on a probably widespread – though previously overlooked – phenomenon which might represent an additional carbon source to the marine carbon pool. Empirical studies can help to better estimate the amount of carbon reflux from seep-carbonate. In 2008, a set of carbonate cubes was deployed at methane-seeps on the Congo deep-sea fan. The cubes were recently recovered and will be studied in detail on the amount of carbonate that was dissolved.

The third manuscript presents REE profiles in combination with major pore water parameters measured in methane-seep pore waters on Hydrate Ridge. Bicarbonate production during sulphate-dependent anaerobic oxidation of methane favours carbonate-complexation of dissolved REEs, as shown by shale-normalised REE patterns. The carbonate-complexed REEs coprecipitate with authigenic seep carbonates which may act as an efficient sink for pore water REEs at methane-seeps. Microbial activity (i.e. AOM, Ce reduction) apparently influences the liberation of REEs into pore water. Remarkably, negative Ce anomalies are detected in anoxic pore waters and discussed in the light of

increased carbonate alkalinity. Based on these findings it remains difficult to evaluate the potential of Ce as redox proxy in seep carbonates. More REE data on pore waters from seeps with different flux rates may help to unravel the behaviour of Ce at methane-seeps and thus improve the evaluation of Ce anomalies as redox tracers in seep carbonates.

Acknowledgements

I kindly thank Prof. Dr. Jörn Peckmann for giving me the opportunity to carry out this project at the University of Bremen, supervising my studies, and fruitful discussions on scientific and unscientific topics. Prof. Dr. Wolfgang Bach and Prof. Dr. Gerhard Bohrmann encouraged me throughout my studies and generously supported my work. I am indebted to Prof. Dr. Marta Torres and Dr. Brian Haley (Oregon State University) for their invaluable help and support, and for sharing some exciting times in Corvallis. PD Dr. Sabine Kasten, David Fischer, and PD Dr. Matthias Zabel are greatly acknowledged for fruitful discussions and for sharing some of their samples and data. Dr. Daniel Birgel, Dr. Marcus Elvert, Dr. Thomas Pape, and Dr. Heiko Sahling are acknowledged for help at any concerns and stimulating discussions.

My sincere gratitude goes to all the people of the MARUM–Center for Marine and Environmental Sciences and the Department of Geosciences at the University of Bremen who have contributed in many ways to this study and supported my work throughout the last three years: I started in the area of the working groups *Geobiologie* and *Organische Geochemie* in the MARUM building, then I carried out most of the lab work in cooperation with the working group *Petrologie der Ozeankruste* in the GEO building, and finished in the working group *Allgemeine Geologie–Marine Geologie*. All members of the working groups are warmly thanked for inspiring conversations during numerous coffee breaks. I thank Greta Ohling, Angelika Rinkel, Birgit Schmincke, and Dr. Nicloas Dittert for administrative support. Heike Anders, Sebastian Flotow, Prof. Dr. Andreas Klügel, Svenja Rausch, Dr. Monika Segl, Andy Ungerer (Oregon State University), and Dr. Christoph Vogt are acknowledged for analytical and technical support.

I greatly thank my friends and colleagues for sharing pleasant times (mostly) unrelated to science: Esther Arning, Vera Barbara Bender, Eva de

Boever, Florian Brinkmann, Claudia Sofia Burbano, James Collins, Livia Dobre, Benjamin Eickmann, Moataz Adel El-Shafeiy, Giovanni Gattolin, Angelique Gobet, Aline Govin, Mihaela Gradinaru, Cyril Gyri, Antonie Haas, Katrin Heindl, Wei-Li Hong, Calvin & Hobbes, Kraig Joseph, Hendrik Lantzsch, Lars Hoffmann-Sell, Chia-I Huang, Enqing Huang, Matthias Kellermann, André Klicpera, Eva Kwooll, Alice Lefebvre, Yann Marcon, Guillem Mateu Vicens, Siliva Mecozzi, Jan Metzen, Julien Michel, Alice Montinaro, Jesse Muratli, Alexander Müller, Marcello Natalicchio, Jean Nizou, Catalin Petrea, Manuel Plettenberg, Nereo Preto, Xavier Prieto Mollar, Pamela Rossel, Moutusi Roy, Frauke Schmidt, Henry Wu, Marcos Yoshinaga, and Simone Ziegenbalg.

Finally, I am deeply grateful to my family for invaluable support.

References

- AHARON, P., GRABER, E.R., AND ROBERTS, H.H., 1992. Dissolved carbon and $\delta^{13}\text{C}$ anomalies in the water column caused by hydrocarbon seeps on the northwestern Gulf of Mexico slope. *Geo-Marine Letters* 12, 33–40.
- ALIBO, D.S. AND NOZAKI, Y., 1999. Rare earth elements in seawater: Particle association, shale-normalization, and Ce oxidation. *Geochimica et Cosmochimica Acta* 63, 363–372.
- ALOISI, G., PIERRE, C., ROUCHY, J.-M., FOUCHER, J.-P., WOODSIDE, J., AND THE MEDINAUT SCIENTIFIC PARTY, 2000. Methane-related authigenic carbonates of eastern Mediterranean Sea mud volcanoes and their possible relation to gas hydrate destabilisation. *Earth and Planetary Science Letters* 184, 321–338.
- ALOISI, G., BOULOUBASSI, I., HEIJS, S.K., PANCOST, R., PIERRE, C., SINNINGHE DAMSTÉ, J.S., GOTTSCHAL, J.C., FORNEY, L.J., AND ROUCHY, J.-M., 2002. CH_4 -consuming microorganisms and the formation of carbonate crusts at cold seeps. *Earth and Planetary Science Letters* 203, 195–203.
- BAU, M., 1996. Controls on the fractionation of isovalent trace elements in magmatic and aqueous systems: evidence from Y/Ho, Zr/Hf, and lanthanide tetrad effect. *Contributions to Mineralogy and Petrology* 123, 323–333.
- BAU, M. AND DULSKI, P., 1996. Distribution of yttrium and rare-earth elements in the Penge and Kuruman iron-formations, Transvaal Supergroup, South Africa. *Precambrian Research* 79, 37–55.
- BAU, M., BALAN, S., SCHMIDT, K., AND KOSCHINSKY, A., 2010. Rare earth elements in mussel shells of the Mytilidae family as tracers for hidden and fossil high-temperature hydrothermal systems. *Earth and Planetary Science Letters* 299, 310–316.
- BEAL, E.J., HOUSE, C.H., AND ORPHAN, V.J., 2009. Manganese- and iron-dependent marine methane oxidation. *Science* 325, 184–187.
- BEAUCHAMP, B. AND SAVARD, M., 1992. Cretaceous chemosynthetic carbonate mounds in the Canadian Arctic. *Palaios* 7, 434–450.
- BIRGEL, D., HIMMLER, T., FREIWALD, A., PECKMANN, J., 2008. A new constraint on the antiquity of anaerobic oxidation of methane: Late Pennsylvanian seep limestones from southern Namibia. *Geology* 36, 543–546.

- BIRGEL, D. AND PECKMANN, J., 2008. Aerobic methanotrophy at ancient marine methane-seeps: A synthesis. *Organic Geochemistry* 39, 1659–1667.
- BIRGEL, D., FENG, D., ROBERTS, H.H., AND PECKMANN, J., 2011. Changing redox conditions at cold seeps as revealed by authigenic carbonates from Alaminos Canyon, northern Gulf of Mexico. *Chemical Geology*, in press.
- BOETIUS, A., RAVENSCHLAG, K., SCHUBERT, C.J., RICKERT, D., WIDDEL, F., GIESEKE, A., AMANN, R., JØRGENSEN, B.B., WITTE, U., AND PFANNKUCHE, O., 2000. A marine microbial consortium apparently mediating anaerobic oxidation of methane. *Nature* 407, 623–626.
- BOHRMANN, G. AND TORRES, M.E., 2006. Gas hydrates in marine sediments. – In: Schulz, H.D. and Zabel, M. (Eds.): *Marine Geochemistry*, 2nd edition. Springer-Verlag Berlin Heidelberg, pp. 481–512.
- BOHRMANN, G., GREINERT, J., SUESS, E., AND TORRES, M., 1998. Authigenic carbonates from the Cascadia subduction zone and their relation to gas hydrate stability. *Geology* 26, 647–650.
- BOHRMANN, G., HEESCHEN, K., JUNG, H., WEINREBE, W., BARANOV, B., CAILLEAU, B., HEATH, R., HÜHNERBACH, V., HORT, M., MASSON, D., AND TRUMMER, I., 2002. Widespread fluid expulsion along the seafloor of the Coast Rica convergent margin. *Terra Nova* 14, 69–79.
- BOHRMANN, G., CRUISE PARTICIPANTS, 2008. Report and preliminary results of R/V Meteor Cruise M74/3, Fujairah–Male: Cold seeps of the Makran subduction zone (Continental Margin of Pakistan). Berichte Fachbereich Geowissenschaften, Universität Bremen, 266, 161 pp, Bremen.
- BOLHAR, R., KAMBER, B.S., MOORBATH, S., FEDO, C.M., AND WHITEHOUSE, M.J., 2004. Characterisation of early Archaean chemical sediments by trace element signatures. *Earth and Planetary Science Letters* 222, 43–60.
- BROOKINS, D.G., 1989. Aqueous geochemistry of rare earth elements. – In: Lipin, B.R., McKay, G.A. (Eds.): *Geochemistry and mineralogy of rare earth elements*. Mineralogical Society of America, Washington D.C., 348 pp.
- BURTON, E.A., 1993. Controls on marine carbonate cement mineralogy: review and reassessment. *Chemical Geology* 105, 163–179.
- BYRNE, R.H. AND KIM, K.-H., 1990. Rare earth element scavenging in seawater. *Geochimica et Cosmochimica Acta* 54, 2645–2656.

- CAI, W.-J., CHEN, F., POWELL, E.N., WALKER, S.E., PARSON-HUBBARD, K.M., STAFF, G.M., WANG, Y., ASHTON-ALCOX, K., CALLENDER, W.R., AND BRETT, C.E., 2006. Preferential dissolution of carbonate shells driven by petroleum seep activity in the Gulf of Mexico. *Earth and Planetary Science Letters* 248, 227–243.
- CAMPBELL, K.A., 2006. Hydrocarbon seep and hydrothermal vent paleoenvironments and paleontology: past developments and future research directions. *Palaeogeography, Palaeoclimatology, Palaeoecology* 232, 362–407.
- CAMPBELL, K.A., FARMER, J.D., AND DES MARAIS, D., 2002. Ancient hydrocarbon seeps from the Mesozoic convergent margin of California: carbonate geochemistry, fluids and palaeoenvironments. *Geofluids* 2, 63–94.
- CANTRELL, K.C. AND BYRNE, R.H., 1987. Rare earth element complexation by carbonate and oxalate ions. *Geochimica et Cosmochimica Acta* 51, 597–605.
- CARLIER, A., RITT, B., RODRIGUES, C.F., SARRAZIN, J., OLU, K., GRALL, J., AND CLAVIER, J., 2010. Heterogeneous energetic pathways and carbon sources on deep eastern Mediterranean cold seep communities. *Marine Biology* 157, 2545–2565.
- CHARLOU, J.L., DONVAL, J.P., ZITTER, T., ROY, N., JEAN-BAPTISTE, P., FOUCHER, J.-P., WOODSIDE, J. AND MEDINAUT SCIENTIFIC PARTY, 2003. Evidence of methane venting and geochemistry of brines on mud volcanoes of the eastern Mediterranean Sea. *Deep-Sea Research I* 50, 941–958.
- CLAYPOOL, G.W. AND KVENVOLDEN, K.A., 1983. Methane and other hydrocarbons in marine sediments. *Annual Reviews in Earth and Planetary Science* 11, 299–327.
- DAVIDSON, D.W., LEAIST, D.J., AND HESSE, R., 1983. Oxygen-18 enrichment in water of a clathrate hydrate. *Geochimica et Cosmochimica Acta* 47, 2293–2295.
- DELISLE, G., 2004. The mud volcanoes of Pakistan. *Environmental Geology* 46, 1024–1029.
- DE BAAR, H.J.W., BACON, P.M., AND BREWER, P.G., 1983. Rare earth distributions with a positive Ce anomaly in the Western North Atlantic Ocean. *Nature* 301, 324–327.
- DE BAAR, H.J., BACON, M.P., AND BREWER, P.G., 1985. Rare earth elements in the Pacific and Atlantic Oceans. *Geochimica et Cosmochimica Acta* 49, 1943–1959.
- DE BAAR, H.J.W., GERMAN, C.R., ELDERFIELD, H., AND VAN GAANS, P., 1988. Rare earth element distribution in anoxic waters of the Cariaco Trench. *Geochimica et Cosmochimica Acta* 52, 1203–1291.

- DICKENS, G.R., 2003. Rethinking the global carbon cycle with a large, dynamic and microbially mediated gas hydrate capacitor. *Earth and Planetary Science Letters* 213, 169–183.
- DICKSON, J.A.D., 1966. Carbonate identification and genesis as revealed by staining. *Journal of Sedimentary Research* 36, 491–505.
- DIMITROV, L.I., 2002. Mud volcanoes – the most important pathway for degassing deeply buried sediments. *Earth-Science Reviews* 59, 49–76.
- DÄHLMANN, A. AND DE LANGE, G.J., 2003. Fluid–sediment interactions at Eastern Mediterranean mud volcanoes: a stable isotope study from ODP Leg 160. *Earth and Planetary Science Letters* 212, 377–391.
- ELDERFIELD, H. AND SHOLKOVITZ, E.R., 1987. Rare earth elements in the pore waters of reducing nearshore sediments. *Earth and Planetary Science Letters* 82, 280–288.
- ELVERT, M. AND NIEMANN, H., 2008. Occurrence of unusual steroids and hopanoids derived from aerobic methanotrophs at an active marine mud volcano. *Organic Geochemistry* 39, 167–177.
- EPSTEIN, S., BUCHSBAUM, R., LOWENSTAMM, H.A., AND UREY, H.C., 1953. Revised carbonate-water isotopic temperature scale. *Bulletin of the Geological Society of America* 64, 1315–1326.
- FAIRBANKS, R.G., 1989. A 17,000 year glacio-eustatic sea level record: influence of glacial melting rates on the Younger Dryas event and deep ocean circulation. *Nature* 342, 637–642.
- FARHOUDI, G. AND KARIG, D.E., 1977. Makran of Iran and Pakistan as an active arc system. *Geology* 5, 664–668.
- FEIGL, F. AND ANGER, V., 1958. *Spot tests in inorganic analysis*, 6th edition, Elsevier Science.
- FENG, D., CHEN, D., AND ROBERTS, H.H., 2008. Sedimentary fabrics in the authigenic carbonates from Bush Hill: implication for seabed fluid flow and its dynamic signature. *Geofluids* 8, 301–310.
- FENG, D., CHEN, D., AND PECKMANN, J., 2009a. Rare earth elements in seep carbonates as tracers of variable redox conditions at ancient hydrocarbon seeps. *Terra Nova* 21, 49–56.
- FENG, D., CHEN, D., AND ROBERTS, H.H., 2009b. Petrographic and geochemical characterization of seep carbonate from Bush Hill (GC 185) gas vent and hydrate site of the Gulf of Mexico. *Marine and Petroleum Geology* 26, 1190–1198.

References

- FENG D., CHEN, D., PECKMANN, J., AND BOHRMANN, G., 2010a. Authigenic carbonates from methane-seeps of the northern Congo fan: Microbial formation mechanism. *Marine and Petroleum Geology* 27, 748–756.
- FENG, D., ROBERTS, H.H., CHENG, H., PECKMANN, J., BOHRMANN, G., EDWARDS, R.L., AND CHEN, D., 2010b. U/Th dating of cold-seep carbonates: an initial comparison. *Deep-Sea Research II* 75, 2055–2060.
- FISHER, C. R., 1990. Chemoautotrophic and methanotrophic symbioses in marine invertebrates. *Reviews in Aquatic Sciences* 2, 399–436.
- FLÜGEL, E., 2004. *Microfacies of Carbonate Rocks, Analysis, Interpretation and Application*. Springer-Verlag, Berlin, Heidelberg, New York.
- FORMOLO, M.J., LYONS, T.W., ZHANG, C., KELLEY, C., SASSEN, R., HORITA, J., AND COLE, D.R., 2004. Quantifying carbon sources in the formation of authigenic carbonates at gas hydrate sites in the Gulf of Mexico. *Chemical Geology* 205, 253–264.
- FROELICH, P.N., KLINKHAMMER, G.P., BENDER, M.L., LUEDTKE, N.A., HEATH, G.R., CULLEN, D., DAUPHIN, P., HAMMOND, D, HARTMANN, B., AND MAYNARD, V., 1979. Early oxidation of organic matter in pelagic sediments of the eastern equatorial Atlantic: Suboxic diagenesis. *Geochimica et Cosmochimica Acta* 43, 1075–1090.
- FRUEHN, J, WHITE, R.S., AND MINSHULL, T.A., 1997. Internal deformation and compaction of the Makran accretionary wedge. *Terra Nova* 9, 101–104.
- GARZANTI, E., CRITELLI, S., AND INGERSOLL, R.V., 1996. Paleogeographic and paleotectonic evolution of the Himalayan Range as reflected by detrital modes of Tertiary sandstones and modern sands (Indus transect, India and Pakistan). *Geological Society of America Bulletin* 108, 631–642.
- GERMAN, C.R. AND ELDERFIELD, H., 1990. Rare earth elements in the NW Indian Ocean. *Geochimica et Cosmochimica Acta* 54, 1929–1940.
- GOLONKA, J., 2004. Plate tectonic evolution of the southern margin of Eurasia in the Mesozoic and Cenozoic. *Tectonophysics* 381, 235–273.
- GRANDO, G. AND MCCLAY, K., 2007. Morphotectonic domains and structural styles in the Makran accretionary prism, offshore Iran. *Sedimentary Geology* 196, 157–179.
- GRASSHOFF, K., KREMLING, K., AND ERHARDT, M., 1999. *Methods of seawater analysis*. Wiley-VCH, New York.

- GREIENRT, J., BOHRMANN, G., AND SUESS, E., 2001. Gas hydrate-associated carbonates and methane-venting at Hydrate Ridge: classification, distribution, and origin of authigenic lithologies. – In: Paull, C.K. and Dillon, P.W. (Eds.): *Natural Gas Hydrates: Occurrence, Distribution, and Detection*. Geophysical Monograph 124, pp. 99–113.
- GROSSMAN, E.L. AND KU, T.-L., 1986. Oxygen and carbon isotope fractionation in biogenic aragonite: temperature effects. *Chemical Geology* 59, 59–74.
- HAAS, A., PECKMANN, J., ELVERT, M., SAHLING, H., BOHRMANN, G., 2010. Patterns of carbonate authigenesis at the Kouilou pockmarks on the Congo deep-sea fan. *Marine Geology* 268, 129–136.
- HAN, X., SUESS, E., SAHLING, H., AND WALLMANN, K., 2004. Fluid venting activity on the Costa Rica margin: new results from authigenic carbonates. *International Journal of Earth Sciences* 93, 595–611.
- HALEY, B.A. AND KLINKHAMMER, G.P., 2003. Complete separation of rare earth elements from small volume samples by automated ion chromatography: method development and application to benthic flux. *Marine Chemistry* 82, 197–220.
- HALEY, B.A., KLINKHAMMER, G.P., AND MCMANUS, J., 2004. Rare earth elements in pore waters of marine sediments. *Geochimica et Cosmochimica Acta* 68, 1265–1279.
- HERZIG, P.M. AND HANNINGTON, M.D., 2006. Input from the deep: hot vents and cold seeps. – In: Schulz, H.D. and Zabel, M. (Eds.): *Marine Geochemistry*, 2nd edition. Springer-Verlag Berlin Heidelberg, pp. 457–479.
- HIMMLER, T., BACH, W., BOHRMANN, G., AND PECKMANN, J., 2010. Rare earth elements in authigenic methane-seep carbonates as tracers for fluid composition during early diagenesis. *Chemical Geology* 277, 126–136.
- HINRICH, K.-U. AND BOETIUS, A., 2002. The anaerobic oxidation of methane: new insights in microbial ecology and biogeochemistry. – In: Wefer, G., Hebbeln, D., Jørgensen, B.B., Schlüter, M., Van Weering, T. (Eds.): *Ocean Margin Systems*. Springer-Verlag Berlin Heidelberg, pp. 457–477.
- IRWIN, H., CURTIS, C., AND COLEMAN, M., 1977. Isotopic evidence for source of diagenetic carbonates formed during burial of organic-rich sediments. *Nature* 269, 209–213.
- JOCHUM, K.P., NOHL, U., HERWIG, K., LAMMEL, E., STOLL, B., AND HOFMANN, A.W., 2005. GeoReM: A new geochemical database for reference materials and isotopic standards. *Geostandards and Geoanalytical Research* 29, 333–338.

References

- JOYE, S.B., BOETIUS, A., ORCUTT, B.N., MONTOYA, J.P., SCHULZ, H.N., ERICKSON, M.J., AND LUGO, S.K., 2004. The anaerobic oxidation of methane and sulfate reduction in sediments from Gulf of Mexico cold seeps. *Chemical Geology* 205, 219–238.
- JUDD, A. AND HOVLAND, M., 2007. *Seabed Fluid Flow*. Cambridge University Press, Cambridge.
- JØRGENSEN, B.B. AND KASTEN, S., 2006. Sulfur cycling and methane oxidation. – In: Schulz, H.D. and Zabel, M. (Eds.): *Marine Geochemistry*, 2nd edition. Springer-Verlag Berlin Heidelberg, pp. 271–309.
- KAMBER, B.S. AND WEBB, G.E., 2001. The geochemistry of late Archaean microbial carbonate: Implications for ocean chemistry and continental erosion history. *Geochimica et Cosmochimica Acta* 65, 2509–2525.
- KLAUCKE, I., WEINREBE, W., PETERSEN, C.J., AND BOWDEN, D., 2010. Temporal variability of gas seeps offshore New Zealand: Multi-frequency geoacoustic imaging of the Wairarapa area, Hikurangi margin. *Marine Geology* 272, 49–58.
- KLINKHAMMER, G.P., ELDERFIELD, H., EDMOND, J. M., AND MITRA, A., 1994. Geochemical implications of rare earth element patterns in hydrothermal fluids from mid-ocean ridges. *Geochimica et Cosmochimica Acta* 58, 5105–5113.
- KNITTEL, K., BOETIUS, A., LEMKE, A., EILERS, H., LOCHTE, K., PFANNKUCHE, O., LINKE P., AND AMANN, R., 2003. Activity, distribution, and diversity of sulfate reducers and other bacteria in sediments above Gas Hydrate (Cascadia Margin, Oregon). *Geomicrobiology Journal* 20, 269–294.
- KOPF, A.J., 2002. Significance of mud volcanism. *Reviews of Geophysics* 40, 1005.
- KUKOWSKI, N., SCHILLHORN, T., HUHNS, K., VON RAD, U., HUSEN, S., AND FLUEH, E.R., 2001. Morphotectonics and mechanics of the central Makran accretionary wedge off Pakistan. *Marine Geology* 173, 1–19.
- KULM, L.D., SUESS, E., MOORE, J.C., CARSON, B., LEWIS, B.T., RITGER, S.D., KADKO, D.C.; THORNBURG, T.M., EMBLEY, R.W., RUGH, W.D., MASSOTH, G.J., LANGSETH, M.G., COCHRANE, G.R., AND SCAMMAN, R.L., 1986. Oregon subduction zone: venting, fauna, and carbonates. *Science* 231, 561–566.
- LEE, J.H. AND BYRNE, R.H., 1993. Complexation of trivalent rare earth elements (Ce, Eu, Gd, Tb, Yb) by carbonate ions. *Geochimica et Cosmochimica Acta* 57, 295–302.

- LEEFMANN, T., BAUERMEISTER, J., KRONZ, A., LIEBETRAU, V., REITNER, J., AND THIEL, V., 2008. Miniaturized biosignature analysis reveals implication for the formation of cold seep carbonates at Hydrate Ridge (off Oregon, USA). *Biogeosciences* 5, 731–738.
- LEVIN, L.A., 2005. Ecology of cold seep sediments: interactions of fauna with flow, chemistry and microbes. *Oceanography and Marine Biology: An Annual Review* 43, 1–46.
- LUFF, R. AND WALLMANN, K., 2003. Fluid flow, methane fluxes, carbonate precipitation and biogeochemical turnover in gas hydrate bearing sediments at Hydrate Ridge, Cascadia Margin: numerical modeling and mass balances. *Geochimica et Cosmochimica Acta* 67, 3403–3421.
- LYKOUSIS, V., ALEXANDRI, S., WOODSIDE, J., DE LANGE, G., DÄHLMANN, A., PERISSORATIS, C., HEESCHEN, K., IOAKIM, C., SAKELLARIOU, D., NOMIKOU, P., ROUSAKIS, G., CASAS, D., BALLAS, D., AND ERCILLA, G., 2009. Mud volcanoes and gas hydrates in the Anaximander mountains (Eastern Mediterranean Sea). *Marine and Petroleum Geology* 26, 854–872.
- MATSUMOTO, R., 1990. Vuggy carbonate crust formed by hydrocarbon seepage on the continental shelf of Baffin Island, northeast Canada. *Geochemical Journal* 24, 143–158.
- MATSUMOTO, R., 1992. Causes of oxygen isotope depletion of interstitial waters from sites 798 and 799, Japan Sea, Leg 128. *Proceedings of the Ocean Drilling Program, Scientific Results, Vol. 127/128*, 697–703.
- MICHAELIS, M., SEIFERT, R., NAUHAUS, K., TREUDE, T., THIEL, V., BLUMENBERG, M., KNITTEL, K., GIESEKE, A., PETERKNECHT, K., PAPE, T., BOETIUS, A., AMANN, R., JØRGENSEN, B.B., WIDDEL, F., PECKMANN, J., PIMENOV, N.V., GULIN, M.B., 2002. Microbial reefs in the Black Sea fuelled by anaerobic oxidation of methane. *Science* 297, 1013–1015.
- MILKOV, A.V., 2000. Worldwide distribution of submarine mud volcanoes and associated gas hydrates. *Marine Geology* 167, 29–42.
- MILLERO, F.J., MORSE, J., AND CHEN, C.-T., 1979. The carbonate system in the western Mediterranean Sea. *Deep-Sea Research* 26, 1395–1404.
- MINSHULL, T. AND WHITE, R., 1989. Sediment compaction and fluid migration in the Makran accretionary prism. *Journal of Geophysical Research* 94, 7387–7402.
- MOFFETT, J.W., 1990. Microbially mediated cerium oxidation in sea water. *Nature* 345, 421–423.

References

- MORSE, J.W., MUCCI, A., AND MILLERO, F.J., 1980. The solubility of calcite and aragonite in seawater of 35‰ salinity at 25°C and atmospheric pressure. *Geochimica et Cosmochimica Acta* 44, 85–94.
- MÜLLER, G. AND GASTNER, M., 1971. The 'Karbonat-Bombe', a simple device for the determination of the carbonate content in sediments, soils and other materials. *Neues Jahrbuch für Mineralogie* 10, 466–469.
- NAEHR, T.H., EICHHUBL, P., ORPHAN, V.J., HOVLAND, M., PAULL, C.K., USSLER III, W., LORENSEN, T.D., AND GREENE, H.G., 2007. Authigenic carbonate formation at hydrocarbon seeps in continental margin sediments: A comparative study. *Deep-Sea Research II* 54, 1268–1291.
- NAEHR, T.H., BIRGEL, D., BOHRMANN, G., MCDONALD, I.R. AND KASTEN, S. 2009. Biogeochemical controls on authigenic carbonate formation at the Chapopote "asphalt volcano", Bay of Campeche. *Chemical Geology* 266, 390–402.
- NANCE, W.B. AND TAYLOR, S.R., 1976. Rare earth element patterns and crustal evolution—I. Australian post-Archean sedimentary rocks. *Geochimica et Cosmochimica Acta* 40, 1539–1551.
- NAUDTS, L., GREINERT, J., ARTEMOV, Y., STAELENS, P., POORT, J., VAN RENSBERGEN, P., AND DE BATIST, M., 2006. Geological and morphological setting of 2778 methane-seeps in the Dnepr paleo-delta, northwestern Black Sea. *Marine Geology* 227, 177–199.
- OLU-LE ROY, K., SIBUET, M., FIALA-MÉDIONI, A., GOFAS, S., SALAS, C., MARIOTTI, A., FOUCHER, J.-P., AND WOODSIDE, J., 2004. Cold seep communities in the deep eastern Mediterranean Sea: composition, symbiosis and spatial distribution on mud volcanoes. *Deep-Sea Research I* 51, 1915–1936.
- PANCOST, R., SINNINGHE DAMSTÉ, J.S., DE LINDT, S., VAN DER MAAREL, M.J.E.C., GOTTSCHAL, J.C., AND THE MEDINAUT SHIPBOARD SCIENTIFIC PARTY, 2000. Biomarker evidence for widespread anaerobic methane oxidation in Mediterranean sediments by a consortium of methanogenic archaea and bacteria. *Applied and Environmental Microbiology* 66, 1126–1132.
- PAPE, T., KASTEN, S., ZABEL, M., BAHR, A., ABEGG, F., HOHENBURG, H.-J., AND BOHRMANN, G., 2010. Gas hydrates in shallow deposits of the Amsterdam mud volcano, Anaximander Mountains, Northeastern Mediterranean Sea. *Geo-Marine Letters* 30, 187–206.

- PARNELL, L., 2002. Fluid seeps at continental margins: towards an integrated plumbing system. *Geofluids* 2, 57–61.
- PAULL, C.K., CHANTON, J.P., NEUMANN, A.C., COSTON, J.A., MARTENS, C.S., AND SHOWERS, W., 1992. Indicators of methane-derived carbonates and chemosynthetic organic carbon deposits: examples from the Florida Escarpment. *Palaios* 7, 361–375.
- PEARCE, N.J.G., PERKINS, W.T., WESTGATE, J.A., GORTON, M.P., JACKSON, S.E., NEAL, C.R., AND CHENERY, S.P., 1997. A compilation of new and published major and trace element data for NIST SRM 610 and NIST SRM 612 glass reference materials. *Geostandards Newsletter* 21, 157–161.
- PECKMANN, J., THIEL, V., MICHAELIS, W., CLARI, P., GAILLARD, C., MARTIRE, L., AND REITNER, J., 1999. Cold seep deposits of Beauvoisin (Oxfordian; southeastern France) and Marmorito (Miocene; northern Italy): microbially induced, authigenic carbonates. *International Journal of Earth Sciences* 88, 60–75.
- PECKMANN, J., REIMER, A., LUTH, U., LUTH, C., HANSEN, B.T., HEINICKE, C., HOEFS, J., AND REITNER, J., 2001. Methane-derived carbonates and authigenic pyrite from the northwestern Black Sea. *Marine Geology* 177, 129–150.
- PECKMANN, J. AND THIEL, V., 2004. Carbon cycling at ancient methane-seeps. *Chemical Geology* 205, 443–467.
- PECKMANN, J., BIRGEL, D., AND KIEL, S., 2009. Molecular fossils reveal fluid composition and flow intensity at a Cretaceous seep. *Geology* 37, 847–850.
- PECKMANN, J., GOEDERT, J.L., HEINRICHS, T., HOEFS, J., AND REITNER, J., 2003. The Late Eocene ‘Whiskey Creek’ methane-seep deposit (western Washington State)—Part II: Petrology, stable isotopes, and biogeochemistry. *Facies* 48, 241–254.
- PIERRE, C. AND FOUQUET, Y., 2007. Authigenic carbonates from methane-seeps of the Congo deep-sea fan. *Geo-Marine Letters* 27, 249–257.
- PIRLET, H., WEHRMANN, L.M., BRUNNER, B., FRANK, N., DEWANCKELE, J., VAN ROOIJ, D., FOUBERT, A., SWENNEN, R., NAUDTS, L., BOONE, M., CNUUDE, V., AND HENRIET, J.-P., 2009. Diagenetic formation of gypsum and dolomite in a cold-water coral mound in the Porcupine Seabight, off Ireland. *Sedimentology* 57, 786–805.
- PLATT, J.P., LEGETT, J.K., YOUNG, J., RAZA, H., AND ALAM, S., 1985. Large-scale sediment underplating in the Makran accretionary prism, southwest Pakistan. *Geology* 13, 507–511.

References

- POURRET, O., DAVRANCHE, M., GRUAU, G., AND DIA, A., 2008. New insights into cerium anomalies in organic-rich alkaline waters. *Chemical Geology* 251, 120–127.
- QU, C., LU, B., AND LIU, G., 2009. Enrichment of lanthanides in aragonite. *Journal of Rare Earths* 27, 1062–1065.
- RITGER, S., CARSON, B., AND SUESS, E., 1987. Methane-derived authigenic carbonates formed by subduction-induced pore-water expulsion along the Oregon/Washington margin. *Geological Society of America Bulletin* 98, 147–156.
- REEBURGH, W.S., 2007. Oceanic methane biogeochemistry. *Chemical Reviews* 107, 486–513.
- ROBERTS, H.H. AND AHARON, P., 1994. Hydrocarbon-derived carbonate buildups of the northern Gulf of Mexico continental slope: a review of submersible investigations. *Geo-Marine Letters* 14, 135–148.
- RULKÖTTER, J., 2006. Organic matter: The driving force for early diagenesis. – In: Schulz, H.D. and Zabel, M. (Eds.): *Marine Geochemistry*, 2nd edition. Springer-Verlag Berlin Heidelberg, pp. 125–168.
- SAHLING, H., RICKERT, D., LEE, R.W., LINKE, P., AND SUESS, E., 2002. Macrofaunal community structure and sulfide flux at gas hydrate deposits from the Cascadia convergent margin, NE Pacific. *Marine Ecology Progress Series* 231, 121–138.
- SAIN, K., MINSHULL, T.A., SINGH, S.C., AND HOBBS, R.W., 2000. Evidence for a thick free gas layer beneath the bottom simulating reflector in the Makran accretionary prism. *Marine Geology* 164, 3–12.
- SCHLÜTER, M., 2002. Fluid flow in continental margin sediments. – In: Wefer, G., Hebbeln, D., Jørgensen, B.B., Schlüter, M., Van Weering, T. (Eds.): *Ocean Margin Systems*. Springer-Verlag Berlin Heidelberg, pp. 205–217.
- SCHOONEN, M.A.A., 2004. Mechanisms of sedimentary pyrite formation. – In: Amend, J.P., Edward, J.K., Lyons, T.W (Eds.): *Sulfur biogeochemistry—Past and present*. Geological Society of America Special Papers 379, Boulder, Colorado, pp. 117–134.
- SCHULZ, H.N. AND JØRGENSEN, B.B., 2001. Big bacteria. *Annual Review of Microbiology* 55, 105–137.
- SHOLKOVITZ, E.R. AND ELDERFIELD, H., 1988. Cycling of dissolved rare earth elements in Chesapeake Bay. *Global Biogeochemical Cycles* 2, 157–176.

- SHOLKOVITZ, E.R., LANDING, W.M., AND LEWIS, B.L., 1994. Ocean particle chemistry: The fractionation of rare earth elements between suspended particles and seawater. *Geochimica et Cosmochimica Acta* 58, 1567–1579.
- SIBUET, M. AND OLU-LE ROY, K., 2002. Cold seep communities on continental margins: structure and quantitative distribution relative to geological and fluid venting patterns. – In: Wefer, G., Hebbeln, D., Jørgensen, B.B., Schlüter, M., Van Weering, T. (Eds.): *Ocean Margin Systems*. Springer-Verlag Berlin Heidelberg, pp. 235–251.
- SOLOMON, E.A., KASTNER, M., JANNESCH, H., ROBERTSON, G., AND WEINSTEIN, Y., 2008. Dynamic fluid flow and chemical fluxes associated with a seafloor gas hydrate deposit on the northern Gulf of Mexico. *Earth and Planetary Science Letters* 270, 95–105.
- SUESS, E., BOHRMANN, G., VON HUENE, R., LINKE, P., WALLMANN, K., LAMMERS, S., SAHLING, H., WINCKLER, G., LUTZ, R.A., AND ORANGE, D., 1998. Fluid venting in the Aleutian subduction zone. *Journal of Geophysical Research* 103 (B2), 2597–2614.
- SUESS, E., TORRES, M.E., BOHRMANN, G., COLLIER, R.W., GREINERT, J., LINKE, P., REHDER, G., TRÉHU, A., WALLMANN, K., WINCKLER, G., AND ZULEGER, E., 1999. Gas hydrate destabilization: Enhanced dewatering, benthic material turnover and large methane plumes at the Cascadia convergent margin. *Earth and Planetary Science Letters* 170, 1–15.
- SWEENEY, R.E., 1988. Petroleum-related hydrocarbon seepage in a recent North Sea sediment. *Chemical Geology* 71, 53–64.
- TAYLOR, S.R. AND MCLENNAN, S.M., 1985. *The Continental Crust: Its Composition and Evolution*. Blackwell Scientific Publications, Oxford, 312 pp.
- TEICHERT, B.M.A., BOHRMANN, G., AND SUESS, E., 2005. Chemoherms on Hydrate Ridge—unique microbially-mediated carbonate build-ups growing into the water column. *Palaeogeography, Palaeoclimatology, Palaeoecology* 227, 67–85.
- TERAKADO, Y. AND MASUDA, A., 1988. The coprecipitation of rare-earth elements with calcite and aragonite. *Chemical Geology* 69, 103–110.
- THIEL, V., PECKMANN, J., REITNER, J., SEIFERT, R., WEHRUNG, P., AND MICHAELIS, W., 1999. Highly isotopically depleted isoprenoids – molecular markers for ancient methane venting. *Geochimica et Cosmochimica Acta* 63, 3959–3966.
- THIEL, V., PECKMANN, J., RICHNOW, H.H., LUTH, U., REITNER, J., AND MICHAELIS, W., 2001. Molecular signals for anaerobic oxidation in Black Sea seep carbonates and a microbial mat. *Marine chemistry* 73, 97–112.

- TISSOT, B. AND WELTE, H., 1992. *Petroleum formation and occurrence*. Springer-Verlag, 536 pp.
- TORRES, M.E., MCMANUS, J., HAMMOND, D.E., DE ANGELIS, M.A., HEESCHEN, K.U., COLBERT, S.L., TRYON, M.D., BROWN, K.M., AND SUESS, E., 2002. Fluids and chemical fluxes in and out of sediments hosting methane hydrate deposits on Hydrate Ridge, OR, I: Hydrological provinces. *Earth and Planetary Science Letters* 201, 525–540.
- TORRES, M.E., EMBLEY, R.W., MERLE, S.G., TRÉHU, A.M., COLLIER, R.W., SUESS, E., AND HEESCHEN, K.U., 2009. Methane sources feeding cold seeps on the shelf and upper continental slope off central Oregon, USA. *Geochemistry Geophysics Geosystems* 10, Q11003, doi:10.1029/2009GC002518.
- TREUDE, T., BOETIUS, A., KNITTEL, K., WALLMANN, K., AND JØRGENSEN, B.B., 2003. Anaerobic oxidation of methane above gas hydrates at Hydrate Ridge, NE Pacific. *Marine Ecology Progress Series* 264, 1–14.
- TRYON, M.D., BROWN, K.M., TORRES, M.E., TRÉHU, A.M., MCMANUS, J., AND COLLIER, R.W., 1999. Measurements of transience and downward fluid flow near episodic methane gas vents, Hydrate Ridge, Cascadia. *Geology* 27, 1075–1078.
- TRYON, M.D. AND BROWN, K.M., 2001. Complex flow patterns through Hydrate Ridge and their impact on seep biota. *Geophysical Research Letters* 28, 2863–2866.
- VALENTINE, D.L., KASTNER, M., WARDLAW, G.D., WANG, X., PURDY, A., AND BARTLETT, D.H., 2005. Biogeochemical investigations of marine methane-seeps, Hydrate Ridge, Oregon. *Journal of Geophysical Research* 110, G02005, doi:10.1029/2005JG000025.
- VON RAD, U., RÖSCH, H., BERNER, U., GEYH, M., MARCHIG, V., AND SCHULZ, H., 1996. Authigenic carbonates derived from oxidized methane vented from the Makran accretionary prism off Pakistan. *Marine Geology* 136, 55–77.
- VON RAD, U., BERNER, U., DELISELE, G., DOOSE-ROLINSKI, H., FECHNER, N., LINKE, P., LÜCKGE, A., ROESER, H.A., SCHMALJOHANN, R., WIEDICKE, M., AND SONNE 122/130 SCIENTIFIC PARTIES, 2000. Gas and fluid venting at the Makran accretionary wedge off Pakistan, *Geo-Marine Letters* 20, 10–19.
- WEBB, G.E. AND KAMBER, B.S., 2000. Rare earth elements in Holocene reefal microbialites: A new shallow seawater proxy. *Geochimica et Cosmochimica Acta* 64, 1557–1565.
- WEBB, G.E., NOTHDURFT, L.D., KAMBER, B.S., KLOPROGGE, J.T., AND ZHAOS, J.-X., 2009. Rare earth element geochemistry of scleractinian coral skeleton during meteoric diagenesis: a sequence through neomorphism of aragonite to calcite. *Sedimentology* 56, 1433–1463.

- WHITE, R.S., 1984. Active and passive plate boundaries around the Gulf of Oman, north-west Indian Ocean. *Deep-Sea Research* 31, 731–745.
- WHITICAR, M.J., 1999. Carbon and hydrogen isotope systematics of bacterial formation and oxidation of methane. *Chemical Geology* 161, 291–314.
- WHITICAR, M.J. AND FABER, E., 1986. Methane oxidation in sediment and water column environments – Isotope evidence. *Organic Geochemistry* 10, 759–768.
- WIEDICKE, M., NEBEN, S., AND SPIESS, V., 2001. Mud volcanoes at the front of the Makran accretionary complex, Pakistan. *Marine Geology* 172, 57–73.
- WOODSIDE, J.M., IVANOV, M.K., LIMONOV, A.F., AND SHIPBOARD SCIENTISTS OF THE ANAXIPROBE EXPEDITIONS, 1998. Shallow gas and gas hydrates in the Anaximander Mountains region, eastern Mediterranean Sea. – In: Henriot, J.-P., Mienert, J. (Eds.): *Gas Hydrates: Relevance to World Margin Stability and Climate Change*, Geol. Soc. London Spec. Publ. 137, pp. 177–193.
- WRIGHT, J., SCHRADER, H., AND HOLSER, W.T., 1987. Paleoredox variations in ancient oceans recorded by rare earth elements in fossil apatite. *Geochimica et Cosmochimica Acta* 51, 631–644.
- ZHONG, S. AND MUCCI, A., 1995. Partitioning of rare earth elements (REEs) between calcite and seawater solutions at 25°C and 1 atm, and high dissolved REE concentrations. *Geochimica et Cosmochimica Acta* 59, 443–453.

**Erklärung gemäß § 6 Abs. 5 der Promotionsordnung der Universität
Bremen für die mathematischen, natur- und
ingenieurwissenschaftlichen Fachbereiche**

Hiermit versichere ich, dass ich die vorliegende Arbeit

1. ohne unerlaubte fremde Hilfe angefertigt habe,
2. keine anderen als die von mir im Text angegebenen Quellen und Hilfsmittel benutzt habe und
3. die den benutzten Werken wörtlich oder inhaltlich entnommenen Stellen als solche kenntlich gemacht habe.

Bremen, 30. März 2011

Tobias Himmler